Article
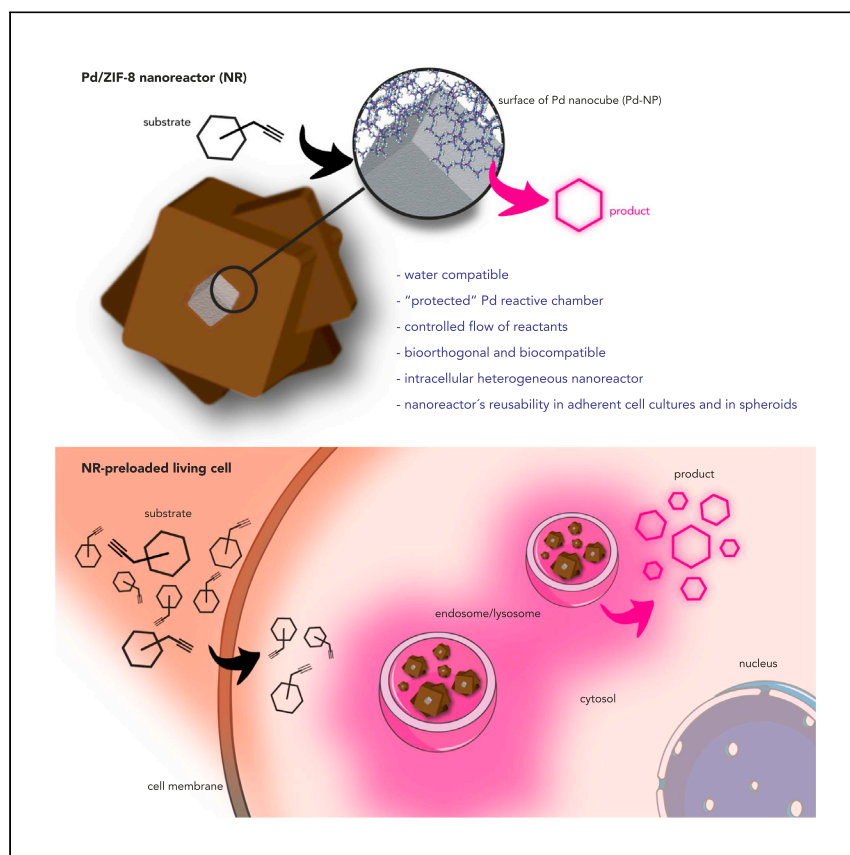
Core-Shell Palladium/MOF Platforms as Diffusion-Controlled Nanoreactors in Living Cells and Tissue Models

Pd/ZIF-8 nanoreactor (NR)

substrate

surface of Pd nanocube (Pd-NP)

product

- water compatible
- "protected" Pd reactive chamber
- controlled flow of reactants
- bioorthogonal and biocompatible
- intracellular heterogeneous nanoreactor
- nanoreactor´s reusability in adherent cell cultures and in spheroids

NR-preloaded living cell

substrate

product

endosome/lysosome

nucleus

cytosol

cell membrane

Martínez et al. demonstrate the feasibility of using core-shell Pd/MOF nanoreactors as intracellular metallo-catalysts, which can be reused within the same cells with recurrent batches of reactants, both in adherent cell cultures and in spheroids. The MOF-based shell preserves the integrity of the catalytic chamber while providing for bio-orthogonality.

Raquel Martínez, Carolina Carrillo-Carrión, Paolo Destito, ..., Fernando Lopez, José L. Mascareñas, Pablo del Pino

joseluis.mascarenas@usc.es (J.L.M.)
pablo.delpino@usc.es (P.d.P.)

HIGHLIGHTS

The MOF cloak allows diffusion of reactants while protecting the Pd catalytic chamber

The MOF cloak provides for orthogonality (substrate selectivity) and biocompatibility

The core-shell nanoreactors intracellularly process sequential batches of reactants

Demonstration of a transition-metal promoted reaction in a living tissue model

Article

Core-Shell Palladium/MOF Platforms as Diffusion-Controlled Nanoreactors in Living Cells and Tissue Models

Raquel Martínez,[1,5] Carolina Carrillo-Carrión,[1,5] Paolo Destito,[2] Aitor Alvarez,[1] María Tomás-Gamasa,[2] Beatriz Pelaz,[3] Fernando Lopez,[2,4] José L. Mascareñas,[2,6,*] and Pablo del Pino[1,7,8,*]

SUMMARY

Translating the potential of transition metal catalysis to biological and living environments promises to have a profound impact in chemical biology and biomedicine. A major challenge in the field is the creation of metal-based catalysts that remain active over time. Here, we demonstrate that embedding a reactive metallic core within a microporous metal-organic framework-based cloak preserves the catalytic site from passivation and deactivation, while allowing a suitable diffusion of the reactants. Specifically, we report the fabrication of nanoreactors composed of a palladium nanocube core and a nanometric imidazolate framework, which behave as robust, long-lasting nanoreactors capable of removing propargylic groups from phenol-derived pro-fluorophores in biological milieu and inside living cells. These heterogeneous catalysts can be reused within the same cells, promoting the chemical transformation of recurrent batches of reactants. We also report the assembly of tissue-like 3D spheroids containing the nanoreactors and demonstrate that they can perform the reactions in a repeated manner.

INTRODUCTION

Intracellular enzymes play an essential role in maintaining and controlling the cell's metabolism and function and have evolved to catalyze life-sustaining reactions. Scientists are not limited by the constraints of life and evolution and can therefore aspire to develop non-natural catalytic reactors capable of working inside living environments. These systems could provide unprecedented opportunities for cellular intervention and eventually lead to the discovery of innovative biomedical tools.[1]

Within the catalysis field, transition metal catalysis is especially appealing, owing to the innumerable type of transformations that can be achieved. Although most of these reactions have been carried out in organic solvents and under water-free conditions, recent years have witnessed a significant increase in metal-mediated reactions that can occur in complex aqueous environments and even within living mammalian cells.[2–8] Initial work in the field was focused on homogeneous copper-promoted azide-alkyne annulations[9–14] and ruthenium-mediated uncaging reactions;[15–20] however, more recently, other metals, like gold,[19,21,22] iridium,[23] osmium,[24] and palladium,[25] have also demonstrated potential to induce specific transformations of exogenous substrates in biological settings. Unfortunately, these catalysts tend to be deactivated over time and therefore cannot be used in a recurrent, long-lasting manner.

[1]Centro Singular de Investigación en Química Biolóxica e Materiais Moleculares (CiQUS) and Departamento de Física de Partículas, Universidade de Santiago de Compostela, 15782 Santiago de Compostela, Spain

[2]Centro Singular de Investigación en Química Biolóxica e Materiais Moleculares (CiQUS) and Departamento de Química Orgánica, Universidade de Santiago de Compostela, 15782 Santiago de Compostela, Spain

[3]Centro Singular de Investigación en Química Biolóxica e Materiais Moleculares (CiQUS) and Departamento de Química Inorgánica, Universidade de Santiago de Compostela, 15782 Santiago de Compostela, Spain

[4]Instituto de Química Orgánica General CSIC, Juan de la Cierva 3, 28006 Madrid, Spain

[5]These authors contributed equally

[6]Twitter: @MetBioCat

[7]Twitter: @bionanotools

[8]Lead Contact

*Correspondence:
joseluis.mascarenas@usc.es (J.L.M.),
pablo.delpino@usc.es (P.d.P.)
https://doi.org/10.1016/j.xcrp.2020.100076

This is especially relevant for palladium-based reagents, which can be readily degraded or deactivated when used in complex biological media.[26–29] As an alternative, there have been several attempts to use Pd nanoparticles as heterogeneous catalysts.[27,30] However, in absence of a suitable surface functionalization,[31,32] the nanoparticles tend to aggregate and suffer from Pd leaching, and their surface is easily passivated by biological components of the milieu.[27,33] On the other hand, the functionalization of nanoparticles with organic coatings, typically required to fabricate colloidally stable systems, can dramatically decrease their catalytic capability.[34]

Bradley and Unciti-Broceta have nicely approached some of these issues by embedding "pristine" Pd nanoparticles within polystyrene microspheres.[35,36] This heterogeneous formulation allowed to carry out designed uncaging reactions in biological media and even in the presence of mammalian cells; however, as the own authors noted, the solvent-exposed nanoparticles can become deactivated over time because of fouling.[37]

In an effort to avoid the passivation of the Pd surface, we engineered hollow silica microcapsules containing Pd nanoparticles in the internal cavity and demonstrated that they can be used for uncaging reactions in phosphate-buffered saline (PBS) and in the presence of added proteins. However, despite these promising results, the microcapsules were not effective in intracellular settings.[38]

Overall, achieving efficient bio-orthogonal Pd-catalyzed reactions in complex aqueous media, and especially inside living cells, stands as a challenge in research at the interface between catalysis and cell biology. More importantly, the development of robust, intracellular metallic reactors that remain active over time, and can thus process recurrent batches of reactants, is yet to be accomplished.

Metal-organic frameworks (MOFs), porous materials self-assembled from metal ions and organic ligands, have attracted attention for gas storage and biomedical applications, such as drug delivery, imaging, and biosensing.[39] In recent years, they have also demonstrated great potential in metal-promoted heterogeneous catalysis.[40,41] In this context, a number of palladium-containing MOF structures have been used as catalysts to promote hydrogenations,[42] oxidations,[43] and even C-C bond-forming processes.[44] Not surprisingly, most of these MOF-promoted reactions have been carried out in organic solvents and under water-free conditions, due to the well-known sensitivity of most MOF architectures to the presence of bulk water.[45–50]

Although several MOF-based composites compatible with aqueous media have been made, for instance, for removal of pollutants from waste water,[51] their use for transition metal catalysis in aqueous milieu remains essentially unexplored.[52,53] Needless to say, they have never been used in living settings, except for a pioneering report involving MOF-supported copper nanocomposites for achieving azide-alkyne cycloadditions in presence of cells.[54] The distribution of copper nanoparticles in the MOF nanocomposite (including solvent-exposed catalytic centers), however, does not allow to discern whether the reaction occurs in the surface and/or throughout the nanocomposite.

Herein, we report water-compatible core-shell Pd/ZIF-8 nanocomposites capable of working as efficient, and long-lasting bio-orthogonal heterogeneous nanoreactors. The nanocomposite features a single Pd nanocube core (the catalyst) and a porous nanometric ZIF-8 shell (the filter) equipped with an amphiphilic polymer (PMA) (poly
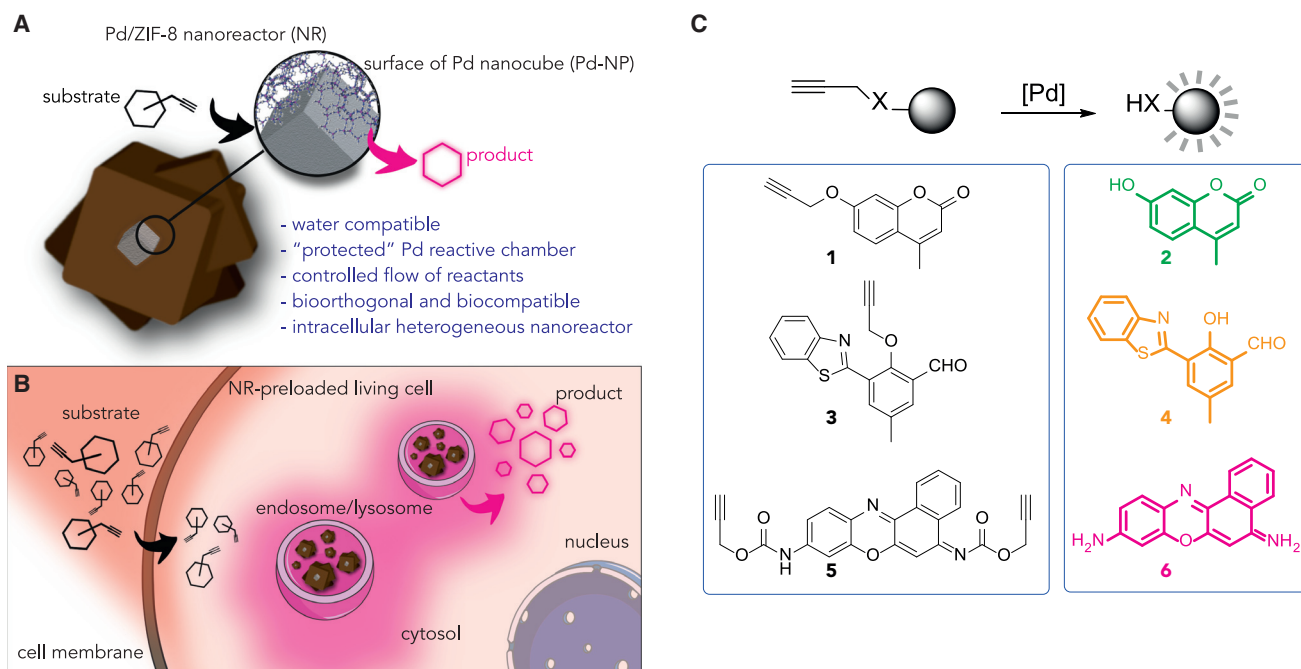
Figure 1. Core-Shell Pd/ZIF-8 Nanoreactor (NR) for Intracellular Reactions

(A) Pd nanocubes (Pd-NPs) coated by a porous ZIF-8/PMA shell are colloidally and structurally stable in water.

(B) The NRs tend to accumulate in cytosolic compartments (endosomes/lysosomes) and work as heterogeneous palladium-based nanoreactors capable of processing substrates, even in a recurrent manner.

(C) Reacting probes (substrates 1, 3, and 5) used in our study; below, their corresponding fluorescent products (2, 4, and 6) resulting from a Pd-promoted removal of their propargylic protecting groups (see Figures S1–S9 and Supplemental Experimental Procedures).

[isobutylene-alt-maleic anhydride]-graft-dodecyl). The PMA derivatization strategy renders the nanocomposite stable in aqueous media.[55] Importantly, we demonstrate that the ZIF-8/PMA architecture not only protects the Pd nanocatalyst from deactivation, leaking, and aggregation, but its porosity allows a diffusion-controlled flow of reactants within the core reaction chamber (Figure 1A). As a result, these constructs can be used as efficient metallo-nanoreactors (NRs) in complex aqueous media and inside living mammalian cells. The nanoplatforms tend to be stored in cytosolic vesicles, remaining stable, active, and accessible to the reactants (see Supplemental Experimental Procedures and Figures S1–S9), and can therefore promote consecutive reaction runs using new batches of reactants, without losing efficiency (Figures 1B and 1C). Importantly, we also demonstrate that these NRs can be readily incorporated into 3D tumor spheroids to produce tissue-like catalytic systems, which can also work in a recurrent, dose-dependent manner. This type of "catalytic tissues," which might lead to "in vivo" catalytic engineering, is also unprecedented.

RESULTS AND DISCUSSION

Design and Synthesis of the Pd/ZIF-8 Nanocomposites

Pd nanocubes (Pd-NPs from now) were selected as catalytic cores, owing to their shape-enhanced catalytic performance.[56] The selected nanocubes with side length ~24 nm (Figure S10) were synthesized in aqueous solution at room temperature (~23°C), in the presence of the cationic surfactant hexadecyltrimethylammonium bromide (CTAB), using K_2PdCl_4 as Pd source and L-ascorbic acid as reducing agent.[57] These CTAB-coated Pd-NP cores were added during the synthesis of the
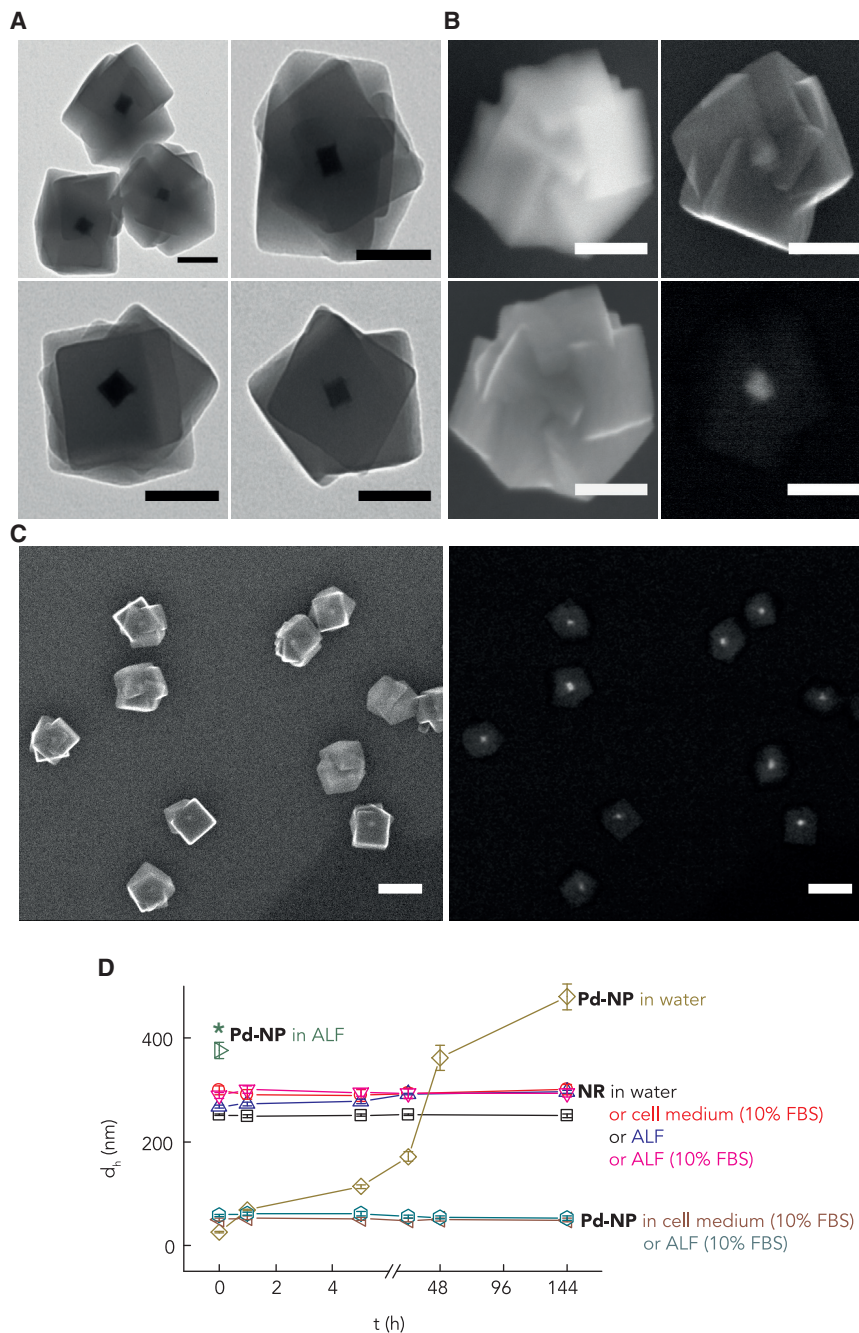
Figure 2. Characterization of the Core-Shell Pd/ZIF-8 Nanoreactors

(A) Transmission electron microscopy (TEM) micrographs confirm the core-shell Pd/ZIF-8 structure (without PMA).

(B) Scanning electron microscopy (SEM) micrographs of the same core-shell Pd/ZIF-8 particle using different detectors, at different voltages, provide depth-dependent structural and textural information. Top-left: Everhart-Thornley detector (type II, SE2, secondary electrons) at 3 kV is shown. Top-right: InLens detector (type I, SE1, secondary electrons) at 20 kV is shown. Down: AsB detector (backscattered electrons) at 3 kV (left) and 20 kV (right) is shown.

(C) SEM micrographs of PMA-derivatized Pd/ZIF-8 nanocomposites (NRs) using two detectors at 20 kV (left: InLens detector, secondary electrons; right: AsB detector, backscattered electrons).

(D) Mean d_h of NRs and Pd-NPs in different media: water, 10% FBS supplemented cell medium, artificial lysosomal fluid (ALF), and 10% FBS supplemented ALF. * indicates immediate, irreversible

ZIF-8, enabling the formation of core-shell Pd/ZIF-8 particles with average size ~250 nm (Figures 2A, 2B, and S11). This synthetic approach allows fabricating one Pd/ZIF-8 particle per Pd-NP seed, as shown by electron microscopy. Pd/ZIF-8 particles exhibit the characteristic Bragg peaks of ZIF-8 and Pd^0, as shown by powder X-ray diffraction (PXRD) (Figure S12; Table S1). Importantly, the resulting nanosystems were post-functionalized with the amphiphilic polymer PMA, in order to introduce aqueous stability.

Albeit related core-shell metal NP/ZIF-8 composites have been previously reported using other surfactants,[58] or different nanoparticle cores,[59] the inherent aqueous instability of ZIF-8 is well known; indeed, this ZIF-8 characteristic has been used for the progressive release of encapsulated drugs inside cells.[48,60–62] Notice that, when such composites are internalized into cells, they tend to accumulate in lysosomes, where the acidic pH accelerates the ZIF-8 degradation and hence the release of the drug. Such aqueous instability is, however, incompatible with the potential use of these nanostructures as biocompatible heterogeneous catalysts.

Our PMA-modified Pd/ZIF-8 nanocomposites (in the following referred to as NRs; Figure 2C) with ζ-potential ~−30 mV are colloidally stable in aqueous solution, as well as in supplemented (10% fetal bovine serum [FBS]) cell medium and in artificial lysosomal fluid (ALF) (plain or supplemented with 10% FBS). Dynamic light scattering (DLS) demonstrates that they remain stable for at least 1 week (hydrodynamic diameter [d_h] ~250 nm; see Figures 2D and S13; Table S2). In contrast to our NRs, Pd-NPs (equivalent to the Pd cores of NRs) rapidly aggregate and precipitate in water or ALF buffer, albeit they remain colloidally stable in supplemented cell medium or supplemented ALF (Figure 2D), likely due to the adsorption of serum proteins.

Inductively coupled plasma mass spectrometry (ICP-MS) was used to corroborate the Pd content before and after the ZIF-8 coating (Table S3), as well as to quantify the amount of Pd per Pd/ZIF-8 particle (3.8 wt %). Taking geometrical and structural considerations regarding the Pd-NPs used herein,[56,63] we estimate that ~5% of the Pd content of one Pd-NP are surface atoms (surface Pd) and thereby potentially available for the catalytic processes (Table S4). Importantly, although the specific surface area of the NRs decreases after PMA-modification,[55] likely because the PMA partially fills voids in the nanostructure, the ZIF-8 shell remains porous and accessible for small molecule loading by diffusion, as demonstrated with model fluorescent probes (Table S5; Figure S14).

NR-Catalyzed Removal of Propargylic Groups in Aqueous Solution

With the water-compatible Pd/MOF structures (NRs) at hand, we tested their catalytic performance in the depropargylation of the coumarin derivative 1 (Figure 1C). This is a reaction that we had already studied with discrete Pd complexes[29] and with hollow nanocapsules[38] and therefore represents an excellent reference to assess and compare the transformative potential of our system.

Gratifyingly, when the propargyl-protected coumarin 1 (10 μM) was mixed with the NRs in water/methanol (9:1) at 37°C for 15 h, we observed a smooth formation of the fluorescent coumarin 2 (89% using 50 mol % of surface Pd and 97% using 100 mol %;

aggregation and precipitation. Note: using water with 10% MeOH, instead of only water, the colloidal stability of the NRs is similar. The error bars represent 2σ value for each datapoint (σ, SD of the diameter mean value as obtained from three repetitions of the measurement). Scale bars are 200 nm.
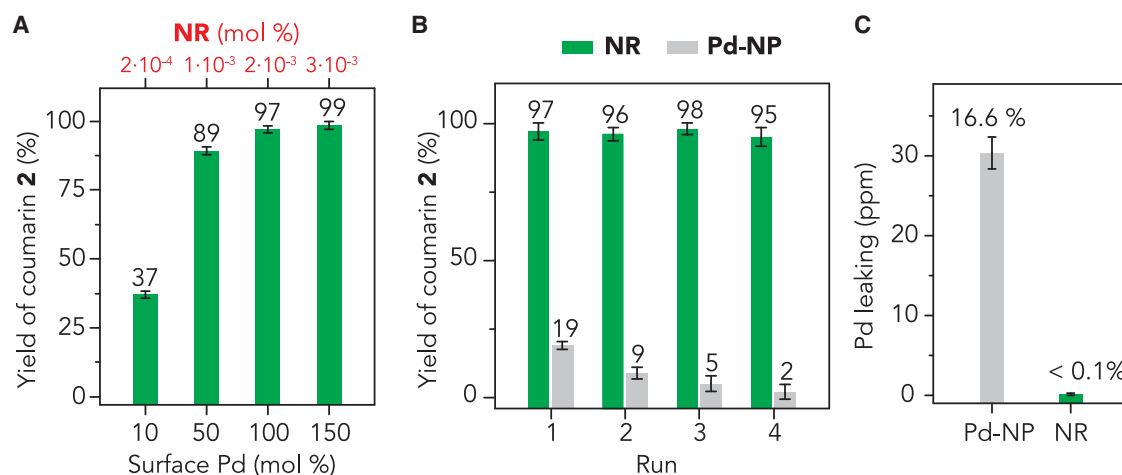
Figure 3. Characterization of the Pd-Promoted (NR or Pd-NP) Depropargylation of Pro-coumarin 1 in Aqueous Solution

(A) Yield (%) of 2 using increasing concentrations of the NRs and, therefore, of surface Pd (10%, 50%, 100%, and 150% mol surface Pd); reaction conditions: 10 μM of 1, H_2O:MeOH 9:1, 37°C, 15 h.

(B) Reusability comparison between NRs and Pd-NPs; reaction conditions: 100% mol surface Pd, 10 μM of 1, H_2O:MeOH 9:1, 37°C, 15 h.

(C) Pd leaking after one run.

The error bars represent 2σ value for each datapoint (σ, SD, calculated from three independent measurements).

Figure 3A; Table S6). With lower amounts of the NRs (10 mol % surface Pd), the reaction is slower but also effective (37% or 99% yield after 15 h or 7 days, respectively; Table S7), confirming that the nanocomposite behaves as a true catalyst. Notice that we quantified the amount of generated product in the supernatant of the reaction mixture after precipitation of our NRs; therefore, we also considered the washing steps required to fully recover the generated product (Table S8).

The NR-promoted deprotection of 1 can also be carried out in PBS/MeOH (9:1) instead of water/methanol (9:1), leading to similar results. A control experiment using similar ZIF-8 particles lacking the Pd core confirmed the need of the Pd core to promote the depropargylation reaction (Table S6).

Remarkably, pristine Pd-NPs, under identical conditions, led to much more modest yields, which could be in part explained in terms of their poor colloidal stability (Figures 3B and S15). Indeed, although the Pd content of the NRs remained virtually unaltered, in the case of the Pd-NPs, their integrity was significantly disrupted after just one cycle (>16% Pd leaking; Figure 3C; Table S9). Importantly, the NRs can be recycled without compromising their catalytic activity, as corresponds to a true heterogeneous nanocatalyst. Indeed, as shown in Figure 3B, after four runs of overnight reaction with 1, the NRs were just as effective as in the first round. In contrast, Pd-NPs gradually lost efficacy after each use, which is in consonance with their poor colloidal stability under the reaction conditions (Figure 3B; Table S10).

We also explored the uncaging of the propargyl derivative of 2-(2′-hydroxyphenyl) benzothiazole (3; Figure 1C), a probe that emits light at longer wavelengths. Surprisingly, in this case, the reaction did not proceed; however, it can be achieved with pristine Pd-NPs (15% yield after 15 h; Table S6). Although this result could be considered unsatisfactory, it is rather valuable from a mechanistic perspective. DLS data resulting from exposing the NRs to 1 and/or 3 suggest that the lack of reaction in the case of substrate 3 is likely due to the coordination of the thiazole nitrogen atom to the unsaturated Zn^{2+} ions of the ZIF-8 surface, an interaction that prevents the
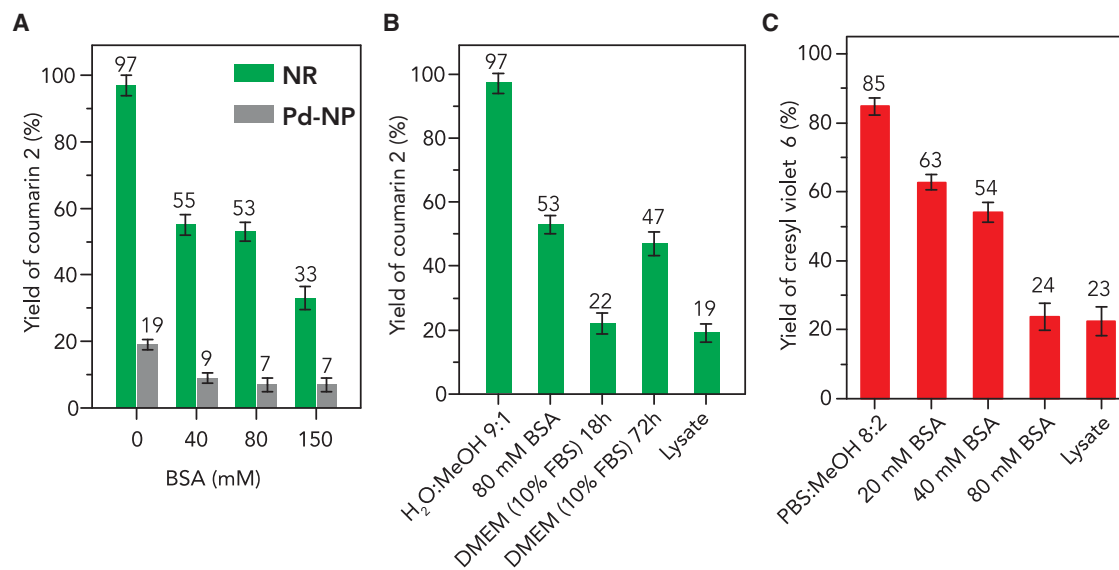
Figure 4. Characterization of the Pd-Promoted (NR or Pd-NP) Generation of Fluorophores 2 or 6 in Biological Media

(A) Yield of coumarin 2 in the presence of increasing concentrations of BSA (10 μM of 1, 37°C, 15 h).

(B) Yield of 2 in the presence of media of increasing biocomplexity (10 μM of 1, 37°C, 15 h unless otherwise noted).

(C) NR's performance as catalyst for the depropargylation of 5 in the presence of media of increasing biocomplexity (10 μM of 5, 37°C, 15 h). In all the cases, the concentration of NR or Pd-NP was kept constant at 0.23 nM, ≈100 mol % surface Pd.

The error bars represent 2σ value for each datapoint.

penetration of the substrate into the reaction chamber (Table S11). In consonance, adding one equivalent of the benzothiazole 3 to the reaction of pro-coumarin 1 with the NRs compromises the reaction rate, albeit still allowing the formation of product 2 in 54% yield (after 15 h) and in quantitative yield after 72 h (Table S6; Figure S16). These observations confirm the filtering role of the ZIF-8 shell; that is, only substrates that can permeate through the porous structure will be able to reach the nanoreactor's core. Therefore, the MOF structure not only protects the reactive Pd core but also allows discrimination among reactants, which might be especially relevant in terms of orthogonality.

As expected, the NRs can efficiently promote the depropargylation of other precursors that do not feature zinc coordinating moieties, even in substrates containing two propargyl caging groups. This is the case of the bis-protected cresyl violet 5 (Figure 1C). We observed a similar reaction trend than with the pro-coumarin 1 in terms of yield, reusability, and turnover number (TON) (Table S7). Additionally, we confirmed that the reaction exclusively affords the fully deprotected cresyl violet 6, with no traces of monopropargylated intermediates (Figure S17). In this case, we also tested consecutive reaction runs using the same NRs (10 μM surface Pd) and adding the substrate 5 (10 μM) up to three times separated by ~18 h. The cumulative yield of the product 6 (>250%; Table S12) demonstrates the feasibility of the NRs to work as true heterogeneous flow nanoreactors.

Bio-orthogonality

The shell-based architecture of the microporous ZIF-8 structure allows not only to protect the Pd core from colloidal degradation and/or Pd leaking but also filters large components of biological mixtures, thereby partially preventing Pd inactivation by biomolecule adsorption. As shown in Figure 4A, the reaction of the propargylated coumarin 1 tolerates the presence of excess amounts of bovine serum

albumin (BSA). Even using very high BSA concentration (150 µM; i.e., ~75 × 10^3 molecules of BSA per NR particle), four times more than typically contained in supplemented cell media, the reaction yield was over 30% (after 15 h). Using pristine Pd-NPs instead of our NRs, the yields are low (<10%).

The NRs are also effective in media of higher complexity, such as Dulbeccós modified Eagle's medium (DMEM) supplemented with 10% FBS, or HeLa cell lysates, albeit the reaction yields after 15 h were modest (Figure 4B). However, leaving the reaction in DMEM (10% FBS) for a longer time (72 h), the yield increases up to 47%, which confirms the ability of the NR to remain active for long periods, even in a crowded molecular environment. Analogous bio-orthogonality experiments using the cresyl violet precursor 5 led to similar results (Figure 4C; Table S13).

Intracellular Reactions

Having demonstrated and quantified the catalytic performance of our Pd/MOF particles in aqueous media with increasing biocomplexity, our next aim consisted of demonstrating that such chemistry can be performed inside living mammalian cells. Toward this end, we first carried out viability studies using HeLa cells supplemented with different concentrations of either the NRs, Pd-NPs, and/or the bispropargyl carbamate-protected cresyl violet 5 (Figure S18). This allowed us to set the range of concentrations for substrates and reagents compatible with >90% cell viability (24 h incubation, ≤2 µM in surface Pd, equivalent to ≤50 pM NRs; ≤45 µM bispropargyl carbamate-protected cresyl violet 5). The pristine Pd-NPs did not impair viability in the concentration range studied here (0.3–167 µM in surface Pd content, equivalent to 7 pM–4 nM Pd-NPs). Control experiments with cresyl violet (6; expected product of the intracellular depropargylation) revealed a higher toxicity than the protected precursor (using 0.6 µM; ~25% viability after 24 h incubation; Figure S18).

Cell uptake experiments with fluorescently labeled NRs (50 pM) confirmed an efficient internalization and the accumulation in the endocytic compartments (endosomes or lysosomes) after 12 h (Figure S19). ICP-MS was used to quantify the average Pd content (Table S14), which thereby allowed us to estimate the average number of NRs per cell (~120). We also quantified the amount of internalized Pd when using Pd-NPs instead of the NRs, resulting in a decreased intracellular Pd content (~71 Pd-NPs) per cell, which is not surprising, owing to the poorer colloidal stability of the pristine Pd-NPs.

The Pd-promoted reactions were performed by first incubating the cells with the NRs (~50 pM, equivalent to 2 µM in surface Pd, overnight) to obtain NR-preloaded cells. Before adding the substrate 5, cells were extensively washed with PBS to ensure that non-internalized or membrane-bound particles were removed.

Due to the toxicity profile of the cresyl violet 6, we used confocal microscopy to test different substrate concentrations and incubation times (Figures S20–S24); as a control, cresyl violet was also added to cells without NRs to confirm its intracellular distribution by confocal microscopy (Figure S25). We were glad to observe that, after incubating NR-preloaded cells for 6 h with 2.5 or 10 µM of 5, there is a clear dose-dependent buildup in cellular fluorescence associated to the production of 6 (Figure 5A). Not surprising, when using higher concentrations of 5, we started to observe certain toxicity, as we generate more product. Indeed, there is a similar impair (~50%) in cell viability after 24 h, when cells are exposed to 0.15 µM of cresyl violet 6 (the product), or by addition of 10 µM of the bisprotected precursor 5 to
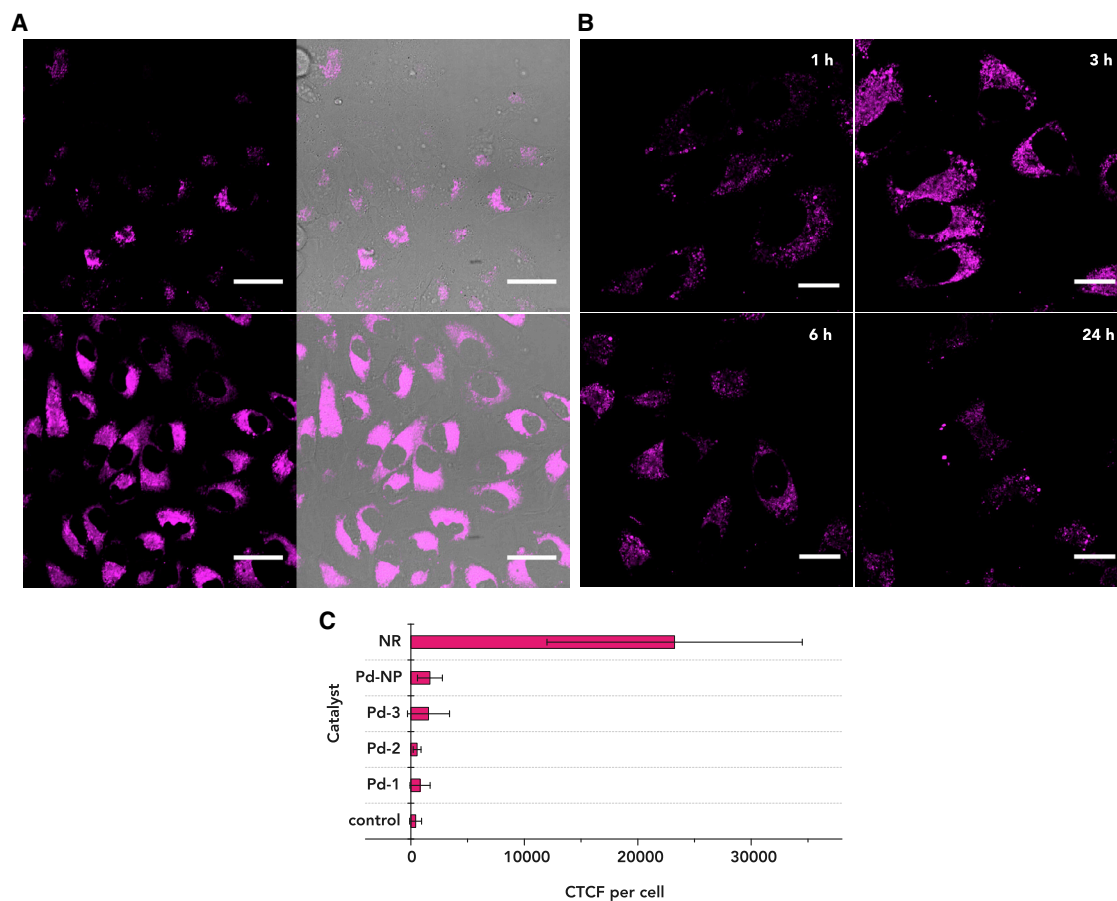
Figure 5. NR-Promoted Intracellular Depropargylation Reactions

(A) Confocal microscopy images (60×) after incubation of NR-preloaded cells with different concentration of substrate 5 (top: 2.5 μM; down: 10 μM; 60×; the fluorescence corresponds to the intracellular production of cresyl violet 6).

(B) Confocal images (100×) after incubation of 5 (10 μM) with NR-preloaded cells at different incubation times (1–24 h).

(C) Comparison of the intracellular fluorescence generated in the reactions of substrate 5 (corrected total cell fluorescence [CTCF] per cell) achieved by our NR or other palladium reagents (Pd-NPs; Pd-1: [Pd(allyl)Cl]$_2$; Pd-2: [(PPh$_3$)Pd(allyl)Cl]; or Pd-3: [PdCl$_2$(TFP)$_2$]), using equivalent incubation conditions (2 μM of Pd overnight) and cell treatment (PBS washings and incubation with of 10 μM of substrate 5 during 6 h); at least 35 cells per catalyst were analyzed (see Figure S26).

In (A), images on the right panel correspond to merged images (bright-field plus fluorescence channels). The error bars represent 2σ value for each datapoint (σ, SD, calculated from at least 35 cells per catalyst). In all cases, cells pretreated with the palladium reagents were washed with PBS (three times) before adding fresh medium and the substrates. Scale bars correspond to 20 μm (100×) or 40 μm (60×).

NR-preloaded cells. This result can be viewed as a NR-promoted generation of a cytotoxic product.

Interestingly, when the reaction of 5 (10 μM) was analyzed at different incubation times (1, 3, 6, and 24 h), we observed a fluorescence maximum intensity around 3 h, whereas, after 24 h, there is a significant decrease in emission (Figure 5B). This result suggests that the product 6 is slowly expelled out of the cells.

We should acknowledge at this point that Pd-NPs (~50 pM, equivalent to ~2 μM in surface Pd, overnight), which lack the MOF shell, also promoted the intracellular generation of cresyl violet (6). However, as expected from the test tube experiments, the efficiency was considerably lower than with the NRs (Figure S26). This is also reflected from the less impaired viability (that is, less cresyl violet production from 5) in cells pretreated with Pd-NPs than with our NRs (Figure S18).

To further assess the real potential of our palladium nanoreactors, we carried out equivalent cellular reactivity studies using three state-of-the-art Pd homogeneous catalysts: Pd-1 ([Pd(allyl)Cl]$_2$);[26] Pd-2 ([(PPh$_3$)Pd(allyl)Cl]);[29] and Pd-3 ([PdCl$_2$(TFP)$_2$]).[30] In consonance with previous reports on related depropargylation reactions, these homogeneous catalysts showed only marginal activity in the intracellular uncaging of 5 (2 μM Pd; overnight incubation; Figure S26). A comparative analysis using a fluorescence readout (corrected total cell fluorescence [CTCF] per cell) confirmed that our NRs outperform these catalysts, leading to CTCF per cell ~15 times higher than those obtained with Pd-2, which was the best among these complexes (Figures 5C and S26). The reasons for this improved performance of our metallo-nanoreactors inside living cells must be related to the core-shell nano-architecture in which the MOF-based shell plays a critical role to protect the metal reactive chamber from deactivation while providing for a controlled flow of reactants.

Diffusion-Controlled Core-Shell Pd/ZIF-8 as Recurrent Intracellular Nanoreactors

The above studies confirm that the designed Pd/MOF nanocomposites are readily internalized into mammalian cells and are capable of promoting intracellular depropargylation reactions. We then envisioned that the core-shell, microporous structure of our constructs could allow an efficient flow of reagents and products without damage to the core catalytic Pd, and therefore, the Pd/ZIF-8 platforms might work as recyclable nanoreactors. Accordingly, we examined the feasibility of reusing the nanocatalyst-loaded cells, which can be especially relevant in terms of accomplishing the long-term goal of developing "catalytic cellular implants."

Given that product 6 seems to be readily washed out of the cells, we explored the viability of using our Pd/MOF platforms as recurrent (flow) intracellular nanoreactors (Figure 6A). Therefore, the NR-preloaded cells were incubated during 3 h with the substrate 5 (20 μM = run-1) as previously discussed, and the intracellular formation of cresyl violet 6 after 3 h was confirmed by confocal microscopy (Figure 6B, left). Cells were then washed twice with PBS to remove extracellular substrates/products and mixed with fresh cell medium to facilitate the cleansing of product 6 and of remaining reactants. Indeed, after 3 h of cleansing, there is almost no intracellular fluorescence (Figure 6B, right), whereas cell viability does not appear significantly affected; that is, similar cell densities were observed. Notice that, although in the experiments shown in Figure 5B, there are not washing steps before confocal inspection, in the experiments of Figure 6 (cleansing panels), cells were washed after 3 h of incubation. This allows removing products and creates a concentration gradient that further promotes the extracellular release and the cleansing process. Next, cells were incubated with a second dose of substrate 5 (20 μM = run-2) during 3 h. We observed again a rise up of fluorescence associated to the production of 6 (Figure 6C, right), which was cleared by the cells after the cleansing treatment (run-2/cleansing; Figure 6C, left). We repeated this protocol up to 4 cycles (Figure 6; additional images in Figure S27) with similar outcomes, which demonstrates the robustness of our heterogeneous nanoreactors to perform dose-dependent, sustained intracellular transformations. For completeness, we also attempted equivalent experiments with either the pristine Pd-NPs or the homogeneous catalysts (Pd-1, Pd-2, and Pd-3). Not surprisingly, these reagents, which already performed poorly in a first cycle, were unable to sustain a second reaction cycle (Figure S26). These results further corroborate the unique performance of our NRs in this type of recurrent reactivity and represent a first approach to the development of reusable "catalytic cells."
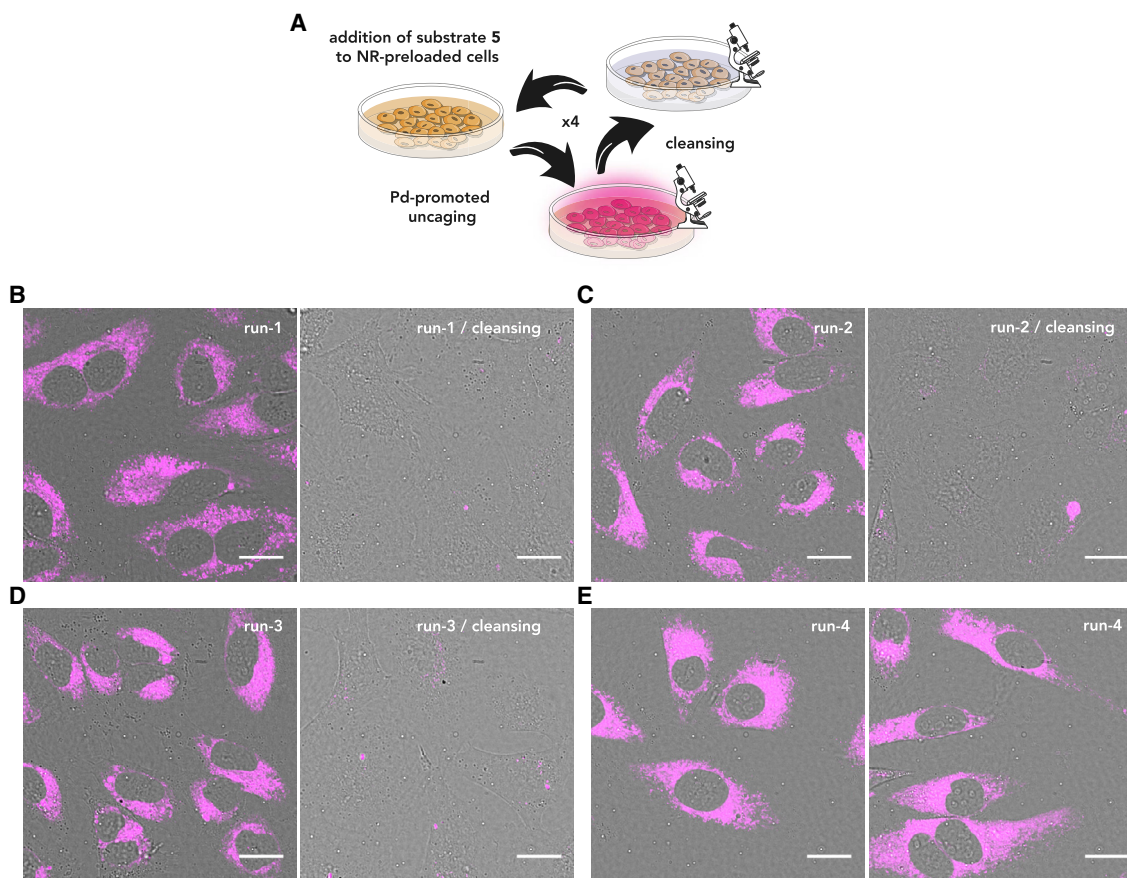
Figure 6. NR-Preloaded Cells Working as Recurrent "Flow" Nanoreactors

(A) Reusability scheme (4 cycles) demonstrated for the deprotection of precursor 5.

(B–D) First, second, and third reaction runs using the same NR-preloaded cells and recorded by confocal microscopy; left: after 3 h incubation with 5; right: after washing (2xPBS) and leaving the cells for 3 h for further cleansing (see main text).

(E) Two images of the fourth deprotection run of precursor 5 with the same NR-preloaded cells.

In (B)–(E), confocal images (100✕) correspond to merged channels: bright-field plus fluorescence. Scale bars correspond to 20 μm (100✕).

3D Spheroid Catalytic Model

Having demonstrated the potential of our NRs to carry out intracellular depropargylation reactions in adherent 2D cultured cells and the viability of using these NR-containing cells in a recurrent manner, we questioned whether the reactivity could be exported to tissue-like models. This would be an important step to further narrowing the frontier between transition metal catalysis and cellular biology and biomedicine. In particular, we wondered whether it would be possible to build 3D tissue-like systems containing our NRs and whether these cellular networks could be capable of performing the designed metal-promoted reactions. We chose 3D tumor spheroids as models of avascular tissues (Figure S28), as they are widely used in cancer research as intermediate models between *in vitro* cancer cell line cultures and *in vivo* tumors.[64]

To test the viability of building these spheroids, we first used NRs in which the PMA contains a rhodamine tag, in order to facilitate the analysis by confocal microscopy. Therefore, HeLa cells were loaded with these NRs as previously discussed and grown in agarose templates for 24 h (Figure S29). Microscope inspection of the cell cultures confirmed the presence of the desired 3D structures (developed from an initial density of $\sim 1 \times 10^4$–3×10^4 cells per spheroid, which presented a diameter ~ 0.4–1 μm).
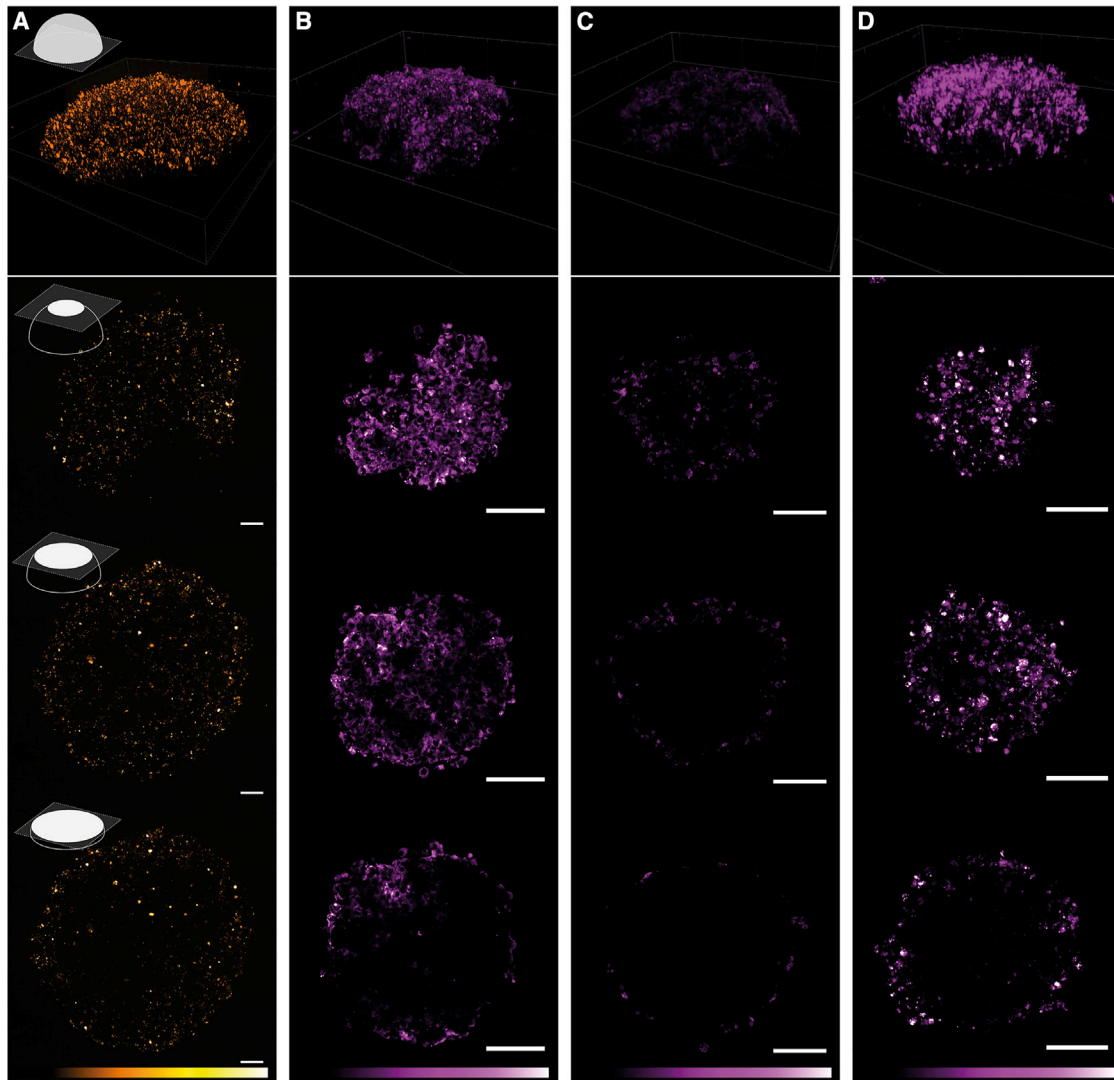
Figure 7. NR-Preloaded 3D Spheroids Working as Recurrent Flow Tissue-like Reactor

(A) Top: 3D reconstruction of confocal microscopy z-scans of a NR-preloaded spheroid; NRs were fluorescently labeled (i.e., PMA was covalently modified with a rhodamine tag). Bottom: three individual scans at different depths are shown, illustrating the homogeneous distribution of the NRs throughout the spheroid volume.

(B) Top: 3D reconstruction of confocal microscopy z-scans of a NR-preloaded spheroid 24 h after incubation with substrate 5 (20 µM), showing the fluorescence resulting from the generation of 6. Bottom: three individual scans at different depths are shown, illustrating the non-homogeneous "crust-like" distribution of 6 throughout the spheroid volume.

(C) Top: 3D reconstruction of confocal microscopy z-scans of a NR-preloaded spheroid, which, after one reaction run with 5, was washed with PBS (three times) and incubated for 24 h in fresh cell media, which led to cleansing of the spheroid. Bottom: three individual scans at different depths are shown to illustrate the cleansing process at different depths.

(D) Top: 3D reconstruction of confocal microscopy z-scans of a NR-preloaded spheroid, which, after one reaction run with 5 (24 h) and the cleansing step (24 h), was gain incubated with more substrate (5; 20 µM). Bottom: three individual scans at different depths are shown, illustrating the non-homogeneous "crust-like" distribution of fluorescence (from 6) throughout the spheroid volume.

3D reconstructions were done with ~300 stack images (total thickness ~150 µm; step thickness ~0.5 µm). Scale bars correspond to 100 µm (20✕).

Importantly, we observed a homogeneous distribution of the NRs inside the cells of the spheroids (Figure 7A).

Following the same procedure, we synthesized homologous spheroids using NRs without the fluorescent label, and their reactive potential was analyzed in the

depropargylation of bis-propargylated probe 5 (Figure S30). Excitingly, when the NR-loaded spheroids were incubated with 5 (20 µM) for 24 h, we observed a clear buildup of fluorescence corresponding to product 6 (Figure 7B). Curiously, and in contrast to the homogeneous distribution of the rhodamine-labeled NRs (Figure 7A), the fluorescence arising from 6 is non-homogeneous but mostly concentrating as a thick "crust" in the spheroid. This result is not surprising, and it is very likely due to the diffusion-limited distribution of the substrate 5, which prefers to enter the cells located in the more external layer of the tissue model, so that the fluorescent product is generated in these regions. It is important to note that tumor spheroids are in fact suitable models to reproduce the heterogeneity of environments within solid tumors: decreasing chemical gradients of nutrients from the outermost cells to the hypoxic core of the spheroid.

After one run, as previously discussed for the 2D cell experiments, NR-loaded spheroids were washed with PBS (three times) to remove extracellular substrates/products and fresh cell media was added, which facilitated the cleansing of 6 (for 24 h; Figure 7C). The resulting NR-loaded spheroids were again incubated with 5 (20 µM) during 24 h. Gratifyingly, we observed a new rise up of fluorescence associated to the production of 6 (Figure 7D), which is again mainly concentrated in the crust.

These results represent the first demonstration of a transition-metal promoted reaction carried out in a living tissue model. Excitingly, these spheroids can be considered as recyclable "catalytic tissues," a concept without precedent, which might have profound implications in the future development of "catalytic cellular or tissue implants."

We have demonstrated the feasibility of using Pd/ZIF-8 nanocomposites as intracellular heterogeneous metallo-catalysts. In contrast to other MOF-metal hybrids, which present active metals in the surface, our core-shell Pd/ZIF-8 architecture ensures that the reaction occurs in a core reaction chamber, which is critical for the biological application. The ZIF-8-based shell plays a critical role to preserve the integrity of the catalytic chamber while providing for orthogonality (substrate selectivity) and biocompatibility. Excitingly, our heterogeneous nanoplatforms can process sequential batches of reactants when loaded in cells, both in the form of 2D monolayers or as 3D tumor spheroids. This represents a pioneering demonstration of intracellular recurrent nanoreactors and may set the basis for the development of "catalytic cellular or tissular nanoimplants." To provide a comprehensive picture of the catalytic behavior of our NRs inside living cells and tissues, further work will be necessary to analytically determine the amount of intracellularly generated product, thereby making it possible to calculate and optimize TONs.

The versatility of the nanobuilding technology promises a straightforward access to other related nanocomposites (for instance, by integrating other metal[s] clusters or NPs and/or metal-organic-framework-based shells), which could operate as multifunctional nanoreactors in biological settings, and promotes many other abiotic reactions in living environments.

EXPERIMENTAL PROCEDURES
Resource Availability
Lead Contact
Further information and requests for resources and reagents should be directed to and will be fulfilled by the lead contact, Pablo del Pino (pablo.delpino@usc.es).

Materials Availability

All unique/stable reagents generated in this study are available from the lead contact with a completed Materials Transfer Agreement.

Data and Code Availability

The main data supporting the findings of this study are included in the paper and its Supplemental Information file. Additional raw data (NMR spectra, mass spectra, and so on) are available from the lead contact on reasonable request.

Synthesis of Probes

The compounds propargyl-protected coumarin 1, propargyl-protected 2-(2′-hydroxyphenyl) benzothiazole 3, and bis-propargyl carbamate-protected cresyl violet 5 were synthesized following known procedures (see the Supplemental Experimental Procedures).[28,65–67]

Preparation of PMA-Modified Pd/ZIF-8 Nanocomposites (NRs)

The here-designed and studied NRs consisted of a Pd-NP core and a ZIF-8 shell, which was further functionalized with a polymer (PMA). The synthetic method involved three main steps: (1) CTAB-coated Pd nanocubes enclosed by {100} facets were first synthesized using K_2PdCl_4 as precursor, L-ascorbic acid as reducing agent, and hexadecyltrimethylammonium bromide (CTAB) as capping agent and stabilizer. (2) These Pd-NPs were then used as seeds onto which a shell of ZIF-8 was grown by following an aqueous procedure in which the surfactant CTAB works as size-controlling and structural-directing agent. (3) Finally, in order to provide colloidal stability in diverse complex aqueous media, these Pd/ZIF-8 core-shell particles were wrapped with the amphiphilic polymer PMA by following a recently described protocol;[55] alternatively, PMA was covalently modified with a rhodamine (specifically, we used 5(6)-TAMRA cadaverine) for fluorescence labeling of our NRs, as previously reported for analogous plasmonic nanocomposites.[55]

Characterization Techniques

Scanning electron microscopy (SEM) and transmission electron microscopy (TEM) were used to study the size and morphology of the nanomaterials. SEM images were acquired with a FESEM Zeiss Ultra Plus operated at 3 kV and 20 kV. TEM images were acquired with a JEOL JEM-2010 microscope operated between 80 and 200 kV accelerating voltage. ImageJ free software and Origin software were used for the size measurements and distribution analysis, respectively. Mass spectra were acquired using IT-MS Bruker AmaZon SL and using electrospray ionization (ESI). UV-Vis absorption spectra and fluorescence spectra were acquired using Jasco V-670 spectrometer and Varian Cary Eclipse fluorescence spectrofluorometer, respectively. An X-ray diffractometer Philips was used to study the crystallinity of the samples, operating in the range of 2θ between 2° and 75° with a passage of 0.02° and a time by step of 2 s. A Malvern Zetasizer (Nano ZSP) instrument, equipped with a 10 mW He-Ne laser operating at a wavelength of 633 nm and fixed scattering angle of 173°, was used to measure the hydrodynamic diameters (by DLS) and the zeta potentials (by laser Doppler anemometry [LDA]). Inductively coupled plasma mass spectrometry (ICP-MS) measurements were performed using an Agilent 7700x ICP-MS after acidic digestion of the samples with aqua regia. Reverse-phase high-performance liquid chromatography-diode array detector/mass spectrometry (RP-HPLC-DAD/MS) analysis was done by using Thermo Dionex Ultimate 3000 coupled with a MSD Bruker AmaZon SL.

General Procedures for the Depropargylation Reactions

The reaction with the NRs or with Pd-NPs in aqueous solution was performed as follows: 1, 3, or 5 (8 μL; 0.5 mM stock solution in MeOH) was added to a H_2O:MeOH 9:1 solution (342 μL of the reaction medium; H_2O:MeOH 8:2 solution for substrate 5) in a 1.5 mL HPLC vial (containing a stirring bar), followed by addition of an aqueous solution of Pd-NPs or NRs (50 μL, 2 nM, unless otherwise specified; this corresponds to 10 μM of surface Pd). Reactions were carried out overnight under continuous stirring (400 rpm) at 37°C. Afterward, the particles were collected by centrifugation (7,000 RCF; 10 min) and washed with 400 μL of reaction medium, and the generated product (supernatant) was quantified by fluorescence.

Parameters such as the catalyst concentration, the influence of washing steps, and the presence of bio-additives in the reaction medium were studied and evaluated. Potential leaking of Pd during the reaction was determined by ICP-MS of the supernatants. Procedures for obtaining kinetic curves and TONs and testing the reusability of the particles (Pd-NPs or NRs) are described in the Supplemental Information. Each experiment was performed at least in duplicate, and the values given correspond to the mean value $\pm$ standard deviation (SD) of n $\geq$ 2. Each measurement was taken from distinct samples. R^2 is the coefficient of determination, used as statistical parameter of goodness of fit in the calibration curves. Data analysis was performed using OriginPro 8 statistical software.

Cell Studies

We confirm that the biological material involved in the study (cervical cancer cell line—HeLa) are readily available from standard commercial source (ATCC). A standard experiment consists of incubation of HeLa cells with the NRs or Pd-NPs (~50 pM, equivalent to ~2 μM in surface Pd) overnight (~12 h). In all the cell studies, before adding the substrate (5) or resazurin (for cell viability studies; Figure S18), non-internalized nanostructures were washed out from the cell culture. In the intracellular depropargylation of 5, before confocal inspections, washing of extracellular probes (substrates and/or products) was not required.

Spheroids of HeLa cells and NR-loaded HeLa cells were produced by adapting the application note provided by Ibidi (i.e., generation of spheroids), that is, the manufacturer of the wells that we used for spheroid culture and confocal microscopy. As in the 2D cell studies, cells were incubated with the NRs (~50 pM, equivalent to ~2 μM in surface Pd) overnight (~12 h). Then, before generating the spheroids, non-internalized NRs were washed out from the cell culture. In the case of the intra-spheroid depropargylation of 5, before confocal inspections, extracellular probes (substrates and/or products) were removed by washing with PBS three times.

Cells were imaged with an Andor Dragonfly spinning disk confocal system mounted on a Nikon TiE microscope equipped with a Zyla 4.2 PLUS camera (Andor, Oxford Instruments) and an OKO-lab incubator to keep cells at 37°C during all the experiments. Images were taken with different magnification objectives (60✕ and 100✕). Excitation/emission wavelengths used for confocal imaging of the rhodamine-labeled NRs/product 6 are 561/620 (60).

SUPPLEMENTAL INFORMATION

Supplemental Information can be found online at https://doi.org/10.1016/j.xcrp.2020.100076.

ACKNOWLEDGMENTS

AUTHOR CONTRIBUTIONS

R.M., C.C.-C., P.D., A.A., and M.T.-G. prepared and characterized the materials and reactants and did data analysis. R.M. performed the experiments *in vitro*. C.C.-C., B.P., F.L., J.L.M., and P.d.P. conceived the idea and designed the research. All authors contributed to results, discussion, and manuscript writing.

DECLARATION OF INTERESTS

The authors declare no competing interests.

REFERENCES

1. Unciti-Broceta, A. (2015). Bioorthogonal catalysis: rise of the nanobots. Nat. Chem. 7, 538–539.

2. Völker, T., and Meggers, E. (2015). Transition-metal-mediated uncaging in living human cells—an emerging alternative to photolabile protecting groups. Curr. Opin. Chem. Biol. 25, 48–54.

3. Yang, M., Yang, Y., and Chen, P.R. (2016). Transition-metal-catalyzed bioorthogonal cycloaddition reactions. Top. Curr. Chem. (Cham) 374, 2.

4. Soldevila-Barreda, J.J., and Sadler, P.J. (2015). Approaches to the design of catalytic metallodrugs. Curr. Opin. Chem. Biol. 25, 172–183.

5. Martínez-Calvo, M., and Mascareñas, J.L. (2018). Organometallic catalysis in biological media and living settings. Coord. Chem. Rev. 359, 57–79.

6. Rebelein, J.G., and Ward, T.R. (2018). In vivo catalyzed new-to-nature reactions. Curr. Opin. Biotechnol. 53, 106–114.

7. Bai, Y., Chen, J., and Zimmerman, S.C. (2018). Designed transition metal catalysts for intracellular organic synthesis. Chem. Soc. Rev. 47, 1811–1821.

8. Soldevila-Barreda, J.J., and Metzler-Nolte, N. (2019). Intracellular catalysis with selected metal complexes and metallic nanoparticles: advances toward the development of catalytic metallodrugs. Chem. Rev. 119, 829–869.

9. Link, A.J., and Tirrell, D.A. (2003). Cell surface labeling of Escherichia coli via copper(I)-catalyzed [3+2] cycloaddition. J. Am. Chem. Soc. 125, 11164–11165.

10. Link, A.J., Vink, M.K.S., and Tirrell, D.A. (2004). Presentation and detection of azide functionality in bacterial cell surface proteins. J. Am. Chem. Soc. 126, 10598–10602.

11. Beatty, K.E., Xie, F., Wang, Q., and Tirrell, D.A. (2005). Selective dye-labeling of newly synthesized proteins in bacterial cells. J. Am. Chem. Soc. 127, 14150–14151.

12. Tiwari, V.K., Mishra, B.B., Mishra, K.B., Mishra, N., Singh, A.S., and Chen, X. (2016). Cu-catalyzed click reaction in carbohydrate chemistry. Chem. Rev. 116, 3086–3240.

13. Mahdavi, A., Hamblin, G.D., Jindal, G.A., Bagert, J.D., Dong, C., Sweredoski, M.J., Hess, S., Schuman, E.M., and Tirrell, D.A. (2016). Engineered aminoacyl-tRNA synthetase for cell-selective analysis of mammalian protein synthesis. J. Am. Chem. Soc. 138, 4278–4281.

14. Miguel-Ávila, J., Tomás-Gamasa, M., Olmos, A., Pérez, P.J., and Mascareñas, J.L. (2018). Discrete Cu(i) complexes for azide-alkyne annulations of small molecules inside mammalian cells. Chem. Sci. (Camb.) 9, 1947–1952.

15. Völker, T., Dempwolff, F., Graumann, P.L., and Meggers, E. (2014). Progress towards bioorthogonal catalysis with organometallic compounds. Angew. Chem. Int. Ed. Engl. 53, 10536–10540.

16. Williams, D.S., Atilla, G.E., Bregman, H., Arzoumanian, A., Klein, P.S., and Meggers, E. (2005). Switching on a signaling pathway with an organoruthenium complex. Angew. Chem. Int. Ed. Engl. 44, 1984–1987.

17. Streu, C., and Meggers, E. (2006). Ruthenium-induced allylcarbamate cleavage in living cells. Angew. Chem. Int. Ed. Engl. 45, 5645–5648.

18. Tomás-Gamasa, M., Martínez-Calvo, M., Couceiro, J.R., and Mascareñas, J.L. (2016). Transition metal catalysis in the mitochondria of living cells. Nat. Commun. 7, 12538–12547.

19. Vidal, C., Tomás-Gamasa, M., Destito, P., López, F., and Mascareñas, J.L. (2018). Concurrent and orthogonal gold(I) and ruthenium(II) catalysis inside living cells. Nat. Commun. 9, 1913.

20. Vidal, C., Tomás-Gamasa, M., Gutiérrez-González, A., and Mascareñas, J.L. (2019). Ruthenium-catalyzed redox isomerizations inside living cells. J. Am. Chem. Soc. 141, 5125–5129.

21. Pérez-López, A.M., Rubio-Ruiz, B., Sebastián, V., Hamilton, L., Adam, C., Bray, T.L., Irusta, S., Brennan, P.M., Lloyd-Jones, G.C., Sieger, D., et al. (2017). Gold-triggered uncaging chemistry in living systems. Angew. Chem. Int. Ed. Engl. 56, 12548–12552.

22. Tsubokura, K., Vong, K.K.H., Pradipta, A.R., Ogura, A., Urano, S., Tahara, T., Nozaki, S., Onoe, H., Nakao, Y., Sibgatullina, R., et al. (2017). In vivo gold complex catalysis within live

mice. Angew. Chem. Int. Ed. Engl. 56, 3579–3584.

23. Bose, S., Ngo, A.H., and Do, L.H. (2017). Intracellular transfer hydrogenation mediated by unprotected organoiridium catalysts. J. Am. Chem. Soc. 139, 8792–8795.

24. Coverdale, J.P.C., Romero-Canelón, I., Sanchez-Cano, C., Clarkson, G.J., Habtemariam, A., Wills, M., and Sadler, P.J. (2018). Asymmetric transfer hydrogenation by synthetic catalysts in cancer cells. Nat. Chem. 10, 347–354.

25. Jbara, M., Maity, S.K., and Brik, A. (2017). Palladium in the chemical synthesis and modification of proteins. Angew. Chem. Int. Ed. Engl. 56, 10644–10655.

26. Li, J., Yu, J., Zhao, J., Wang, J., Zheng, S., Lin, S., Chen, L., Yang, M., Jia, S., Zhang, X., and Chen, P.R. (2014). Palladium-triggered deprotection chemistry for protein activation in living cells. Nat. Chem. 6, 352–361.

27. Wang, J., Cheng, B., Li, J., Zhang, Z., Hong, W., Chen, X., and Chen, P.R. (2015). Chemical remodeling of cell-surface sialic acids through a palladium-triggered bioorthogonal elimination reaction. Angew. Chem. Int. Ed. Engl. 54, 5364–5368.

28. Wang, J., Zheng, S., Liu, Y., Zhang, Z., Lin, Z., Li, J., Zhang, G., Wang, X., Li, J., and Chen, P.R. (2016). Palladium-triggered chemical rescue of intracellular proteins via genetically encoded allene-caged tyrosine. J. Am. Chem. Soc. 138, 15118–15121.

29. Martínez-Calvo, M., Couceiro, J.R., Destito, P., Rodríguez, J., Mosquera, J., and Mascareñas, J.L. (2018). Intracellular deprotection reactions mediated by palladium complexes equipped with designed phosphine ligands. ACS Catal. 8, 6055–6061.

30. Miller, M.A., Askevold, B., Mikula, H., Kohler, R.H., Pirovich, D., and Weissleder, R. (2017). Nano-palladium is a cellular catalyst for in vivo chemistry. Nat. Commun. 8, 15906.

31. Rivera-Gil, P., Jimenez de Aberasturi, D., Wulf, V., Pelaz, B., del Pino, P., Zhao, Y., de la Fuente, J.M., Ruiz de Larramendi, I., Rojo, T., Liang, X.-J., and Parak, W.J. (2013). The challenge to relate the physicochemical properties of colloidal nanoparticles to their cytotoxicity. Acc. Chem. Res. 46, 743–749.

32. Feliu, N., Docter, D., Heine, M., Del Pino, P., Ashraf, S., Kolosnjaj-Tabi, J., Macchiarini, P., Nielsen, P., Alloyeau, D., Gazeau, F., et al. (2016). In vivo degeneration and the fate of inorganic nanoparticles. Chem. Soc. Rev. 45, 2440–2457.

33. Dahal, E., Curtiss, J., Subedi, D., Chen, G., Houston, J.P., and Smirnov, S. (2015). Evaluation of the catalytic activity and cytotoxicity of palladium nanocubes: the role of oxygen. ACS Appl. Mater. Interfaces 7, 9364–9371.

34. Gavia, D.J., and Shon, Y.-S. (2015). Catalytic properties of unsupported palladium nanoparticle surfaces capped with small organic ligands. ChemCatChem 7, 892–900.

35. Weiss, J.T., Dawson, J.C., Macleod, K.G., Rybski, W., Fraser, C., Torres-Sánchez, C., Patton, E.E., Bradley, M., Carragher, N.O., and

Unciti-Broceta, A. (2014). Extracellular palladium-catalysed dealkylation of 5-fluoro-1-propargyl-uracil as a bioorthogonally activated prodrug approach. Nat. Commun. 5, 3277–3285.

36. Yusop, R.M., Unciti-Broceta, A., Johansson, E.M.V., Sánchez-Martín, R.M., and Bradley, M. (2011). Palladium-mediated intracellular chemistry. Nat. Chem. 3, 239–243.

37. Unciti-Broceta, A., Johansson, E.M.V., Yusop, R.M., Sánchez-Martín, R.M., and Bradley, M. (2012). Synthesis of polystyrene microspheres and functionalization with Pd(0) nanoparticles to perform bioorthogonal organometallic chemistry in living cells. Nat. Protoc. 7, 1207–1218.

38. Destito, P., Sousa-Castillo, A., Couceiro, J.R., López, F., Correa-Duarte, M.A., and Mascareñas, J.L. (2018). Hollow nanoreactors for Pd-catalyzed Suzuki-Miyaura coupling and O-propargyl cleavage reactions in bio-relevant aqueous media. Chem. Sci. (Camb.) 10, 2598–2603.

39. Giménez-Marqués, M., Hidalgo, T., Serre, C., and Horcajada, P. (2016). Nanostructured metal–organic frameworks and their bio-related applications. Coord. Chem. Rev. 307, 342–360.

40. Li, G., Zhao, S., Zhang, Y., and Tang, Z. (2018). Metal-organic frameworks encapsulating active nanoparticles as emerging composites for catalysis: recent progress and perspectives. Adv. Mater. 30, e1800702.

41. Pascanu, V., González Miera, G., Inge, A.K., and Martín-Matute, B. (2019). Metal-organic frameworks as catalysts for organic synthesis: a critical perspective. J. Am. Chem. Soc. 141, 7223–7234.

42. Wan, M., Zhang, X., Li, M., Chen, B., Yin, J., Jin, H., Lin, L., Chen, C., and Zhang, N. (2017). Hollow Pd/MOF nanosphere with double shells as multifunctional catalyst for hydrogenation reaction. Small 13, 1701395.

43. Dhakshinamoorthy, A., Asiri, A.M., and Garcia, H. (2016). Metal-organic frameworks as catalysts for oxidation reactions. Chemistry 22, 8012–8024.

44. Yuan, N., Pascanu, V., Huang, Z., Valiente, A., Heidenreich, N., Leubner, S., Inge, A.K., Gaar, J., Stock, N., Persson, I., et al. (2018). Probing the evolution of palladium species in Pd@MOF catalysts during the heck coupling reaction: an operando X-ray absorption spectroscopy study. J. Am. Chem. Soc. 140, 8206–8217.

45. Liu, X., Li, Y., Ban, Y., Peng, Y., Jin, H., Bux, H., Xu, L., Caro, J., and Yang, W. (2013). Improvement of hydrothermal stability of zeolitic imidazolate frameworks. Chem. Commun. (Camb.) 49, 9140–9142.

46. Zhang, H., Liu, D., Yao, Y., Zhang, B., and Lin, Y.S. (2015). Stability of ZIF-8 membranes and crystalline powders in water at room temperature. J. Membr. Sci. 485, 103–111.

47. Howarth, A.J., Liu, Y., Li, P., Li, Z., Wang, T.C., Hupp, J.T., and Farha, O.K. (2016). Chemical, thermal and mechanical stabilities of metal-organic frameworks. Nat. Rev. Mater. 1, 15018.

48. Yan, L., Chen, X., Wang, Z., Zhang, X., Zhu, X., Zhou, M., Chen, W., Huang, L., Roy, V.A.L., Yu,

P.K.N., et al. (2017). Size controllable and surface tunable zeolitic imidazolate framework-8-poly(acrylic acid sodium salt) nanocomposites for pH responsive drug release and enhanced in vivo cancer treatment. ACS Appl. Mater. Interfaces 9, 32990–33000.

49. Yang, S., Peng, L., Sun, D.T., Asgari, M., Oveisi, E., Trukhina, O., Bulut, S., Jamali, A., and Queen, W.L. (2019). A new post-synthetic polymerization strategy makes metal-organic frameworks more stable. Chem. Sci. (Camb.) 10, 4542–4549.

50. Luzuriaga, M.A., Benjamin, C.E., Gaertner, M.W., Lee, H., Herbert, F.C., Mallick, S., and Gassensmith, J.J. (2019). ZIF-8 degrades in cell media, serum, and some—but not all—common laboratory buffers. Supramol. Chem. 31, 485–490.

51. Gao, Q., Xu, J., and Bu, X.-H. (2019). Recent advances about metal–organic frameworks in the removal of pollutants from wastewater. Coord. Chem. Rev. 378, 17–31.

52. Llabrés i Xamena, F.X., Abad, A., Corma, A., and Garcia, H. (2007). MOFs as catalysts: activity, reusability and shape-selectivity of a Pd-containing MOF. J. Catal. 250, 294–298.

53. Pascanu, V., Yao, Q., Bermejo Gómez, A., Gustafsson, M., Yun, Y., Wan, W., Samain, L., Zou, X., and Martín-Matute, B. (2013). Sustainable catalysis: rational Pd loading on MIL-101Cr-NH2 for more efficient and recyclable Suzuki-Miyaura reactions. Chemistry 19, 17483–17493.

54. Wang, F., Zhang, Y., Liu, Z., Du, Z., Zhang, L., Ren, J., and Qu, X. (2019). A biocompatible heterogeneous MOF-Cu catalyst for in vivo drug synthesis in targeted subcellular organelles. Angew. Chem. Int. Ed. Engl. 58, 6987–6992.

55. Carrillo-Carrión, C., Martínez, R., Navarro Poupard, M.F., Pelaz, B., Polo, E., Arenas-Vivo, A., Olgiati, A., Taboada, P., Soliman, M.G., Catalán, Ú., et al. (2019). Aqueous stable gold nanostar/ZIF-8 nanocomposites for light-triggered release of active cargo inside living cells. Angew. Chem. Int. Ed. Engl. 58, 7078–7082.

56. Zhang, H., Jin, M., Xiong, Y., Lim, B., and Xia, Y. (2013). Shape-controlled synthesis of Pd nanocrystals and their catalytic applications. Acc. Chem. Res. 46, 1783–1794.

57. Xie, X., Gao, G., Pan, Z., Wang, T., Meng, X., and Cai, L. (2015). Large-scale synthesis of palladium concave nanocubes with high-index facets for sustainable enhanced catalytic performance. Sci. Rep. 5, 8515.

58. Hu, P., Zhuang, J., Chou, L.-Y., Lee, H.K., Ling, X.Y., Chuang, Y.-C., and Tsung, C.-K. (2014). Surfactant-directed atomic to mesoscale alignment: metal nanocrystals encased individually in single-crystalline porous nanostructures. J. Am. Chem. Soc. 136, 10561–10564.

59. Zheng, G., de Marchi, S., López-Puente, V., Sentosun, K., Polavarapu, L., Pérez-Juste, I., Hill, E.H., Bals, S., Liz-Marzán, L.M., Pastoriza-Santos, I., and Pérez-Juste, J. (2016). Encapsulation of single plasmonic nanoparticles within ZIF-8 and SERS analysis of the MOF flexibility. Small 12, 3935–3943.

60. Nabipour, H., Sadr, M.H., and Bardajee, G.R. (2017). Synthesis and characterization of nanoscale zeolitic imidazolate frameworks with ciprofloxacin and their applications as antimicrobial agents. New J. Chem. *41*, 7364–7370.

61. Kaur, H., Mohanta, G.C., Gupta, V., Kukkar, D., and Tyagi, S. (2017). Synthesis and characterization of ZIF-8 nanoparticles for controlled release of 6-mercaptopurine drug. J. Drug Deliv. Sci. Technol. *41*, 106–112.

62. Chen, X., Tong, R., Shi, Z., Yang, B., Liu, H., Ding, S., Wang, X., Lei, Q., Wu, J., and Fang, W. (2018). MOF nanoparticles with encapsulated autophagy inhibitor in controlled drug delivery system for antitumor. ACS Appl. Mater. Interfaces *10*, 2328–2337.

63. Jin, M., Zhang, H., Xie, Z., and Xia, Y. (2012). Palladium nanocrystals enclosed by {100} and {111} facets in controlled proportions and their catalytic activities for formic acid oxidation. Energy Environ. Sci. *5*, 6352–6357.

64. Weiswald, L.-B., Bellet, D., and Dangles-Marie, V. (2015). Spherical cancer models in tumor biology. Neoplasia *17*, 1–15.

65. Chen, T., Wei, T., Zhang, Z., Chen, Y., Qiang, J., Wang, F., and Chen, X. (2017). Highly sensitive and selective ESIPT-based fluorescent probes for detection of Pd^{2+} with large Stocks shifts. Dyes Pigm. *140*, 392–398.

66. Clavadetscher, J., Indrigo, E., Chankeshwara, S.V., Lilienkampf, A., and Bradley, M. (2017). In-cell dual drug synthesis by cancer-targeting palladium catalysts. Angew. Chem. Int. Ed. Engl. *56*, 6864–6868.

67. Learte-Aymamí, S., Vidal, C., Gutiérrez-González, A., and Mascareñas, J.L. (2020). Intracellular reactions promoted by bis(histidine) miniproteins stapled using palladium(II) complexes. Angew. Chem. Int. Ed. Published online March 11, 2020.

Supplemental Information

Core-Shell Palladium/MOF Platforms

as Diffusion-Controlled Nanoreactors

in Living Cells and Tissue Models

Raquel Martínez, Carolina Carrillo-Carrión, Paolo Destito, Aitor Alvarez, María Tomás-Gamasa, Beatriz Pelaz, Fernando Lopez, José L. Mascareñas, and Pablo del Pino

Supplemental Experimental Procedures

## Synthesis and characterization of the probes and palladium complexes

General procedures: The compounds propargyl-protected coumarin **1**,[1] propargyl-protected 2-(2'-hydroxyphenyl)benzothiazole **3**,[2] and bis-propargyl carbamate-protected cresyl violet **5**,[3] are known compounds and were synthesized according to those previously reported procedures. Compounds **2, 4** and **6** are commercially available and were purchased from Sigma-Aldrich.

Palladium complexes (**Pd-1** = [Pd(allyl)Cl]$_2$;[4] **Pd-2** = [(PPh$_3$)Pd(allyl)Cl];[5] **Pd-3** = [(PdCl$_2$(TFP)$_2$][6]) have been previously described and were synthesized from the corresponding ligands and palladium precursors following reported procedures. Their ^{1}H, ^{13}C and ^{31}P NMR data were in complete agreement with the reported values. Precursors [Pd(allyl)Cl]$_2$ and [PdCl$_2$(CH$_3$CN)$_2$] are commercially available and were purchased from Sigma-Aldrich and Strem Chemicals, respectively. Ligands triphenylphosphine and tris(2-furyl)phosphine (TFP) were acquired from Sigma-Aldrich.

Reactions were conducted in dry solvents under nitrogen atmosphere using vacuum-line and standard Schlenk techniques unless otherwise stated. Dry solvents were freshly distilled under argon from an appropriate drying agent before use. The removal of solvents under reduced pressure was carried out on a rotary evaporator. Water was deionized and purified on a Millipore Milli-Q Integral system. The abbreviation "r.t." refers to reactions carried out approximately at 23 °C (room temperature). Reaction mixtures were stirred using Teflon-coated magnetic stirring bars. Reaction temperatures were maintained using Thermo watch-controlled silicone oil baths. Thin-layer chromatography (TLC) was performed on silica gel plates (Merck 60 silica gel F$_{254}$) and components were visualized by observation under UV light, and/or by treating the plates with p-anisaldehyde followed by heating. Flash chromatography was carried out in silica gel (Merck Geduran Si 60, 40 – 63 m silica gel, normal phase) unless otherwise stated. Dryings were performed with anhydrous Na$_2$SO$_4$ or MgSO$_4$. Concentration refers to the removal of volatile solvents via distillation using a Büchi rotary evaporator followed by residual solvent removal under high vacuum.

Mass spectra were acquired using IT-MS Bruker AmaZon SL at CiQUS and also using electrospray ionization (ESI) and were recorded at the CACTUS facility of the University of Santiago de Compostela. UV and fluorescence spectra were acquired using Jasco V-670 spectrometer and Varian Cary Eclipse fluorescence spectrofluorometer.

## Synthesis of 4-methyl-7-(prop-2-yn-1-yloxy)-2H-chromen-2-one (1)
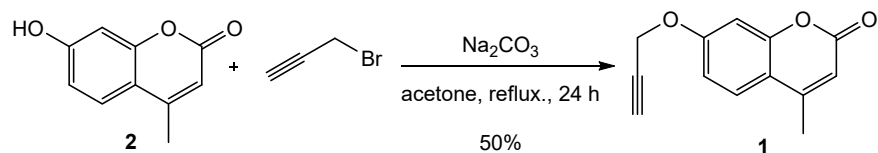
4-Methylumbelliferone (**2**, 0.300 g, 1.702 mmol, 1 eq.) was dissolved in acetone (15 mL) followed by addition of Na$_2$CO$_3$ (0.361 g, 3.411 mmol, 2 eq.). The reaction mixture was stirred at r.t. for 10 min. Further, 3-bromopropyne (0.380 g, 2.552 mmol, 1.5 eq.) was added to the reaction and the resulting mixture was heated at reflux under nitrogen for 24 h. Upon completion, the reaction mixture was cooled to r.t., adsorbed onto silica and purified by silica gel column chromatography EtOAc (20% → 50% v/v)-hexane to give the corresponding product as a white solid. (**1**, 0.182 g, 50%).

## Synthesis of 3-(benzo[d]thiazol-2-yl)-5-methyl-2-(prop-2-yn-1-yloxy)benzaldehyde (3)
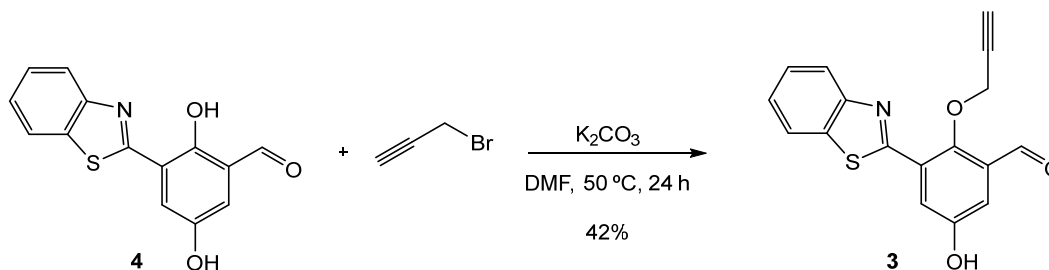
4 (0.250 g, 0.928 mmol, 1 eq.) was dissolved in DMF (5 mL) followed by addition of K$_2$CO$_3$ (0.256 g, 1.864 mmol, 2 eq.). The reaction mixture was stirred at r.t. for 10 min. Further, 3-bromopropyne (0.207 g, 1.392 mmol, 1.5 eq.) was added to the reaction mixture, and heated at 50 °C under nitrogen and stirring for 24 h. Upon completion, the reaction mixture was cooled to r.t., concentrated under vacuum, the crude dissolved in CH$_2$Cl$_2$ (15 mL), adsorbed onto silica, and purified by silica gel column chromatography EtOAc (10% → 30% v/v)-hexane to give the corresponding product as a white solid. (**3**, 0.120 g, 42%).

Synthesis of prop-2-yn-1-yl (Z)-(9-(((prop-2-yn-1-yloxy)carbonyl)amino)-5H-benzo[a]phenoxazin-5-ylidene)carbamate (5)
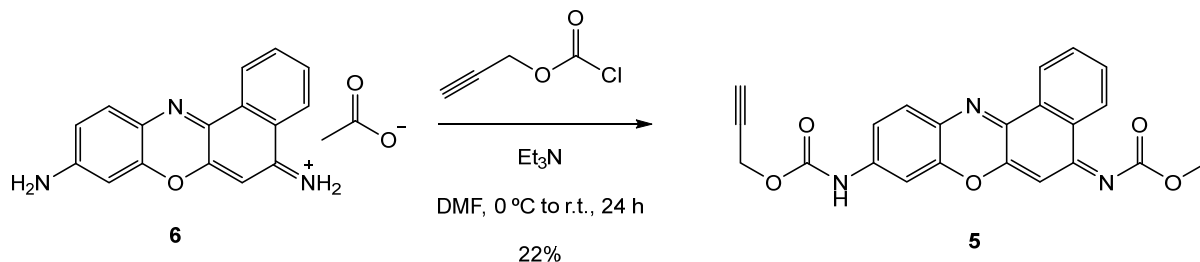
Procedure adapted from Bradley et al.[3] 1H and 13C NMR data of **5** are in agreement with the reported values.[3]

Cresyl violet acetate (0.150 g, 0.467 mmol, 1 eq.) was dissolved in anhydrous DMF (5 mL) and cooled to 0 °C followed by addition of Et$_3$N (0.142 g, 1.403 mmol, 3 eq.). Propargyl chloroformate (5 eq, 2.33 mmol, 0.237 mL in anhydrous DMF (1 mL) was added dropwise to the solution. The reaction mixture was stirred at r.t. for 24 h and followed by RP-HPLC-MS. After that, it was concentrated under vacuum, dissolved in MeOH (15 mL), adsorbed onto silica, and purified by silica gel column chromatography EtOAc (5% → 40% v/v)-hexane to give the corresponding product as a red solid (**5**, 0.044 g, 22%).

Synthesis of [(PPh₃)Pd(allyl)Cl] (Pd-2)
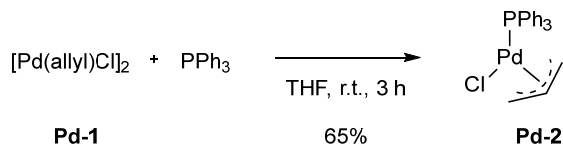
Procedure adapted from Mascareñas et al.[5]

1H, 13C and 31P NMR data of **Pd-2** are in agreement with the reported values.[5]

Triphenylphosphine (0.035 mg, 0.133 mmol, 2 eq.) was dissolved in THF (3.3 mL) followed by addition of [Pd(allyl)Cl]$_2$ (**Pd-1**, 0.024 mg, 0.066 mmol, 1 eq.). The solution was stirred at r.t. under nitrogen for 3 h. After that, it was concentrated under vacuum. The crude was dissolved in AcOEt (ca. 4 mL). Hexane was added (ca. 15 mL) and a pale yellow solid precipitated. After removal of the solvent by decantation, the solid was washed with hexane (3 x 10 mL) and dried under vacuum. The palladium complex (**Pd-2**) was isolated as a pale yellow solid and stored under nitrogen (0.019 g, 65%).

Synthesis of [(PdCl$_2$(TFP)$_2$] (Pd-3)
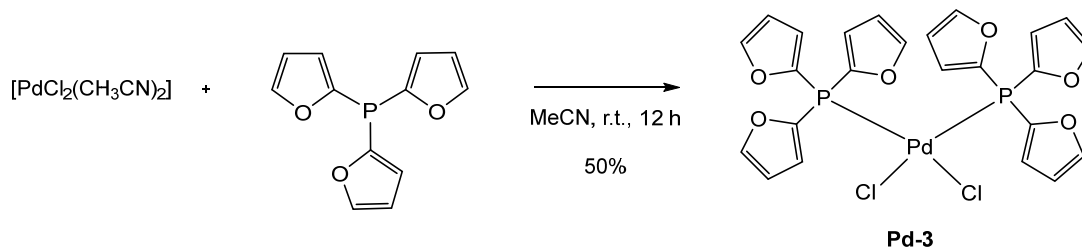
Procedure adapted from Weissleder et al.[6]

^{1}H, ^{13}C and ^{31}P NMR data of **Pd-3** are in agreement with the reported values.[6]

[PdCl$_2$(CH$_3$CN)$_2$] (0.025 mg, 0.098 mmol, 1 eq.) was dissolved in dry MeCN (3.75 mL) followed by addition of a solution of tris(2-furyl)phosphine (TFP) (0.045 mg, 0.196 mmol, 2 eq.) in MeCN (0.5 mL). The reaction mixture was stirred at r.t. overnight and a bright yellow precipitated. The crude product was collected and washed twice with water (2 x 10 mL), dissolved in dried methanol and stored at -30 °C. The palladium complex (**Pd-3**) was isolated as a yellow microcrystalline powder and stored under nitrogen (0.031 mg, 50%).

UV and Fluorescence spectra:

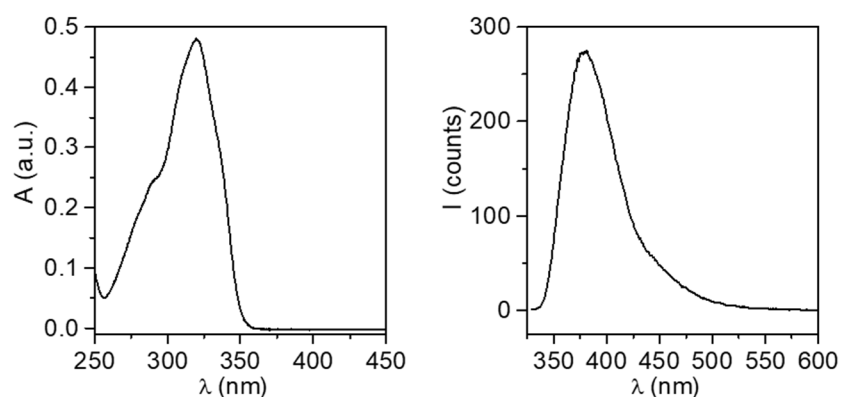## 4-methyl-7-(prop-2-yn-1-yloxy)-2H-chromen-2-one (1)

Figure S1. UV spectra (left) of **1** (30 µM, 1:1 v/v mixture of DMSO:Tris buffer 200 mM, pH = 7.5) and fluorescence spectra (10 µM, 7:3 v/v mixture of DMSO:H_2O) λ_{ex} 323 nm, λ_{em} 380 nm, λ_{cut} 330 nm (right).

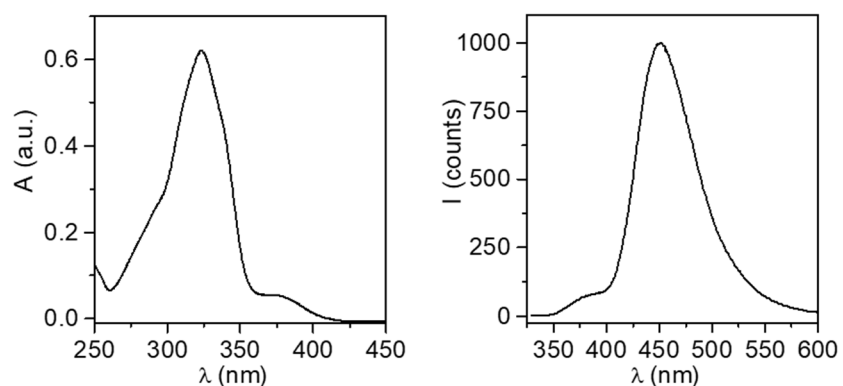## 7-hydroxy-4-methyl-2H-chromen-2-one (2)

Figure S2. UV spectra (left) of **2** (30 µM, 1:1 v/v mixture of DMSO:Tris buffer 200 mM, pH = 7.5) and fluorescence spectra (10 µM, 7:3 v/v mixture of DMSO:H_2O) λ_{ex} 323 nm, λ_{em} 452 nm, λ_{cut} 330 nm (right).
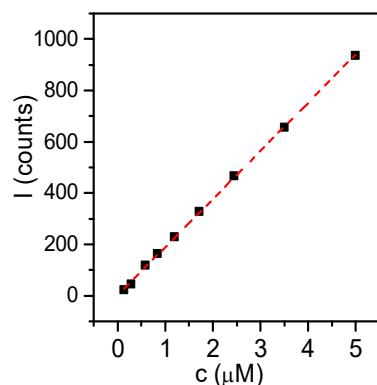

Figure S3. Calibration curve of **2** (9:1 v/v H_2O:MeOH), λ_{ex} 323 nm, λ_{em} 452 nm. Dashed red line: linear regression fitting I (counts) = 1+188·c(µM); coefficient of determination R^2 = 0.999.

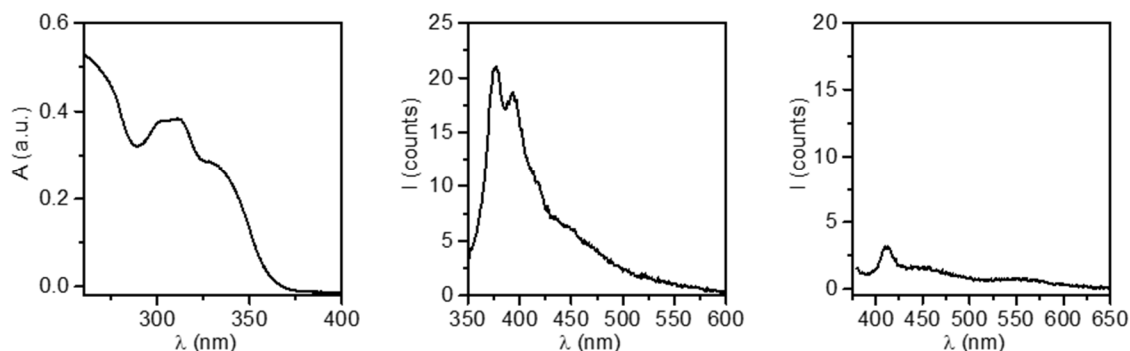### 3-(benzo[d]thiazol-2-yl)-5-methyl-2-(prop-2-yn-1-yloxy)benzaldehyde (3)

Figure S4. UV spectra (left) of **3** (20 µM, 7:3 v/v DMSO:H_2O) and fluorescence spectra (5 µM, 7:3 v/v DMSO:H_2O) λ_{ex} 335 nm, λ_{em} 377 nm, λ_{cut} 340 nm (middle), λ_{ex} 368 nm, λ_{em} 412 nm, λ_{cut} 380 nm (right).

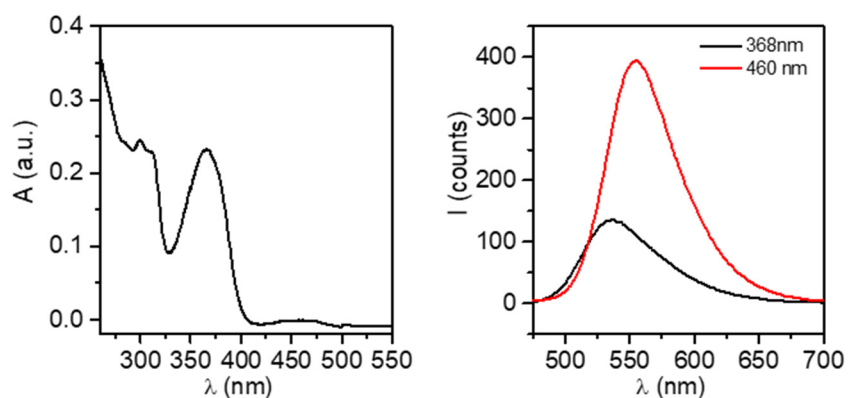### 3-(benzo[d]thiazol-2-yl)-2-hydroxy-5-methylbenzaldehyde (4)

Figure S5. UV spectra (left) of **4** (20 µM, DMSO:H_2O 7:3), and fluorescence spectra (5 µM, 7:3 v/v mixture of DMSO:H_2O) at different wavelengths (λ_{ex} 368 nm, λ_{em} 558 nm, λ_{cut} 380 nm and λ_{ex} 460 nm, λ_{em} 535 nm, λ_{cut} 465 nm (right).
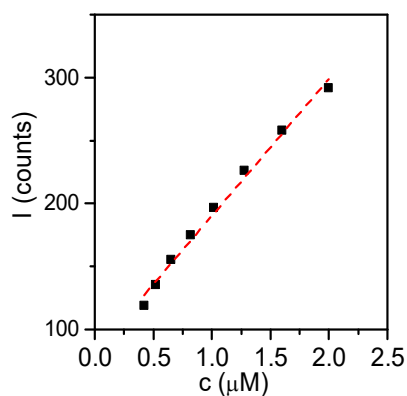
Figure S6. Calibration curve of **4** (7:3 v/v DMSO:H_2O), λ_{ex} 460 nm, λ_{em} 535 nm, λ_{cut} 470 nm. Dashed red line: linear regression fitting I (counts) = 81 + 108·c(µM); coefficient of determination R^2 = 0.990.

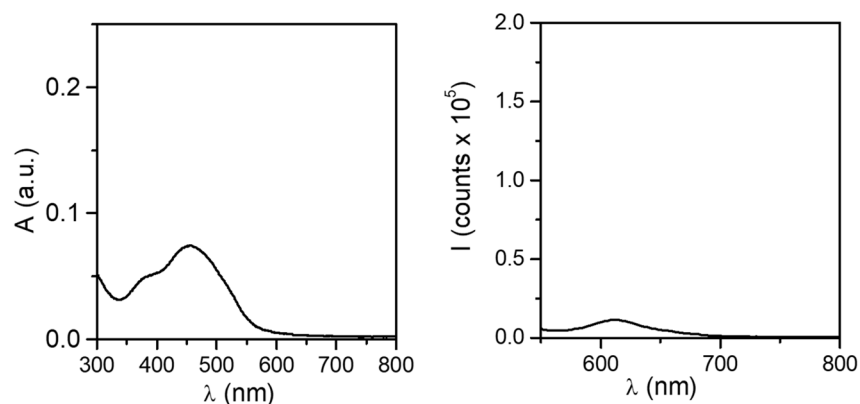prop-2-yn-1-yl(Z)-(9-(((prop-2-yn-1-yloxy)carbonyl)amino)-5H-benzo[a]phenoxazin-5-ylidene)carbamate (5)

Figure S7. UV spectra (left) of **5** (10 µM, 8:2 PBS:MeOH), and fluorescence spectra (1 µM, 8:2 PBS:MeOH) under excitation at λ_{ex}=540 nm; maximum emission at λ_{em}=610 nm (right).

9-Amino-5-imino-5H-benzo[a]phenoxazine (6)
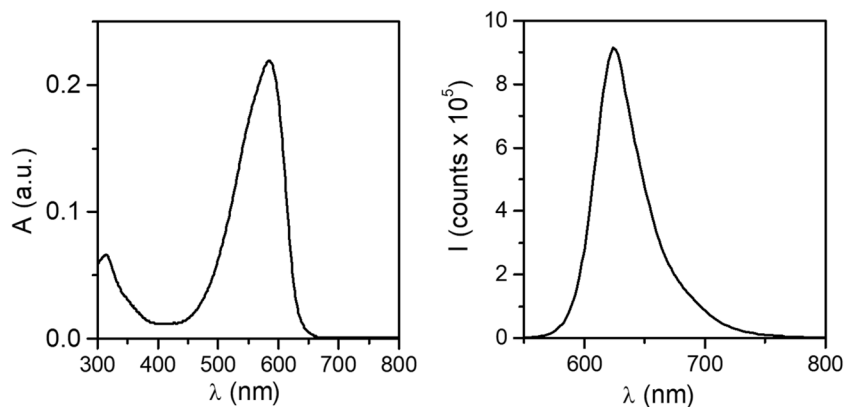
Figure S8. UV spectra (left) of **6** (10 µM, 8:2 PBS:MeOH), and fluorescence spectra (1 µM, 8:2 PBS:MeOH) under excitation at λ_{ex}=540 nm; maximum emission at λ_{em}=624 nm (right).
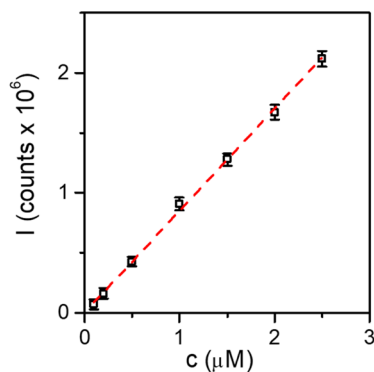

Figure S9. Calibration curve of **6** (8:2 PBS:MeOH), λ_{ex}=540 nm, λ_{em}=624 nm. Dashed red line: linear regression fitting I·10^5 (counts) = 0.006 + 8.504·c(µM); coefficient of determination R^2 = 0.998.

Synthesis of PMA-modified Pd/ZIF-8 nanocomposites (NRs)

Chemicals: All the reagents including potassium tetrachloropalladium (II) (K_2PdCl_4; Sigma Aldrich #205796), L-ascorbic acid (AA; Sigma Aldrich #A5960), zinc nitrate hexahydrate ($Zn(NO_3)_2 \cdot 6H_2O$; Sigma Aldrich #96482), 2-methylimidazole (MeIm; Sigma Aldrich #M50850), and hexadecyltrimethylammonium bromide (CTAB; Sigma Aldrich #H5882) were used as purchased without any purification. The PMA-based amphiphilic polymer (i.e., poly[isobutylene–alt–maleic anhydride]–graft–dodecyl) was synthesized as described previously.[7]

Synthesis of Pd nanocubes: CTAB-coated Pd nanocubes enclosed by {100} facets were synthesized according to a previously reported protocol,[8] using K_2PdCl_4 as precursor, L-ascorbic acid (AA) as reducing agent, and hexadecyltrimethylammonium bromide as capping agent and stabilizer. In a typical synthesis, 0.5 mL of 0.1 M CTAB, 21.25 mL of deionized water and 2.5 mL of 0.01 M K_2PdCl_4 were placed in a 50 mL glass vial, and then 0.75 mL of 0.1 M AA was added while magnetic stirring. The mixture is stirred at room temperature for some minutes (~5 min) observing during this time that the solution turns into black color, which indicates the formation of the Pd nanocubes (in the following referred to as Pd-NPs). Next, the black product was collected by centrifugation (7200 RCF, 10 min), washed twice with MilliQ water to remove the excess of CTAB (Figure S10), and finally the purified Pd-NPs were redispersed in 1.4×10^{-3} M CTAB.

Synthesis of Pd/ZIF-8: These particles were synthesized according to a previously reported protocol with slight modifications.[9] The Pd-NPs were used as seeds onto which a shell of ZIF-8 was grown, in the presence of CTAB as size-controlling and structural-directing agent, obtaining in this way the core-shell nanocomposite. Briefly, an aqueous solution of zinc nitrate (1 mL, 0.025 M) was added to an aqueous solution of 2-methylimidazole (1 mL, 1.3 M) under magnetic stirring (350 rpm) at r.t., and immediately after, a solution containing the Pd-NPs (1mL, 2 nM of nanoparticles dispersed in 1.4×10^{-3} M of CTAB) was added. After 2 min, the stirring was stopped, and the mixture was left undisturbed for 3 h at r.t. The gradual appearance of brownish turbidity indicated the formation of the Pd/ZIF-8 particles. Finally, the particles were collected by centrifugation (7000 RCF, 5 min), washed twice with methanol (MeOH) and redispersed in 1 mL of MeOH. The concentration of particles in this solution was assumed to be ~2 nM, considering that one Pd/ZIF-8 particle was formed per Pd-NP (seed). Note that under optimized conditions virtually all the ZIF-8 particles contained a Pd-NP as core (Figure S11).

Post-functionalization of Pd/ZIF-8 with PMA polymer: The as-prepared Pd/ZIF-8 particles were functionalized with a PMA-based amphiphilic polymer (i.e., poly[isobutylene–alt–maleic anhydride]–graft–dodecyl) by following a recently described protocol.[9] Briefly, the Pd/ZIF-8 particles dispersed in methanol were mixed with the solution of the polymer in chloroform in an optimized proportion; specifically, 150 monomers of polymer per nm^2 of Pd/ZIF-8 particle, assuming a spherical particle with diameter of 250 nm; and the mixture was placed in a rotary evaporator. After complete evaporation of the solvent (3:1 MeOH:CHCl$_3$) the dried product was resuspended by addition of sodium borate buffer (0.1 M, pH 9) and aided by sonication (1-2 min). The resulting PMA-modified Pd/ZIF-8 nanocomposites (in the following referred to as NRs) were collected and purified by centrifugation (7000 RCF, 10 min), washing twice with water, and finally redispersed in water.

Morphological/structural characterization of NRs

Scanning Electron Microscopy (SEM): The size and morphology of Pd-NPs and NRs were investigated with SEM (Figures S10 and S11). SEM images were acquired with a FESEM Zeiss Ultra Plus operated at 3 kV or 20 kV.
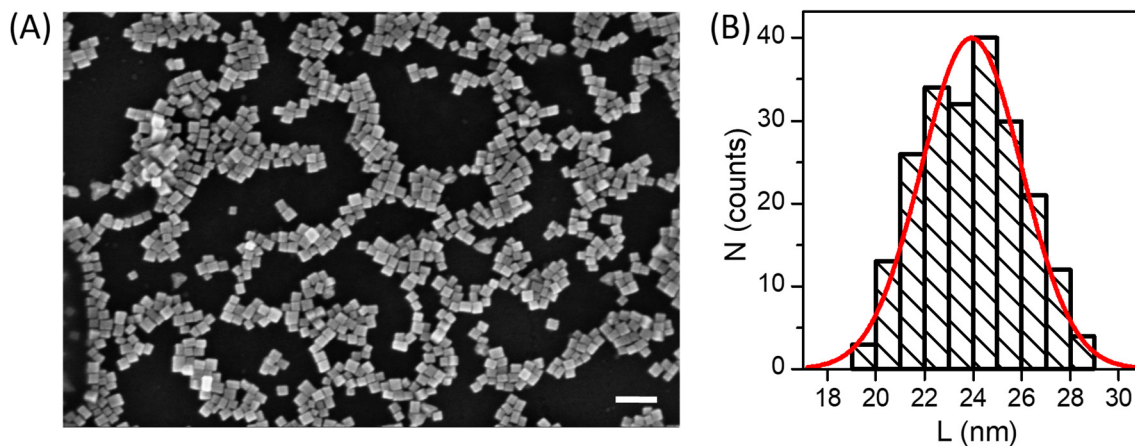
Figure S10. (A) Representative SEM image (scale bar corresponds to 100 nm); and (B) the corresponding histogram of the number distribution N of the side length L of the Pd-NPs (200 particles measured) as determined from SEM images, L = (23.9 ± 2.0) nm.
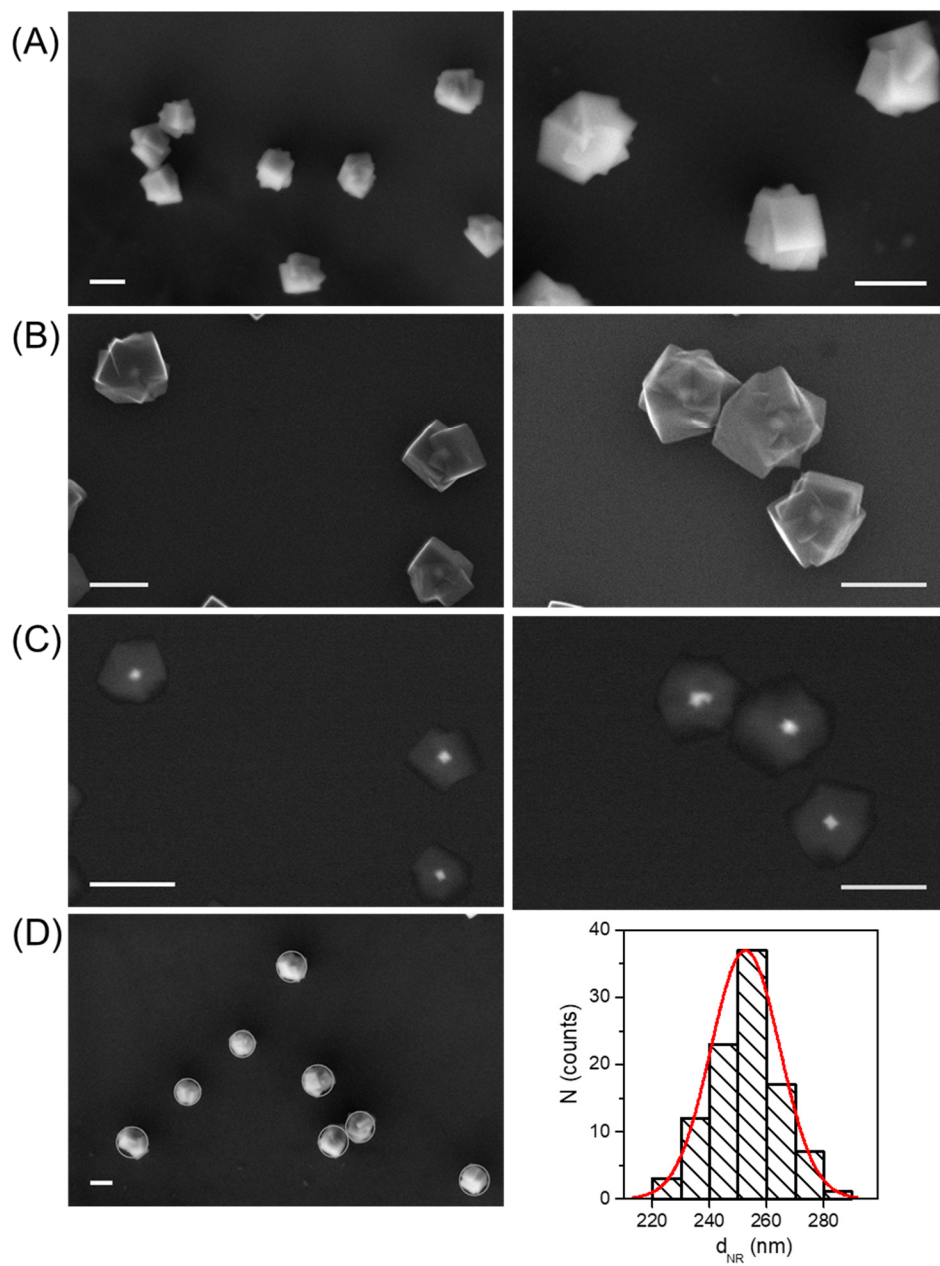
Figure S11. Representative SEM images of the NRs acquired with different detectors and different voltages: (A) Everhart-Thornley detector (SE2, secondary electrons) at 3 kV, (B) InLens detector (SE1, secondary electrons) at 20 kV, and (C) AsB detector (backscattered electrons) at 20 kV. Scale bars correspond to 200 nm. (D) Histogram of the number distribution N of the diameter (i.e., vertex-to-vertex distance) d_{NR} of the NRs (idealized as spherical particles; 100 particles measured); regions of interest (ROIs, outlines) were drawn in the SEM images to estimate the size of the NRs, i.e., $d_{NR} = (253 \pm 12)$ nm.

Powder x-ray diffraction (PXRD): An x-ray diffractometer Philips was used to study the crystallinity of the Pd/ZIF-8 nanocomposites. Sample was examined in the range of 2θ between 2° and 75° with a passage of 0.02° and a time by step of 2s. Table S1 show the major diffraction peaks identified by PXRD (cf., Figure S12).
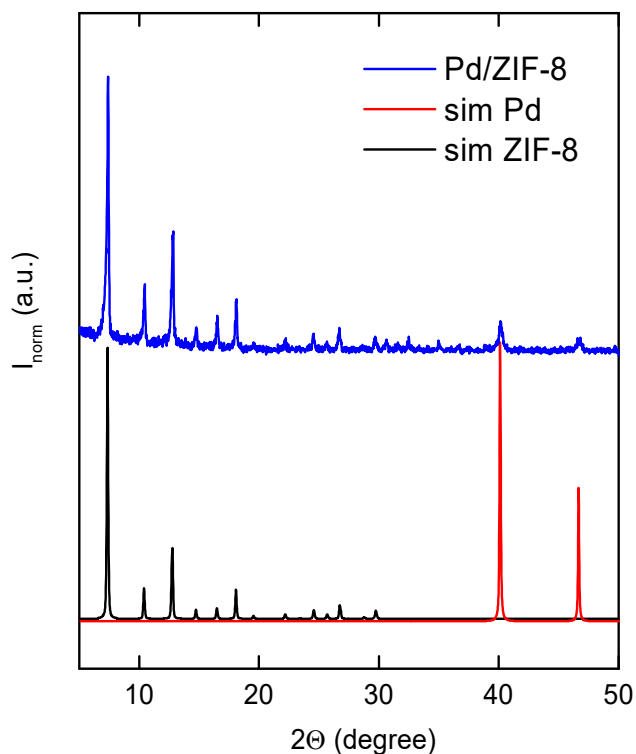
Figure S12. PXRD spectrum of Pd/ZIF-8 nanocomposites. For comparison, simulations of ZIF-8 (black, COD - Crystallography Open Database: 7111970) and Pd-fcc (red; COD: 9008478) are added. I_{norm} is the normalized intensity.

Table S1: Major peaks (relative intensity > 6%) identified in the Pd/ZIF-8 diffractogram.

Pos. (°2θ)	Height (cts)	FWHM Left (°2θ)	d-spacing (Å)	Rel. Int. (%)
7.37	447	0.16	11.977	100.0
10.44	95	0.16	8.470	21.2
12.79	209	0.15	6.918	46.6
14.75	33	0.16	5.999	7.5
16.52	49	0.17	5.363	11.0
18.09	93	0.15	4.899	20.7
24.52	30	0.16	3.627	6.6
26.68	33	0.22	3.339	7.4
40.13	46	0.34	2.245	10.3

Dynamic light scattering (DLS) and Zeta-Potential (ζ): The hydrodynamic diameter (d_h) and polydispersity index (PDI) of the nanocomposites were determined by DLS using a Malvern Zetasizer Nano ZSP equipped with a 10 mW He–Ne laser operating at a wavelength of 633 nm and fixed scattering angle of 173°. DLS spectra of the NRs dispersed in water freshly prepared, as well as measured over time up to one week are presented in Figure S13, and the corresponding d_h values of the NRs both in water, cell medium (supplemented with 10% fetal bovine serum - FBS) and artificial lysosomal fluid (ALF, 10% FBS or without supplements) over time, are summarized in Table S2.
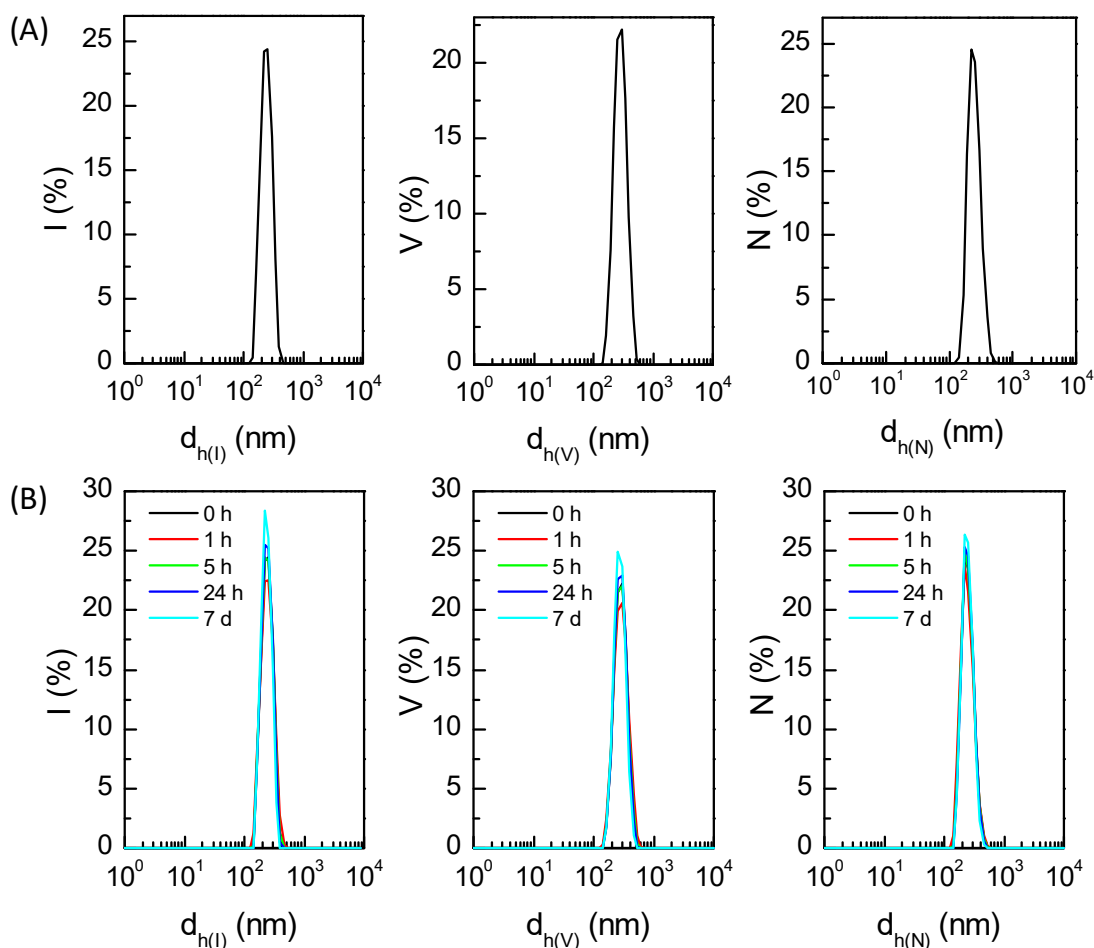

Figure S13. DLS spectra, given as intensity, volume and number distributions, of NRs dispersed in water (A) freshly prepared, and (B) measured at different time points up to one week.

Table S2. Hydrodynamic diameters d_h (mean value ± SD) as derived from DLS measurements of the NRs and Pd-NPs dispersed in water, cell culture medium (DMEM supplemented with 10 % FBS), artificial lysosomal fluid (ALF), or ALF supplemented with 10 % FBS at different time points. SD values correspond to the standard deviation of the diameter mean value as obtained from several repetitions (n=3) of the measurement. The polydispersity index (PDI) values are also given.

NRs								
Time	water		cell medium		ALF		ALF (10% FBS)	
	$d_{h(N)}$ (nm)	PDI	$d_{h(N)}$ (nm)	PDI	$d_{h(N)}$ (nm)	PDI	$d_{h(N)}$ (nm)	PDI
0 h	252 ± 2	0.18	299 ± 8	0.22	268 ± 3	0.14	289 ± 6	0.12
1 h	249 ± 3	0.21	291 ± 9	0.24	273 ± 4	0.15	300 ± 7	0.21
5 h	251 ± 2	0.22	289 ± 11	0.24	278 ± 4	0.20	295 ± 7	0.20
24 h	252 ± 2	0.20	294 ± 10	0.30	292 ± 2	0.11	293 ± 9	0.19
7 days	250 ± 4	0.22	301 ± 10	0.35	296 ± 3	0.19	294 ± 8	0.22
Pd-NP								
Time	water		cell medium		ALF*		ALF (10% FBS)	
	$d_{h(N)}$ (nm)	PDI	$d_{h(N)}$ (nm)	PDI	$d_{h(N)}$ (nm)	PDI	$d_{h(N)}$ (nm)	PDI
0 h	25 ± 1	0.16	50 ± 3	0.19	376 ± 15	0.23	58 ± 2	0.15
1 h	68 ± 2	0.20	53 ± 3	0.20	-		61 ± 3	0.21
5 h	113 ± 3	0.24	51 ± 3	0.20	-		61 ± 4	0.20
24 h	171 ± 10	0.27	49 ± 4	0.21	-		56 ± 3	0.19
48 h	362 ± 24	0.39	50 ± 3	0.22	-		54 ± 3	0.19
7 days	480 ± 25	0.41	49 ± 4	0.19	-		53 ± 4	0.20

*Pd-NPs aggregated immediately in ALF, leading to irreversible precipitation.

Quantification of Pd by inductively coupled plasma mass spectrometry (ICP-MS) and estimation of potentially active Pd

Quantification of Pd by ICP-MS: ICP-MS measurements were performed on an Agilent 7700x inductively coupled plasma mass spectrometer after acidic digestion of the particles sample with aqua regia. To this end 300 µL of fresh aqua regia (i.e. HCl 35 wt % and HNO_3 67 wt % in 3:1 volume ratio) was added to 50 L of sample solution (solutions of NRs or Pd nanoparticles as control; both at the same concentration), and then the samples were left for digestion overnight. Afterwards 4.65 mL of HCl solution (2 wt % HCl) was added prior to their injection into ICP-MS, being thus the total dilution sample of 100. External calibration was applied to quantify the amount of elemental Pd and Zn. External standards were prepared by diluting ICP-MS standards of all the ions in the same background solution (2 wt % HCl) as the samples, measured by triplicate and used for obtaining the external calibration curves.

Results revealed that the total amount of Pd atoms used per reaction were: 8.9 µg (RSD = 1.0 %) for NRs and 9.1 µg (RSD = 1.4 %) for Pd-NPs (Table S3). This clearly indicates that when we are carrying out equivalent reactions with NRs and Pd-NPs (for comparison), we are using the same amount of Pd.

The amount of Pd per NR was determined from ICP-MS data; and considering that the empirical formula of ZIF-8 is $C_8H_{10}N_4Zn$, which means that 1 mol of ZIF-8 contains 1 mol of Zn. Therefore, the Pd amount in NR (i.e. Pd/ZIF-8) could be determined by the following equation:

$$\% \, Pd = \frac{m_{Pd}}{m_{Pd} + m_{Zn}\frac{M_{ZIF-8}}{M_{Zn}}} * 100$$

where,
m_{Pd} = Amount of ^{105}Pd obtained by ICP-MS
m_{Zn} = Amount of ^{66}Zn obtained by ICP-MS
M_{Zn} = Atomic mass of Zn (65.38 g/mol)
M_{ZIF-8} = Molecular mass of ZIF-8 (227.58 g/mol)

Applying this equation, we obtained that the percentage of total Pd in the NR is 3.8 wt%. It was also determined by ICP-MS that this wt% of Pd in the NR is the same after performing the reaction, which is a clear indication of the stability of the NRs during the catalytic reaction.

Table S3 Amount of Pd per reaction as derived from ICP-MS measurements.

Catalyst	V_{cat} (µL)	$C_{particles}$ (nM)	V_{react} (µL)	c_{Zn} (µg/µL)*	c_{Pd} (µg/µL)*	m_{Zn} (µg)	$m_{Pd,total}$ (µg)	Pd total (wt %)
Pd-NPs	50	2	400	–	0.183	–	9.1	100
NRs	50	2	400	1.296	0.179	64.8	8.9	3.8

*Relative standard deviation (RSD) < 1.5%

Estimation of the Pd potentially active for catalysis: Whereas ICP-MS measurements give us the total amount of Pd contained in the NR, it is important to note that only the Pd atoms on the surface of the Pd-NP (located in the center of the NR) will be able to catalyze the reactions and therefore, only this fraction of Pd (hereinafter referred to as surface-Pd) is potentially active. We can estimate this surface-Pd as follows (cf., Table S4).

1) First, we calculate the number of Pd atoms contained in a Pd-NP:

The volume of a Pd-NP (V_{NP}) with a side length of 23.9 nm as determined from SEM images:

$V_{NP} = L^3 = (23.9 \text{ nm})^3 = 1.36 \times 10^4 \text{ nm}^3$

The structure is face-centered-cubic (fcc structure) with a lattice constant of 0.389 nm, being the volume of a unit cell ($V_{fcc\ cell}$)

$V_{fcc\ cell} = (0.389 \text{ nm})^3 = 0.059 \text{ nm}^3$

Knowing that each unit cell contains 4 Pd atoms, the total number of Pd atoms in a single Pd-NP is:

$N_{Pd,\ cell} = (1.56 \times 10^4 \text{ nm}^3) / (0.059 \text{ nm}^3) \times 4 = 9.26 \times 10^5$

2) Next, we calculate the number of Pd atoms on the surface of a Pd-NP:

A Pd-NP is enclosed by 6 {100} facets, so the total surface area of a Pd-NP ($A_{nanocube}$) can be calculated as:

$A_{nanocube} = 6 \times L^2 = 6 \times (23.9 \text{ nm})^2 = 3.43 \times 10^3 \text{ nm}^2$

The lattice constant of the fcc unit cell is 0.389 nm, and each two-dimensional unit cell on the {100} facets contains two Pd atoms. Therefore, the total number of Pd atoms on the surface of a single nanocube ($N_{Pd,\ surface}$) can be calculated as:

$A_{fcc\ cell} = (0.389 \text{ nm})^2 = 0.151 \text{ nm}^2$

$N_{Pd,\ surface} = (3.43 \times 10^3 \text{ nm}^2) / (0.151 \text{ nm}^2) \times 2 = 4.54 \times 10^4$

3) Knowing the number of NRs used for the catalytic reaction we calculate the amount of surface-Pd per reaction:

The total amount of Pd used per reaction is 8.94×10^{-6} g as determined by ICP-MS. Thus, the total number of Pd atoms in the catalytic reaction is:

$N_{Pd} = (8.94 \times 10^{-6} \text{ g}) / (106.42 \text{ g/mol}) \times (6.02 \times 10^{23} \text{ mol}^{-1}) = 5.06 \times 10^{16}$

The number of Pd-NPs involved in the catalytic reaction is (note that one nanocube contains 9.26×10^5 Pd atoms as calculated above):

$N_{nanocube} = (5.06 \times 10^{16}) / (9.26 \times 10^5) = 5.46 \times 10^{10}$

Note here that owing to the architecture of the nanocomposite particle (one Pd-NP in the center of one NR), the number of NRs involved in the reaction is the same as the number of Pd-NPs.

Thus, the **actual concentration of NRs** used per reaction (total volume 400 µL) is:

$n_{NR} = (5.46 \times 10^{10}) / (6.022 \times 10^{23}) = 9.07 \times 10^{-14}$ mol of NR

$C_{NR} = (9.07 \times 10^{-14}) / (4 \times 10^{-4}) = 2.3 \times 10^{-10}$ M = **0.23 nM**

Regarding the fraction of Pd potentially active, the total number of Pd atoms on the surface of Pd-NPs used in the catalytic reaction is:

$N_{\text{total surface-Pd}} = (4.77 \times 10^{10}) \times (4.96 \times 10^4) = 2.71 \times 10^{15}$

$n_{\text{total surface-Pd}} = (2.71 \times 10^{15}) / (6.022 \times 10^{23}) = 4.5 \times 10^{-9}$ mol of surface-Pd

As the total volume of the reaction is 400 µL, the **concentration of surface Pd in the reaction** is ~**10 µM**.

Table S4. Amounts of Pd (total and surface) per reaction as derived from ICP-MS measurements.

Catalyst	V_{NP} (nm³)	$V_{\text{fcc,cell}}$ (nm³)	$N_{\text{Pd,cell}}$*	A_{NP} (nm²)	$A_{\text{fcc,cell}}$ (nm²)	$N_{\text{Pd,surface}}$#	$m_{\text{Pd,total}}$ (µg)	$m_{\text{Surface-Pd}}$ (µg)	$C_{\text{Surface-Pd}}$ (µM)
Pd NPs	$1.36 \cdot 10^4$	0.059	$9.26 \cdot 10^5$	$3.43 \cdot 10^3$	0.151	$4.54 \cdot 10^4$	9.14	$3.78 \cdot 10^{-5}$	10.1
NRs	$1.36 \cdot 10^4$	0.059	$9.26 \cdot 10^5$	$3.43 \cdot 10^3$	0.151	$4.54 \cdot 10^4$	8.94	$3.69 \cdot 10^{-5}$	9.8

*Each unit cell with fcc structure contains 4 Pd atoms

#Each two-dimensional unit cell on the {100} facets contains 2 Pd atoms

Evaluation of porous accessibility/porosity of NRs

The porosity and possibility of diffusion-controlled flow of molecules through the porous of the ZIF-8 shell in the NRs was evaluated using model fluorescent probes. To this end, NRs were incubated with two fluorescent probes: TAMRA (tetramethylrhodamine 5-(and-6)-carboxamide cadaverine) and DOX (doxorubicin); and the amount loaded probes was quantified by fluorescence. NRs as dispersed in water (100 µL, 1 nM) were mixed with a solution of fluorescent probes in MeOH (10 µL, 1.5 mM), having thus 1.5×10^5 probe/NC during the incubation, and the mixture was incubated for 4 h at r.t. Afterwards, the NRs were quickly collected by centrifugation (1 min, 10,000 RCF), and the loaded fluorescent molecules were determined after digestion/destruction of the NRs in order to avoid errors in the quantification associated to potential fluorescence quenching and/or scattering/turbidity interference. For the digestion, the pellet of NR containing the fluorescent molecules were treated with 40 µL of 2% HCl solution for 15 min. Then, 10 µL of 2 M NaOH solution was added to neutralize the medium, plus 250 µL of water, and fluorescence measurement of this mixture was performed. The concentration of TAMRA or DOX loaded was determined by interpolation of the measured fluorescence intensity (I) to a previously constructed analytical calibration curve (Figure S14). This led to a value (mean ± standard deviation, n=2) of $4.24 \times 10^4 \pm 8.29 \times 10^2$ TAMRA per NR and $7.58 \times 10^4 \pm 6.25 \times 10^2$ DOXO per NR (Table S5).
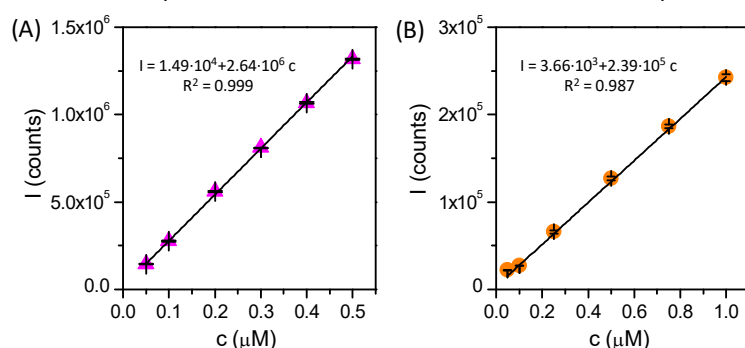

Figure S14. Calibration curves of TAMRA (A) and DOX (B) in water obtained from fluorescence measurements: for TAMRA $\lambda_{exc}/\lambda_{em}$=550/580 nm and for DOXO $\lambda_{exc}/\lambda_{em}$=480/588 nm. Fluorescence intensity (I) at the maximum emission peak as a function of HOE concentration c is plotted and calibration equation is obtained by fitting a linear regression line to the collected data; R^2 is the coefficient of determination.

Table S5. Determination of loading percentage of two fluorescent probes into the NRs after 4 h of incubation.

probe	$N_{probe/NR}$ (incubated)	$N_{probe/NR}$ (loaded)	% loading
TAMRA	$1.5 \cdot 10^5$	$4.24 \cdot 10^4 \pm 8.29 \cdot 10^2$	28.3 ± 0.8
DOX	$1.5 \cdot 10^5$	$7.58 \cdot 10^4 \pm 6.25 \cdot 10^2$	50.5 ± 0.6

General procedures of the depropargylation reactions

Depropargylation of substrates 1 and 3 promoted by NR or Pd-NPs: **1** or **3** (8 μL, 0.5 mM stock solution in MeOH) was added to a H_2O:MeOH 9:1 solution (342 μL) in a 1.5 mL HPLC vial (containing a stirring bar) followed by addition of an aqueous solution of Pd-NPs or NRs (50 μL, 2 nM; this corresponds to 10 μM of surface-Pd). The influence of the catalyst concentration was also evaluated by varying the amount of the aqueous solution of Pd-NPs or NRs added. The vial was sealed with a screw cap and the reaction mixture was stirred (400 rpm) at 37 °C. After overnight (15 h), NRs were collected by centrifugation (7000 RCF, 10 min), and the supernatant was separated. The precipitate was washed once with 400 μL of a 9:1 H_2O:MeOH solution, centrifuged again (7000 RCF, 10 min), and the supernatant was separated and mixed with the first supernatant. Finally, this supernatant was analyzed by fluorescence to quantify the obtained amount of **2** or **4** respectively (Table S6, Figure S15), cf. calibration curves in Figure S3.

Depropargylation of substrate 5 promoted by NR: **5** (8 μL, 0.5 mM stock solution in MeOH) was added to a PBS:MeOH 8:2 solution (342 μL) in a 1.5 mL HPLC vial (containing a stirring bar) followed by addition of an aqueous solution of NRs (50 μL, 2 nM; this is the concentration of NRs). The vial was sealed with a screw cap and the reaction mixture was stirred (400 rpm) at 37 °C. After overnight (15 h), the NRs were collected by centrifugation (7000 RCF, 10 min), and the supernatant was separated. The precipitate was washed once with 400 μL of a 8:2 PBS:MeOH solution, centrifuged again (7000 RCF, 10 min), and the supernatant was separated and mixed with the first supernatant. Finally, this supernatant was analyzed by fluorescence to quantify the amount of **6** obtained (Table S6, Figure S15), cf. calibration curve in Figure S6.

Depropargylation of substrate 1 in the presence of 3 promoted by NR: **1** (8 μL, 0.5 mM stock solution in MeOH) and **3** (8 μL, 0.5 mM stock solution in MeOH) were added to a H_2O:MeOH 9:1 solution (334 μL) in a 1.5 mL HPLC vial (containing a stirring bar) followed by addition of an aqueous solution of NRs (50 μL, 2 nM; this is the concentration of NRs). The vial was sealed with a screw cap and the reaction mixture was stirred (400 rpm) at 37 °C. After overnight (15 h), the NRs were collected by centrifugation (7000 RCF, 10 min), and the supernatant was separated. The precipitate was washed once with 400 μL of a 9:1 H_2O:MeOH solution, centrifuged again (7000 RCF, 10 min), and the supernatant was separated and joined with the first supernatant. Finally, this supernatant was analyzed by fluorescence to quantify the obtained amount of **2** and **4** (Table S6), cf. calibration curve in Figure S9.

Table S6 Reaction conditions and yields of the depropargylation of several substrates promoted by NRs or Pd-NPs; as control, we also used ZIF-8 nanoparticles without the Pd core.

Catalyst type	Surface Pd (µM)	Conditions	Substrate	[Substrate] (µM)	Product	[Product] (µM)	Yield (%)
NRs	1	H_2O:MeOH 9:1, 37 °C, 15h	1	10	2	3.70 ± 0.08	37.0 ± 1.2
NRs	5	H_2O:MeOH 9:1, 37 °C, 15h	1	10	2	8.92 ± 0.14	89.2 ± 1.4
NRs	10	H_2O:MeOH 9:1, 37 °C, 15h	1	10	2	9.70 ± 0.13	97.0 ± 1.3
NRs	15	H_2O:MeOH 9:1, 37 °C, 15h	1	10	2	9.85 ± 0.15	98.5 ± 1.5
NRs	10	PBS:MeOH 9:1, 37 °C, 15h	1	10	2	9.20 ± 0.14	92.0 ± 1.4
Pd-NPs	10	H_2O:MeOH 9:1, 37 °C, 15h	1	10	2	1.90 ± 0.45	19.0 ± 4.5
ZIF-8[#]	0	H_2O:MeOH 9:1, 37 °C, 15h	1	0	n.r.*	n.r.*	n.r.*
NRs	10	H_2O:MeOH 9:1, 37 °C, 15h	3	10	n.r.*	n.r.*	n.r.*
Pd-NPs	10	H_2O:MeOH 9:1, 37 °C, 15h	3	10	4	1.54 ± 0.18	15.4 ± 1.8
NRs	10	H_2O:MeOH 9:1, 37 °C, 15h	1+3	10+10	2	5.40 ± 0.37	54.0 ± 3.7
NRs	10	PBS:MeOH 8:2, 37 °C, 15h	5	10	6	8.23 ± 0.10	82.3 ± 1.0

*n.r. : no reaction; [#]ZIF-8 nanoparticles equivalent to NRs, but without the Pd core.
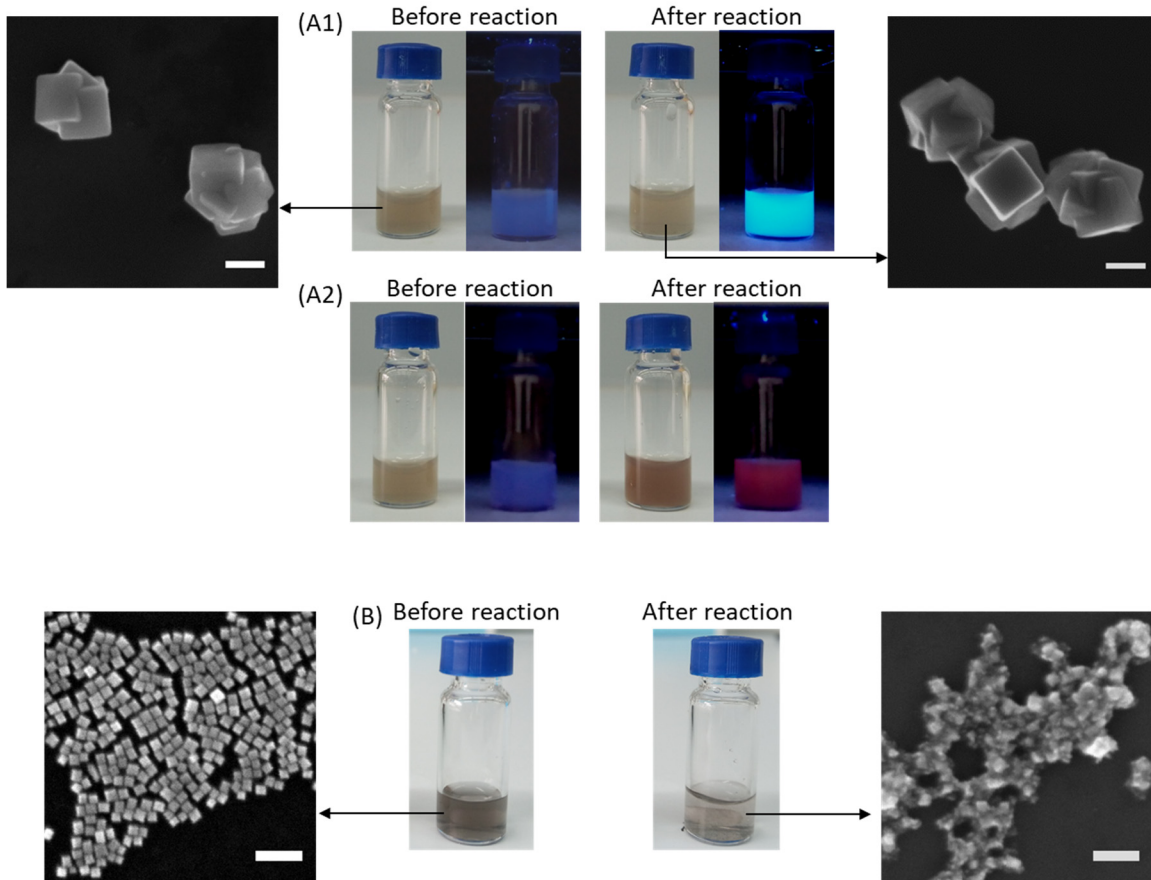
Figure S15. (A) Photographs under visible and UV light of the reaction mixture for the depropargylation reaction of **1** (A1) or **5** (A2) promoted by NRs taken before and after the reaction. (B) Photographs under visible light of the reaction mixture for the depropargylation reaction of **1** promoted by Pd NPs taken before and after the reaction, where aggregation of Pd-NPs is observed. Scale bars correspond to 100 nm.

Calculation of turnover number (TON): As it was calculated in a previous section, the concentration of the catalyst (surface-Pd) used in the reaction under the optimized conditions was 10 µM. Knowing that the total volume of the reaction is 400 µL, this corresponds to 4×10^{-9} mol of catalyst per reaction. The calculation of the yield of the reactions, and therefore, the amount of substrate converted to the desired product, allows us to calculate the TON by using the following equation:

$$TON = \frac{\text{moles of desired product formed}}{\text{moles of catalyst}}$$

We determined the TON values as function of the amount of catalyst used and maintaining constant the amount of substrate (see Table S7).

Table S7. TON values of the reaction for the depropargylation reaction of **1** and **5** by using different amounts of NRs. In all cases the reactions were carried out overnight at 37 °C, except in one case where the reaction was performed for 7 days.

[Catalyst] (μM surface Pd)	Substrate	[Substrate] (μM)	Conditions	Yield (%)	[Product] (μM)	TON
15	1	10	37 °C, 15 h	98.5 ± 1.5	9.85 ± 0.15	0.66 ± 0.01
10	1	10	37 °C, 15 h	97.0 ± 1.3	9.70 ± 0.13	0.97 ± 0.01
5	1	10	37 °C, 15 h	89.2 ± 1.4	8.92 ± 0.14	1.78 ± 0.04
1	1	10	37 °C, 15 h	37.0 ± 1.2	3.70 ± 0.08	3.70 ± 0.11
1	1	10	37 °C, 7 d	99.6 ± 1.1	9.96 ± 0.11	9.96 ± 0.15
15	5	10	37 °C, 15 h	90.8 ± 1.5	9.08 ± 0.15	0.60 ± 0.01
10	5	10	37 °C, 15 h	82.3 ± 1.0	8.23 ± 0.10	0.82 ± 0.01
5	5	10	37 °C, 15 h	65.6 ± 1.2	6.56 ± 0.12	1.31 ± 0.03
1	5	10	37 °C, 15 h	26.6 ± 0.9	2.66 ± 0.09	2.66 ± 0.13

Influence of the washing step after reaction: In order to minimize the number of steps in the general procedure for the determination of the product generated, the influence of the washing step after the reaction was evaluated. As described above, the general procedure consisted of separating the NRs by centrifugation after the reaction, washing them once with the same medium used for carrying out the reaction, and finally determining the amount of product formed by measuring the fluorescence in the total supernatant. The need of this washing step was evaluated by performing the procedure with and without this additional washing step. The obtained data are presented in Table S8 in which it is clear that depending on the substrate (**1** or **5**), and thus of the retention of the generated product within the pores of the ZIF-8 structure (*i.e.*, hydrophobicity/hydrophilicity, polarity, and so on), this step of washing is important for achieving a quantitative determination or not.

Table S8. Effect of washing step on the quantitative yield determination of the depropargylation of two different substrates promoted by NRs.

Catalyst type	Surface Pd (μM)	Substrate	Substrate (μM)	Product	Yield (%)	
					without washing	with washing
NCs	10	1	10	2	93.0 ± 3.8	97.0 ± 1.3
NCs	10	5	10	6	60.0 ± 6.1	85.7 ± 2.8

Leaking of Pd during the depropargylation of substrate 1: The stability of the Pd-NPs inside the ZIF-8 structure was studied by evaluating the potential leaking of Pd from the NRs during the reaction. To this end, the reaction was performed under the optimized conditions described above (used during the reaction of **1** as model) and the amount of Pd released to the supernatant after the reaction was quantified by ICP-MS. For comparison the same was done with the CTAB-protected Pd-NPs. Data presented in Table S9 are expressed in ppm (i.e., mg/L), showing that the amount of Pd released was much higher in the case of working with Pd-NPs while the leaching in the case of NRs was negligible. As we know the amount of total Pd in both Pd-NPs and NRs, the amount of released Pd was also expressed as percentage of the total Pd. These results clearly indicate that the Pd-NPs are well protected inside the ZIF-8 structure, avoiding not only their potential passivation by biomolecules as demonstrated above, but also their surface damage leading to the irreversible leaching of Pd from the catalyst.

Table S9 Leaking of Pd (ppm of Pd released) during the depropargylation reaction of **1** depending on the catalyst used as derived from ICP-MS analysis.

Catalyst type	Surface Pd (μM)	Pd released (ppm)	% Pd released
NRs	10	0.146 ± 0.011	0.081 ± 0.008
Pd-NPs	10	30.4 ± 2.0	16.6 ± 1.1

Reusability of NRs: In order to investigate the potential reuse of the NRs, after the reaction the NRs were collected by centrifugation, washed twice with water to remove potential remaining substrate/products, and redispersed in a fresh aqueous solution containing the substrate for a new run. The supernatants from each use were measured by fluorescence to quantify the amount of generated product. Using the substrate **1** the same procedure was carried out with Pd-NPs in order to compare the stability of NRs with that of Pd-NPs. Data presented in Table S10 clearly shows that the loss of efficiency of the NRs for promoting the depropargylation reaction was negligible after four runs.

Table S10 Yields of the depropargylation of two different substrates promoted by NRs or Pd-NPs after successive runs of the catalyst.

Catalyst type	surfacePd (μM)	Substrate	[Substrate] (μM)	Product	Yield (%) / Run number			
					1	2	3	4
NRs	10	**1**	10	**2**	97.0 ± 3.1	96.1 ± 2.5	98.0 ± 2.1	95.4 ± 3.4
Pd-NPs	10	**1**	10	**2**	19.0 ± 1.5	9.2 ± 2.1	5.0 ± 2.8	2.1 ± 2.7
NRs	10	**5**	10	**6**	80.3 ± 2.9	81.1 ± 3.2	77.9 ± 4.7	71.0 ± 6.1

Kinetic of the depropargylation reaction 1→ 2: To study the kinetic of the reaction of the substrate **1**, the reaction was evaluated as a function of time. Several reactions were carried out in parallel under identical conditions and each one was stopped at different time points. To this end, **1** (8 µL, 0.5 mM stock solution in MeOH) were added to a H_2O:MeOH 9:1 solution (342 µL) in a 1.5 mL HPLC vial (containing a stirring bar) followed by addition of an aqueous solution of NRs (50 µL, 2 nM; this is the concentration of NRs). The vial was sealed with a screw cap and the reaction mixture was stirred (400 rpm) at 37 °C. After different times, the reaction was stopped and the NRs were collected by centrifugation (7000 RCF, 10 min), and washed once with 400 µL of a H_2O:MeOH 9:1 solution. All the supernatants were collected and the fluorescence from product **2** was measured. The fluorescence intensity of **2** was plotted versus the time (see Figure S16) to obtain the kinetic curve. Moreover, the kinetic of the reaction of substrate **1** was evaluated also in the presence of **3** as interference, knowing that the depropargylation of substrate **3** is not promoted by the NRs. In this case 10 µM of **3** (8 µL, 0.5 mM stock solution in MeOH) was added together with 10 µM of **1** (8 µL, 0.5 mM stock solution in MeOH) to the reaction mixture.
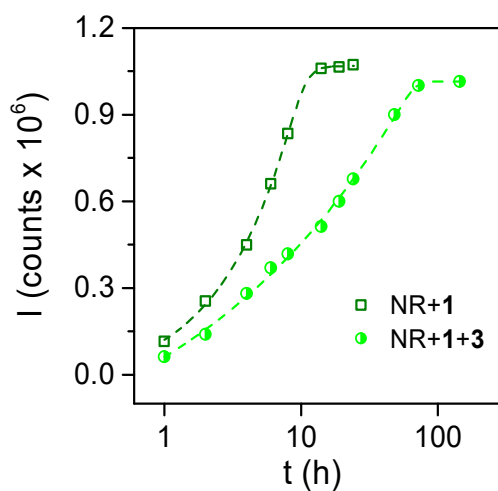

Figure S16. Kinetics of the depropargylation of substrate **1**, either by mixing NR with **1** in the absence (green) or presence of 1 eq. of **3** (light green). Dashed lines correspond to logistic fitting curves obtained with Originlab; R^2 >0.99.

In order to figure out a potential reason of the fact that the substrate **3** is not catalyzed by NRs, and additionally not only slow down the kinetic reaction of **1** but also it seems that a change of the slope in the kinetic curve takes place from 10 h, we carried out studies of the NRs after reaction by DLS and Z-Potential. As shown in Table S11, after the reaction of NRs with substrate **3** the hydrodynamic size of the NRs increased, and a decrease of the negative charge was also observed. This could be attributed to a binding of some molecules of substrate **3** on the surface of NRs, avowing their diffusion into the NR core, and also partially blocking the diffusion of substrate **1**. In contrast, the substrate **1** did not cause any significant change in the NRs.

Table S11. Hydrodynamic diameters d_h (mean value ± SD) as derived from DLS measurements of the NRs dispersed the reaction mixture before reaction and after reaction with substrate **1** or **3** in $H_2O/MeOH$ 9:1. SD values correspond to the standard deviation of the diameter mean value as obtained from several repetitions (n=3) of the measurement. The polydispersity index (PDI) and ζ-potential values are also given.

Parameter	before reaction	After reaction with	
		1	3
d_h (nm)	249 ± 3	252 ± 4	306 ± 3
PDI	0.10	0.12	0.11
ζ (mV)	-34.5 ± 0.5	-34.4 ± 0.8	-26.5 ± 0.7

Performance of the NRs as "continuous" nanoreactors: The performance of the NRs for promoting the depropargylation reaction of **5** by in three successive steps was studied as follows: for 1 cycle, **5** (8 µL, 0.5 mM stock solution in MeOH) was added to a PBS:MeOH 8:2 solution (342 µL) in a 1.5 mL HPLC vial (containing a stirring bar) followed by addition of an aqueous solution of NRs (50 µL, 2 nM; this is the concentration of NRs). The vial was sealed with a screw cap and the reaction mixture was stirred (400 rpm) at 37 °C. After 18 h, the NRs were collected by centrifugation (7000 RCF, 10 min), and the supernatant was separated. The precipitate was washed once with 400 µL of a 8:2 PBS:MeOH solution, centrifuged again (7000 RCF, 10 min), and the supernatant was separated and mixed with the first supernatant. The generated product in the supernatant was measured by fluorescence. For 2 successive cycles, the reaction was carried out in identical conditions and after 18 h, instead of purified the product, another shot of **5** (8 µL, 0.5 mM stock solution in MeOH) was added to the reaction mixture. The mixture was left to react 18 h, with stirring and at 37 °C, and afterwards the total generated product was separated and quantify as described in first cycle. The same was repeated with one more addition for 3 cycles. Results are presented in Table S12.

Table S12 Cumulative yield of the depropargylation of **5** promoted by NRs after successive reuses of the catalyst.

Catalyst type	surface-Pd (µM)	Cycles Number	[Substrate] (µM)	Product	Cumulative Yield (%)
NRs	10	1	10	**2**	94.6 ± 5.3
NRs	10	2	10 + 10	**2**	178.4 ± 6.8
NRs	10	3	10 + 10 + 10	**2**	250.6 ± 8.1

Reverse phase high-performance liquid chromatography- diode array detector/mass spectrometry (RP-HPLC-DAD/MS) characterization of the NR-promoted depropargylation of the cresyl violet 5: The depropargylation reaction of substrate 5 promoted by NR was carried out in slightly different conditions as described above in the general procedures section, in order to obtain the product 6 concentrated enough for their posterior analysis. Specifically, the substrate solution (8 µL, 0.5 mM stock solution in MeOH) was added to a PBS:MeOH 1:1 solution (342 µL) in a 1.5 mL HPLC vial (containing a stirring bar) followed by addition of an aqueous solution of NRs (50 µL, 2 nM; this is the concentration of NRs). The vial was sealed with a screw cap and the reaction mixture was stirred (400 rpm) at 37 °C. This was performed in parallel in 5 vials. After overnight (15 h), the NRs were collected by centrifugation (7000 RCF, 10 min), and the supernatants were separated. The precipitates were washed once with 400 µL of MeOH solution, centrifuged again (7000 RCF, 10 min), and all the supernatants from the different vials were mixed. This supernatant was preconcentrated by evaporation of the MeOH solvent, and 100 µL of DMSO was added to avoid the precipitation of the product and unreacted substrate. Finally, this supernatant was analyzed by RP-HPLC-DAD/MS, and as controls the pure substrate and product were also analyzed (Figure S17).
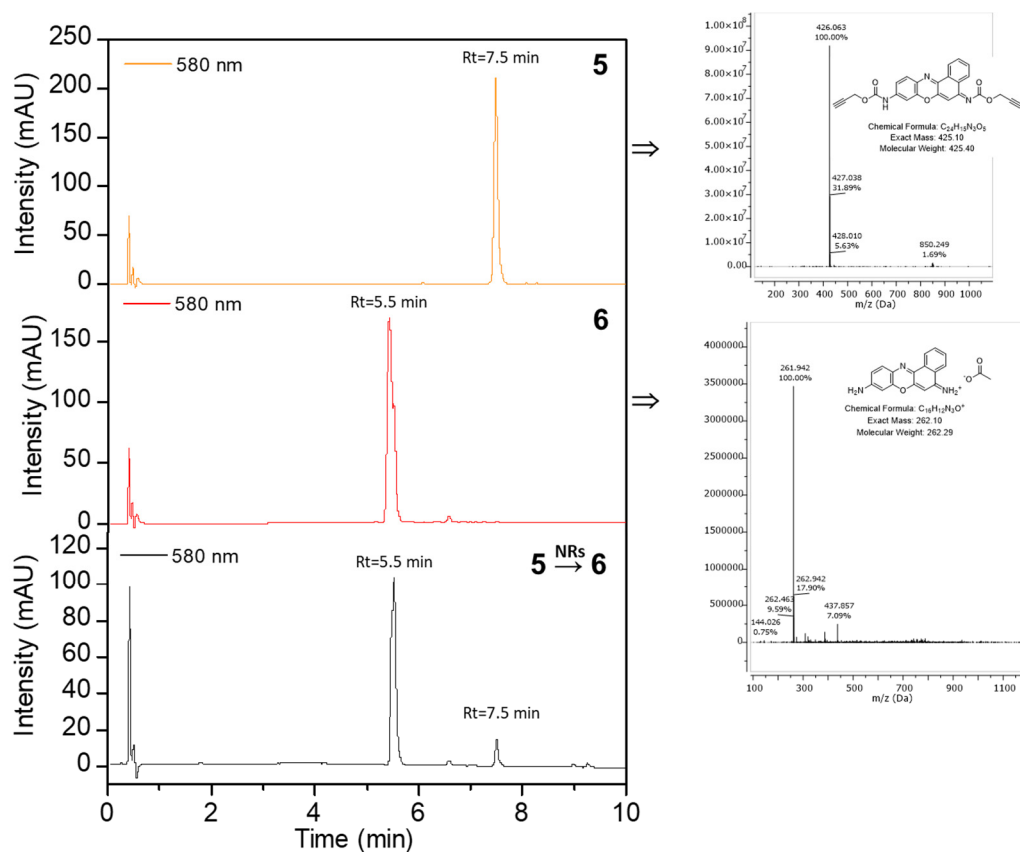

Figure S17. RP-HPLC-DAD chromatogram (left) and ESI-MS spectra (right) of compound 5, RP-HPLC-DAD chromatogram (left) and ESI-MS spectra (right) of compound 6, and RP-HPLC-DAD chromatogram (left) of the obtained reaction mixture promoted by NRs.

Performance of the reactions in the presence of bio-additives

Reaction of substrate 1 in the presence of additives: The reaction was carried out as described in the previous section, but adding the following additives (Table S13): (i) different amounts of BSA (for a final concentration in the total volume of 40 µM, 80 µM, or 150 µM); (ii) DMEM (supplemented with 10 % FBS), and in this case the reaction was studied after 15 h and 72 h; (iii) 5 mg/mL of cell lysate.

Reaction of substrate 5 in the presence of additives: The reaction was carried out as described in the previous section, but adding the following additives (Table S13): (i) different amounts of BSA (for a final concentration in the total volume of 40 µM, 80 µM, or 150 µM); (ii) 5 mg/mL of cell lysate.

Cell Lysate preparation: For the preparation of the HeLa cells lysates, 3×10^6 exponentially growing HeLa cells were washed twice with PBS, scrapped with a rubber policeman in 0.5 mL of PBS, and sonicated intensely for 2 rounds of 1 min with a 30 second cooling period in between. The protein concentration of the lysates was quantified by DCTM Protein Assay (BioRad) and equalised to 10 mg/mL for reproducibility among experiments.

Table S13. Reaction yields of the depropargylation of two substrates promoted by NRs or Pd-NPs in the presence of different bioadditives.

Catalyst type	surface-Pd (µM)	Additive	Substrate	[Substrate] (µM)	Product	Yield (%)
NRs	10	-	1	10	2	97.0 ± 1.3
NRs	10	BSA, 40 µM	1	10	2	55.0 ± 3.0
NRs	10	BSA, 80 µM	1	10	2	53.0 ± 2.9
NRs	10	BSA, 150 µM	1	10	2	33.0 ± 3.5
Pd-NPs	10	-	1	10	2	19.0 ± 1.5
Pd-NPs	10	BSA, 40 µM	1	10	2	9.0 ± 1.6
Pd-NPs	10	BSA, 80 µM	1	10	2	7.0 ± 2.0
Pd-NPs	10	BSA, 150 µM	1	10	2	7.0 ± 2.1
NRs	10	DMEM, 10%, 15h	1	10	2	22.0 ± 3.2
NRs	10	DMEM, 10%, 72h	1	10	2	47.0 ± 3.7
NRs	10	Lysate, 5 mg/mL	1	10	2	19.0 ± 2.8
NRs	10	-	5	10	6	84.8 ± 2.5
NRs	10	BSA, 20 µM	5	10	6	62.8 ± 2.3
NRs	10	BSA, 40 µM	5	10	6	54.1 ± 2.9
NRs	10	BSA, 8 µM	5	10	6	23.8 ± 3.9
NRs	10	Lysate, 5 mg/mL	5	10	6	22.5 ± 4.1

Cell studies

Cell culture: HeLa (cervical cancer cell line) were cultured in Dulbecco's Modified Eagle's Medium with phenol red, 4.5 g/L D-glucose, L-glutamine and pyruvate (DMEM, 1X, Gibco, #41966-029) supplemented with 10% Fetal Bovine Serum (Gibco, #10270-106) and 1% Penicillin Streptomycin (P/S, Corning, 100X, #30-002-CI). Cells were maintained under humid conditions at 37 °C and 5% of CO_2. Cells were passaged after cleaning Dulbecco's Phosphate Buffered Saline (DPBS, 1X, Gibco, #14190-094) with 0.25% Trypsin-EDTA (1X, Gibco, 25200-056) when the culture reached confluency.

Cell Viability: In order to study number of viable cells after the exposure to the substrates, Pd-NPs and/or NRs, we carried resazurin assays (Figure S18). HeLa cells were seeded in 96-well plates (NEST Scientific, #701001), $7.5 \cdot 10^3$ cells per well in 100 μL of cell growth medium (0.3 cm^2 per well) 24 h before the exposition. Then media was removed and 100 L of cell culture growth medium with the desired concentration of the substrates, Pd-NPs and/or NRs s were added. The cells were incubated with the samples the time of interest at 37 °C and 5% CO_2. After that, we rinsed each well three times with PBS and added 100 μL of freshly prepared solution with 90% of media and 10% of resazurin (resazurin sodium salt in water 0.2 mg/mL filtered; Resazurin Sodium Salt, Sigma Aldrich, #199303-1G). Cells were incubated at 37 °C and 5% CO_2 under dark conditions.

Non-fluorescent resazurin (Alamar blue) is oxidized by living cells into its fluorescent product resorufin (excitation at 579 nm and emission at 584 nm). In this way, the fluorescence intensity of each well is proportional to the number of living cells there. After the incubation time, plates were measured with a plate reader (Infinite® 200 PRO, Tecan, Switzerland) under 560±20 nm excitation and collecting fluorescence with a 610±20 nm filter. The fluorescence value of each well provided by the instrument is an average of nine consecutive measures in the same well. Final intensity value for control cells (I_C), the ones that were not treated, is an average of, at least, nine different well values. Final intensity values for samples (I_S) are a mean of three independent well values. So, we can calculate the final cell viability values as:

$$\text{cell viability (\%)} = \frac{I_S}{I_C} \cdot 100$$

Pd content per cell. ICP-MS was used to quantify the average Pd content per cell, which we used to estimate the number of Pd-NPs or NRs per cell (Table S14); see calculations in Section IV "Quantification of Pd by inductively coupled plasma mass spectrometry (ICP-MS) and estimation of Pd potentially active". Note that to estimate the number of particles per cell, we assume that the particles (Pd-NPs or NRs) retain their original Pd content; however, in contrast to the Pd-NPs, such assumption seems valid for the NRs according to the stability data (Table S2). HeLa cells ($\sim 6.4 \cdot 10^6$ cell per experiment) were cultured as previously discussed, supplemented with Pd-NPs or NRs (50 pM   2 μM in surface Pd, equivalent to $\sim 5.7 \cdot 10^3$ particles per cell), and incubated overnight. Extracellular Pd (either free, Pd-NP or NRs) were washed out, and the Pd-loaded cells were digested with aqua regia (see detailed procedures in previous work[10]).

Table S14. Amounts of Pd per cell and particle uptake % (measured-to-added) as derived from ICP-MS measurements.

Particle	Pd per particle (μg)*	Cells (No.)	Particles per cell (added)	ICP-MS		
				Pd per cell (μg)	Particle per cell (No.)	% particle internalization#
Pd-NPs	$1.7 \cdot 10^{10}$	$6.5 \cdot 10^5$	$5.6 \cdot 10^3$	$1.2 \cdot 10^{-8} \pm 8.9 \cdot 10^{-11}$	71 ± 1	0.5
NRs	$1.7 \cdot 10^{10}$	$6.3 \cdot 10^5$	$5.8 \cdot 10^3$	$2.0 \cdot 10^{-8} \pm 2.5 \cdot 10^{-10}$	120 ± 1	0.8

*See section S4.

#Assuming particles retain their Pd original content inside cells.

Confocal imaging: In order to perform all the confocal imaging experiments with living cells, $20 \cdot 10^3$ HeLa cells (200 µL) were seeded on µ-Slide 8 well-ibiTreat chambers (1 cm² per well, Ibidi, Germany, #80826) at least 12 h before NR/substrate exposure. Organelle staining with LysoTracker Blue (#L7525), MitoTracker Green (#M7514) and CellMask Deep Red (#H32721) was performed following provider (Thermo Fisher Scientific) instructions. Confocal images of living cells were captured on an Andor Dragonfly spinning disk confocal system mounted on a Nikon TiE microscope equipped with a Zyla 4.2 PLUS camera (Andor, Oxford Instruments) and an OKO-lab incubator to keep cells at 37 °C during all the experiment. Images were taken with different magnification objectives (60x, 100x). All the images were processed with ImageJ.

Confocal microscopy images of the NR system in which PMA was fluorescently labeled (covalently) with a rhodamine (tetramethylrhodamine 5-(and-6)-carboxamide cadaverine),[9] are shown in Figure S19, aiming to illustrate the efficient cell internalization (HeLa cells) of the proposed NRs (50 pM) and colocalization with lysosomes. Note that we used equivalent particle (NR or Pd-NP) incubation conditions in all the cell studies.

Excitation/Emission wavelengths used for confocal imaging of the rhodamine-labeled NRs/product **6** are 561/620(60).

Depropargylation reactions inside cells. Different concentrations of the substrate **5** (Figure S20-21) were added to cells pretreated with NRs or Pd-NPs (50 pM, overnight). The productions of **6** was inspected by checking the intracellular fluorescence after the time of interest (1-24 h).

For the study of the depropargylation of **5** over time (Figure S21-24), we preload the cells with the NR (50 pM) overnight and, after three washing steps with PBS to remove the excess of NR non-associated with cells, substrate **5** (10 µM) was added with fresh medium. We incubated the substrate **5** during 1, 3, 6 and 24 h. Washing steps to remove extracellular excess of **5** and or **6** were not required before confocal inspection.

Controls were carried with the same concentrations of **5** but with Pd-free cells (Figure S25).

We also confirmed that Pd-NPs (50 pM ≈ 2 µM in surface Pd, overnight) without the MOF shell, or a series of discrete Pd complexes (**Pd-1**, **Pd-2** and **Pd-3**; 2 µM Pd, overnight), promote the intracellular depropargylation of the substrate **5** (Figure S26), although with much less efficiency than the NRs (Figure S21-24).

Intracellular recycling. In order to study the reusability of our cell-nanoreactor for the depropargylation of **5**, we stopped the incubation of the substrates with NR-preloaded cells after the time of interest (substrate **5**: 20 µM, 3 h). Then, the intracellular production of **6** was inspected under the microscope; notice that washing to remove extracellular substrates/products step was not required for visualizing the depropargylation of **5**.

Next, before adding a second shot of **5** (10 µM, 3 h), we cleaned with PBS, added fresh complete DMEM and waited for the cells to "wash away" **6** (~ 3 h, cleansing). We repeated these steps to complete up to four cycles (Figure S27).

As controls for the recycling experiments, we also performed similar studies for the depropargylation of **5** (two runs) but using Pd-NPs (50 pM ≈ 2 µM in surface Pd, overnight) or the discrete Pd complexes (Pd-1, Pd-2 or Pd-3; 2 µM Pd, overnight). However, such alternative Pd catalysts were unable to achieve a second depropargylation cycle, at least to any degree observable by the intracellular fluorescence of **6** (Figure S26).

Depropargylation and recycling in 3D NR-preloaded HeLa spheroids. Spheroids of HeLa cells were cultured in 96 well plates previously treated with agarose as follows:[11] a 1% agarose solution in filtered PBS was heated until

100 °C; the tips and the 96-well plate was pre-warmed in the incubator for ~ 1 h, and 40 µL of the agarose solution were added to each well; the agarose filled wells were led to cool down during, at least, 30 minutes in sterile conditions. Then, we confirmed a homogeneous agarose gelation without bubbles by inspection under the microscope. Once agarose was solidified, 100 µL of cells (NR-preloaded or "empty") solution at different concentrations were added slowly. Cells were led to attach to each other during 24 hours before checking the spheroids formation. After 24 h, the sizes of spheroids were between 0.4 and 1 µm when varying total cells amounts from ~ $1 \cdot 10^4$ to $3 \cdot 10^4$ cells per spheroid (Figure S28). Media of the wells containing the spheroids were changed daily.

For spheroids imaging, spheroids formed as previously discussed were placed onto a µ-plate angiogenesis 96 well (0.125 cm^2 per well, Ibidi, Germany #89646) using a pipette with a sterile cut tip to facilitate the spheroid´s manipulation. Using an Andor Dragonfly spinning disk confocal system with the 20x objective, spheroids were observed in the brightfield channel (Figure S28) and in the Cy3 channel (wavelengths: excitation 561 nm; emission 620(60) nm) where the fluorescence from TAMRA (Figure S29) or from the depropargylation of **5** (Figure S30) were collected. For the bigger ones (~ 1 µm in diameter), 4 different images in the plane XY were required. Z-scans were made with ~ 300 different stack images in the Z axis. 3D reconstructions were done with ~ 300 stack images (total thickness ~ 150 µm; step thickness ~ 0.5 µm). Scale bars correspond to 100 µm (20x). In order to treat the 2D images as well as to crop or stitch 4x4 images, ImageJ was used. Deconvolution of the z-scans were done with Fusion software and finally, for 3D reconstructions, Imaris software (Oxford Instruments) was used.

In order to form spheroids with catalytic properties, $2 \cdot 10^4$ cells per well were seeded on 6 well plates. After 24 hours of cell attachment, cells were treated with the NRs (50 pM, overnight) as previously discussed. Notice that non-treated cells were always seeded and maintained as control, to form control non-catalytic spheroids. Once the NR were internalized, extracellular NRs were washed three times with fresh PBS. Cells were trypsinized with 200 µL of trypsin and neutralized with 2 mL of DMEM (10% FBS). After that, dilutions were made to obtain the desired number of cells in 100 µL. After one day of spheroids formation, the medium was removed and fresh medium containing **5** (20 µM) was added to both NR-loaded spheroids and control spheroids without NRs (Figure S30). After 24 hours, spheroids were checked under the confocal microscope. Media was removed and the spheroids were thoroughly washed (3x) with PBS to remove extracellular substrates and/or products and fresh medium was added, which facilitated the cleansing of **6** during 24 h. After cleansing, a second addition of **5** (24 hours, 20 µM) were added to confirm that the spheroids were still catalytic and confirm reusability.
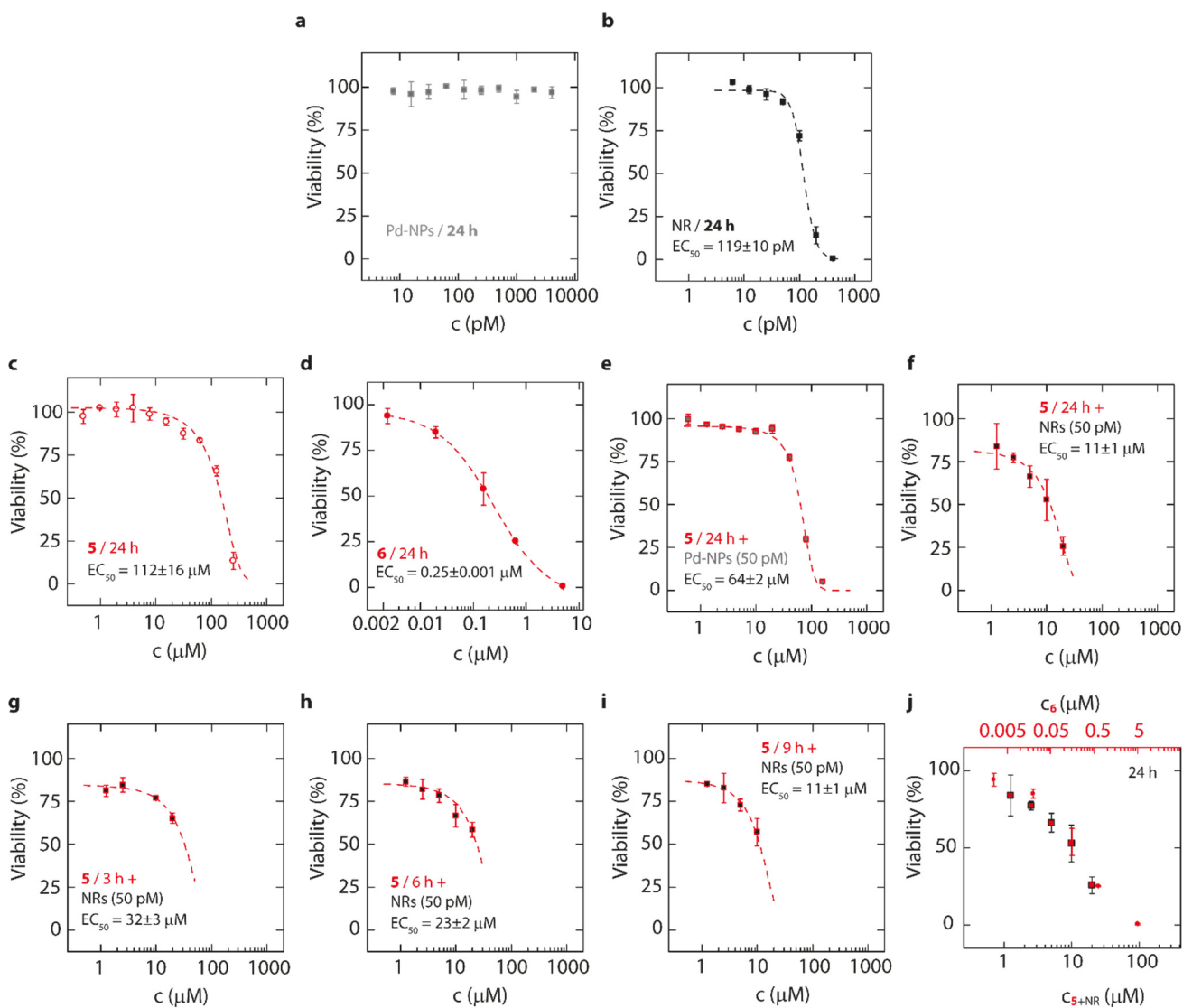
Figure S18. Cell viability using the resazurin assay of HeLa cells exposed to increasing concentrations of reactant(s) and/or NRs and/or Pd-NPs. Half-maximal responses (EC$_{50}$ values) were estimated by fitting (Dose Response function in OriginLab). a) Pd-NPs (50 pM), 24 h incubation; b) NRs (50 pM), 24 h incubation; c) **5**, 24 h incubation; d) **6**, 24 h incubation; e) **5**, 24 h incubation with Pd-NPs (50 pM)-preloaded cells; f) **5**, 24 h incubation with NR (50 pM)-preloaded cells; g) **5**, 3 h incubation with NR (50 pM)-preloaded cells; h) **5**, 6 h incubation with NR (50 pM)-preloaded cells; i) **5**, 9 h incubation with NR (50 pM)-preloaded cells; j) comparison between the incubation (24 h) of **6** with Pd-free cells and **5** with NR (50pM)-preloaded cells.

Figure S19. Collage of confocal microscopy images. a1,a2,a3) Rhodamine-labelled NRs (pink); b1,b2,b3: Rhodamine-labelled NRs (pink) + LysoTracker® Blue (cyan); c1,c2,c3) Display of colocalization of NR and

LysoTracker® Blue (Pearson correlation coefficient: 0.42 ± 0.05, n=5); d1,d2,d3) LysoTracker® Blue + MytoTracker® Green + CellMaskTM Deep Red; e1,e2,e3: d1,d2,d3 + rhodamine-labelled NRs (pink); f1,f2,f3: Display of colocalization of NR and MitoTracker® Green (Pearson correlation coefficient: -0.23 ± 0.04, n=5) . Scale bars correspond to 40 μm. Colocalization analysis in fluorescence was performed with ImageJ (Coloc 2 Fiji's plugin for colocalization analysis).
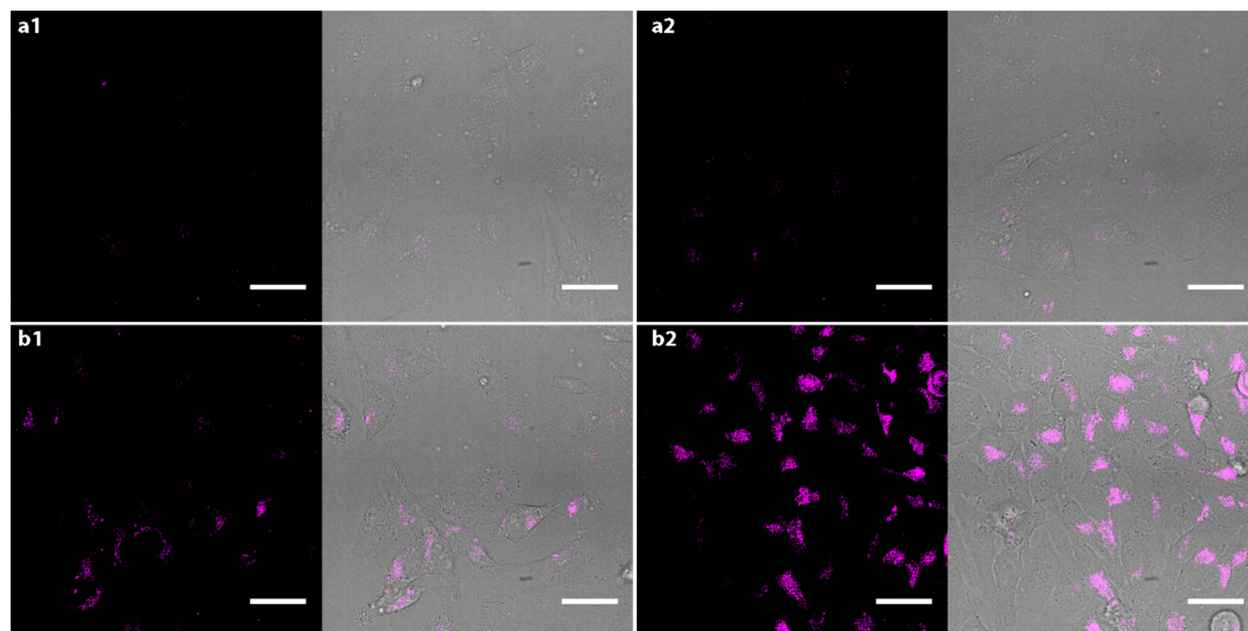
Figure S20. Collage of confocal microscopy images (left: pink channel; right: merged pink + bright-field; 60x) for the production of **6** after 6 h incubation with NR-preloaded cells (using 2.5 μM of **5**); a1-a2) controls without NRs; b1-b2) two examples using NR-preloaded cells as previously discussed. Scale bars correspond to 40 μm.
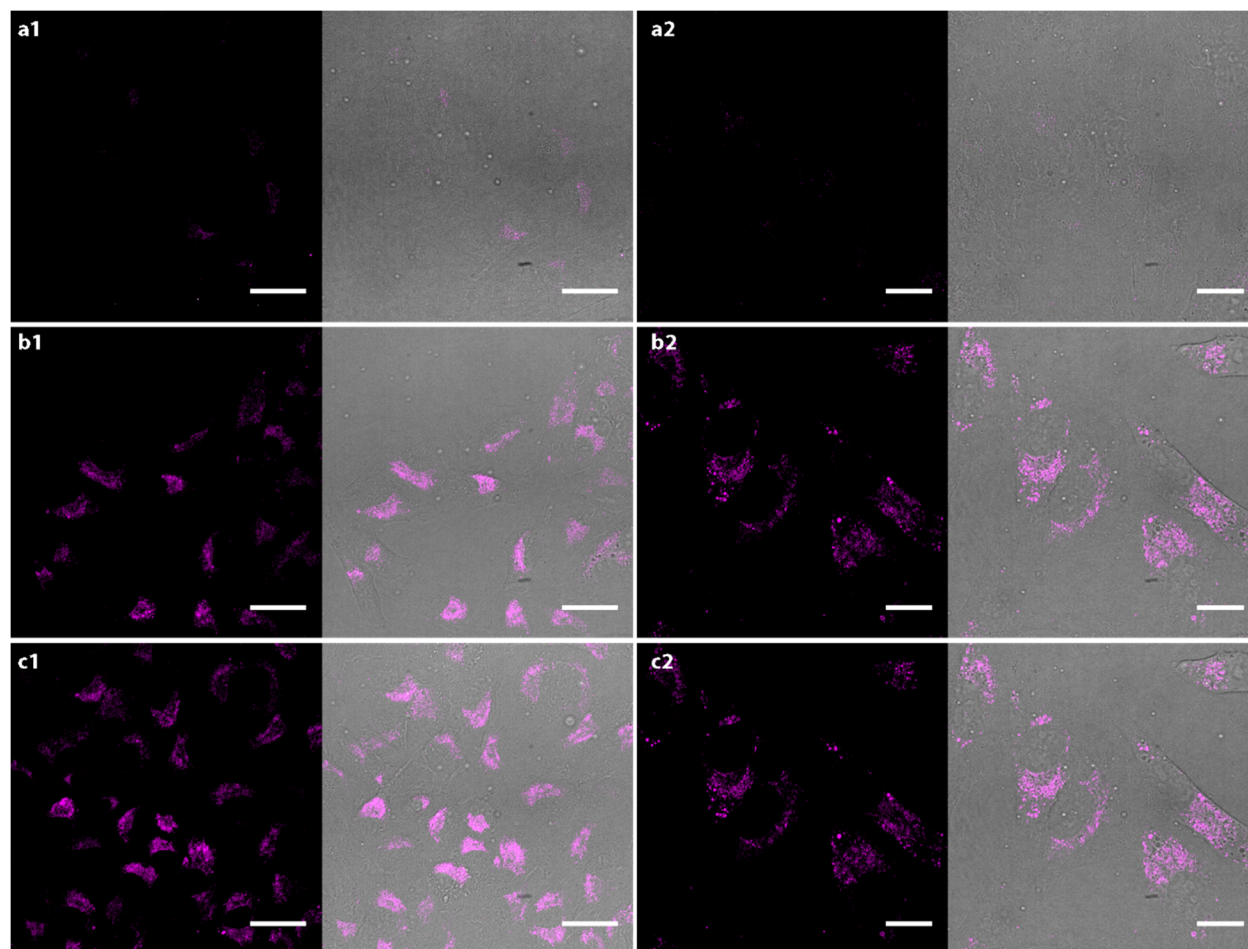
Figure S21. Collage of confocal microscopy images (left: pink channel; right: merged pink + bright-field; 60x) for the production of **6** after 1 h incubation with NR-preloaded cells (using 10 μM of **5**); a1-a2) controls without NRs (a1: 60x; a2: 100x); b1-c1) two examples using NR-preloaded cells as previously discussed (60x); b2-c2) two examples using NR-preloaded cells as previously discussed (60x). Scale bars correspond to 20 μm (100x) or 40 μm (60x).
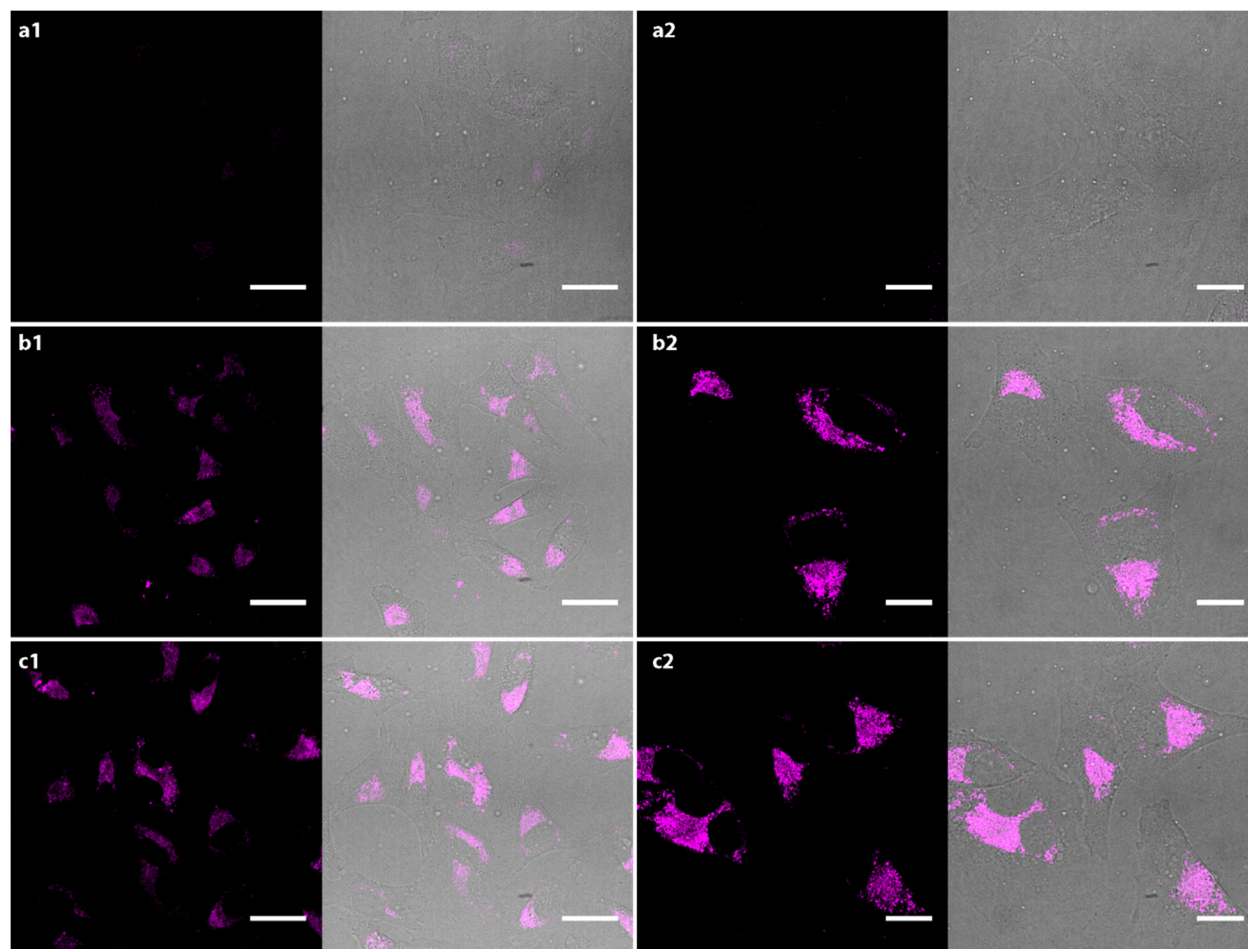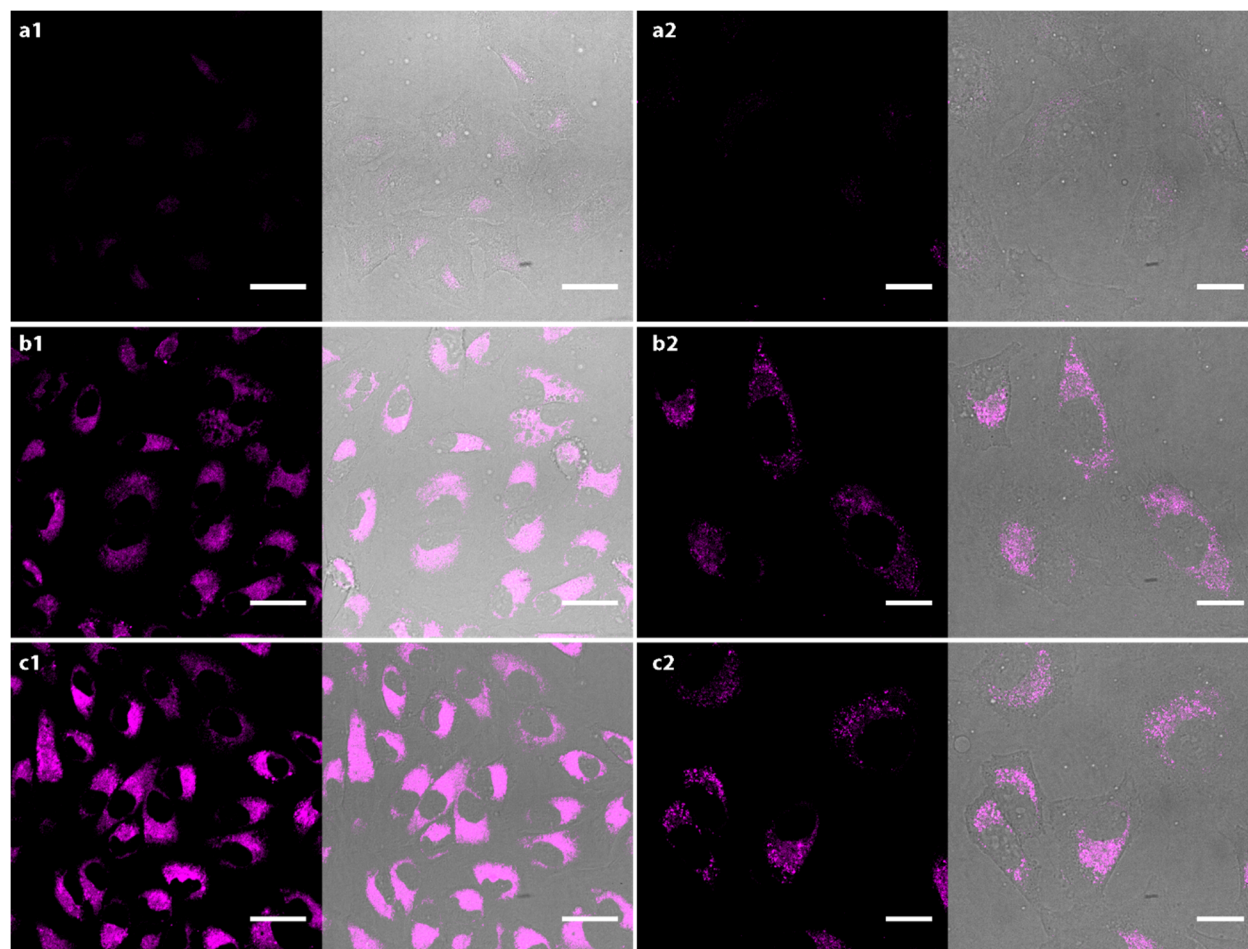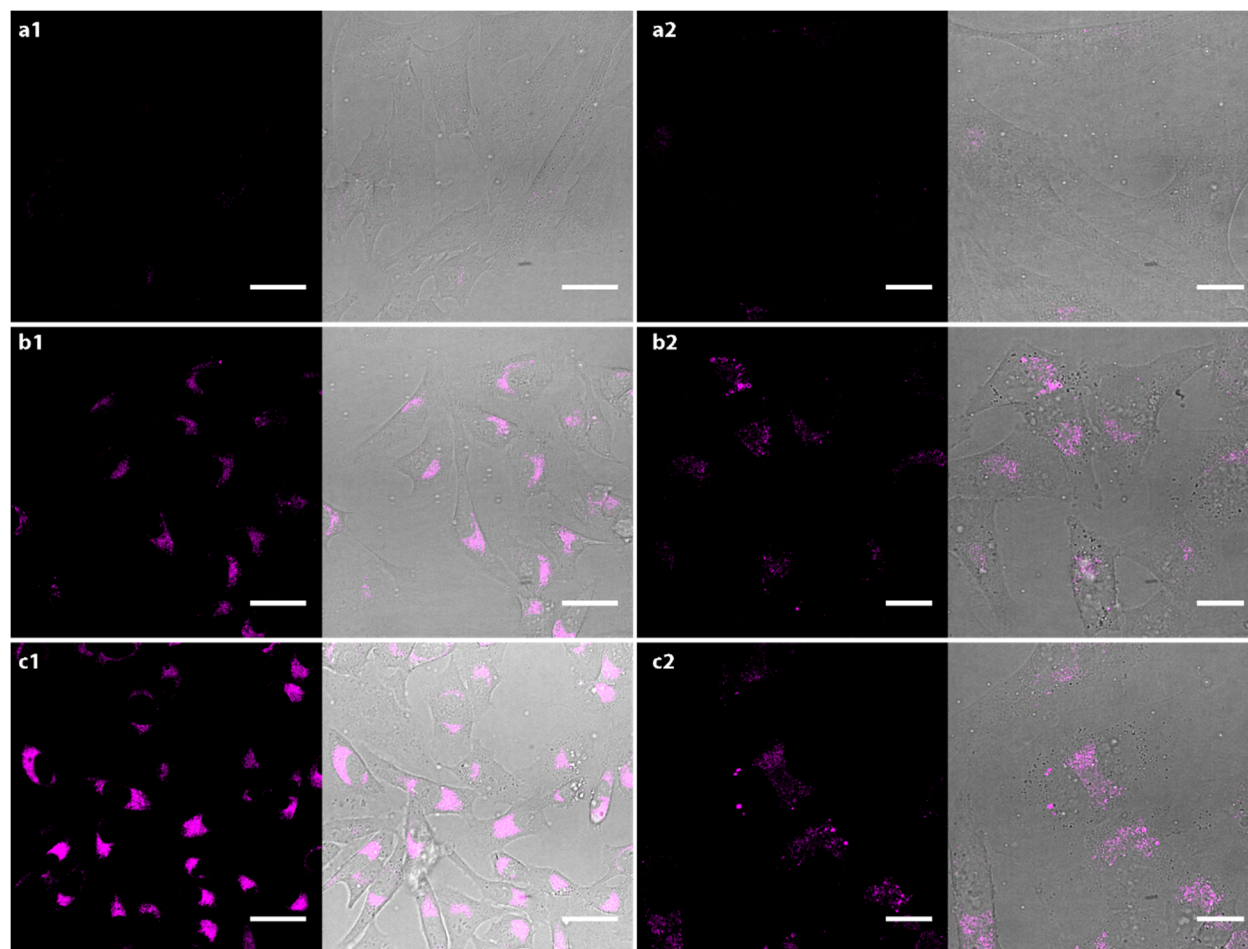
Figure S22. Collage of confocal microscopy images (left: pink channel; right: merged pink + bright-field; 60x) for the production of **6** after 3 h incubation with NR-preloaded cells (using 10 µM of **5**); a1-a2) controls without NRs (a1: 60x; a2: 100x); b1-c1) two examples using NR-preloaded cells as previously discussed (60x); b2-c2) two examples using NR-preloaded cells as previously discussed (60x). Scale bars correspond to 20 µm (100x) or 40 µm (60x).

Figure S23. Collage of confocal microscopy images (left: pink channel; right: merged pink + bright-field; 60x) for the production of **6** after 6 h incubation with NR-preloaded cells (using 10 µM of **5**); a1-a2) controls without NRs (a1: 60x; a2: 100x); b1-c1) two examples using NR-preloaded cells as previously discussed (60x); b2-c2) two examples using NR-preloaded cells as previously discussed (60x). Scale bars correspond to 20 µm (100x) or 40 µm (60x).
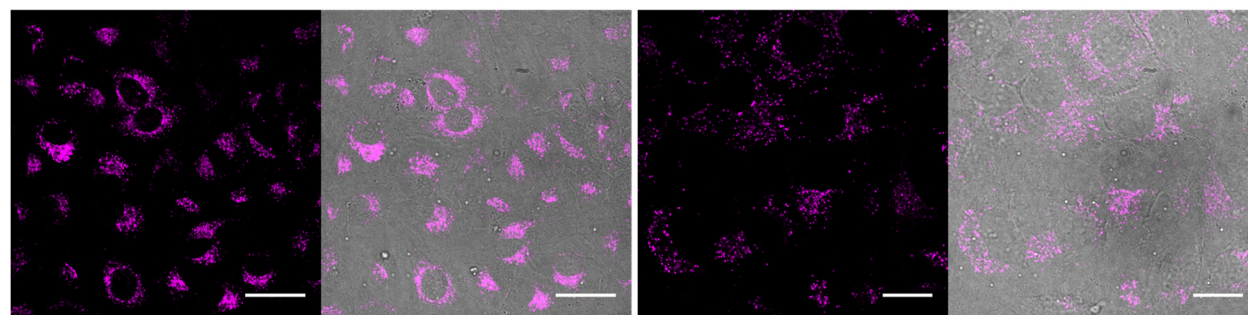
Figure S24. Collage of confocal microscopy images (left: pink channel; right: merged pink + bright-field; 60x) for the production of **6** after 24 h incubation with NR-preloaded cells (using 10 μM of **5**); a1-a2) controls without NRs (a1: 60x; a2: 100x); b1-c1) two examples using NR-preloaded cells as previously discussed (60x); b2-c2) two examples using NR-preloaded cells as previously discussed (60x). Scale bars correspond to 20 μm (100x) or 40 μm (60x).

Figure S25. Collage of confocal microscopy images (left: fluorescence channel; right: merged fluorescence + bright field; 60x and 100x) for the incubation of **6** with Pd-free cells; cells were incubated with **6** (0.2 μM) for ~1 h. Before microscope inspection, cells were washed to remove extracellular probes. Scale bars correspond to 20 μm (100x) or 40 μm (60x).
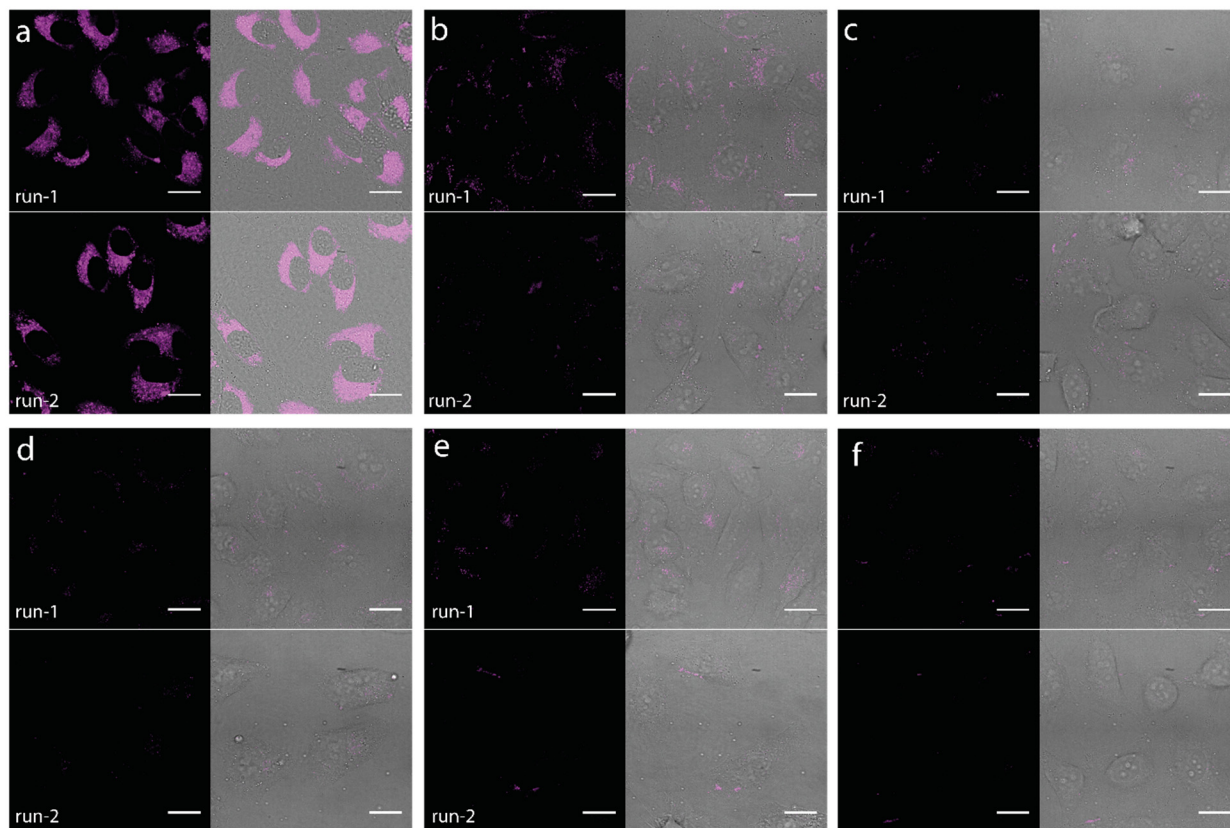
Figure S26. Collage of confocal microscopy images (left: pink channel; right: merged pink + bright-field; top: first generation run; bottom: second generation run using the same catalyst-preloaded cells) for the production of **6**, using cells preloaded with (a) NR (50 pM 2 µM in surface Pd, overnight), (b) Pd-NP (50 pM 2 µM in surface Pd, overnight), of discrete Pd complexes (c) Pd-1, (d) Pd-2, or (e) Pd-3, which were incubated with **5** (10 µM) for ~ 6 h before microscope inspection. f) Control experiments using "empty" cells (Pd "free" cells). Scale bars correspond to 20 µm. All these experiments were carried out using exactly the same experimental conditions.
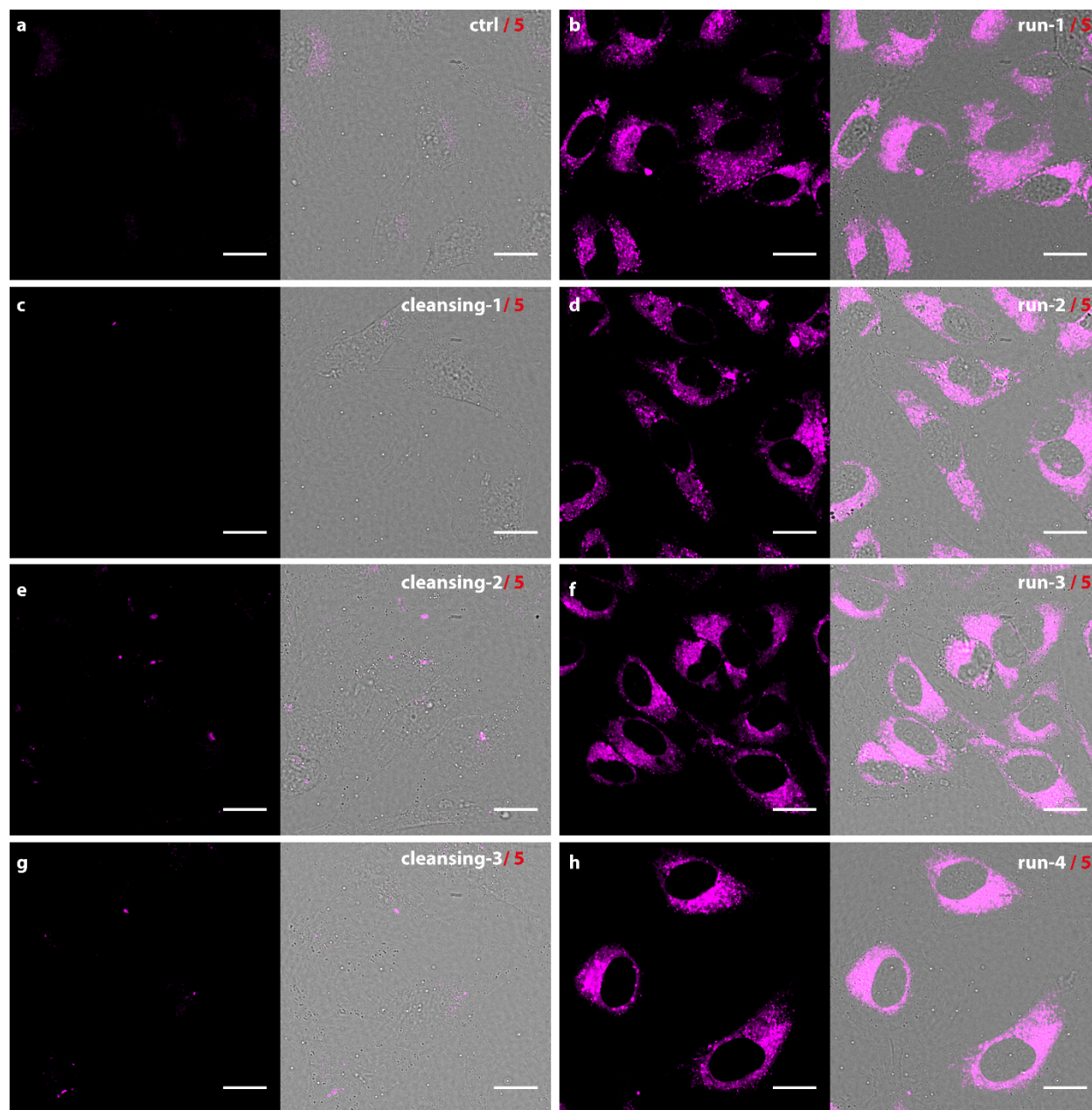
Figure S27. Collage of confocal microscopy images (left: pink channel; right: merged pink + bright-field). a) Control without NRs and the addition of substrate **5** (20 µM). b-g) First, second and third generation runs using the same NR-preloaded cells and recorded by confocal microscopy; b,d,f) generation of **6** after 3 h incubation of **5** (20 M); c,e,g) 3 h cleansing. h) fourth reaction cycle. Scale bars correspond to 20 µm.

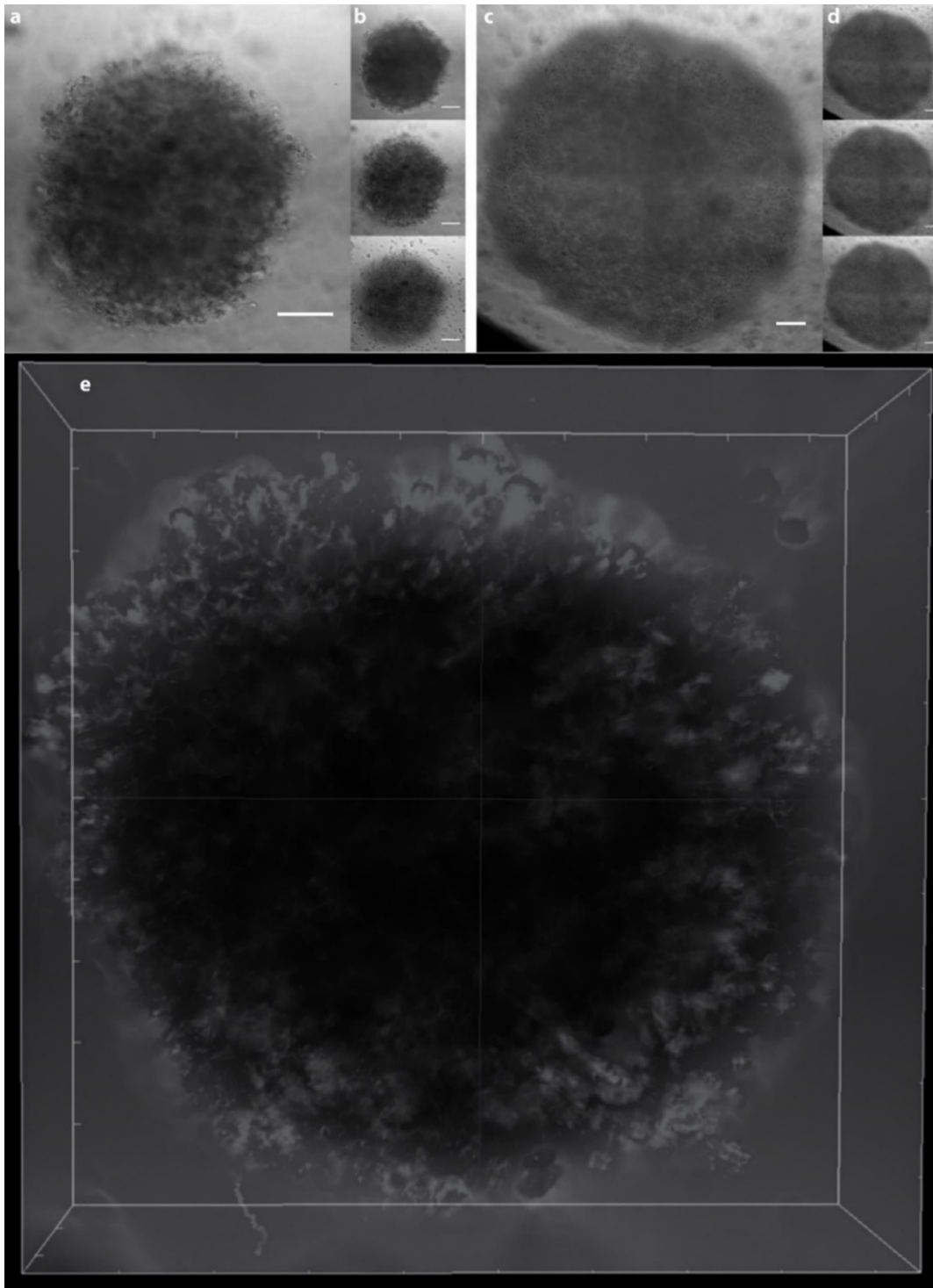**Figure S28.** Collage of brightfield images of 3D HeLa (Pd "free" spheroids). a) HeLa spheroid with diameter ~ 0.4 µm (1 image per stack); b) Three different stacks of the spheroid shown in a. c) HeLa spheroid with diameter ~ 1 µm (4 images in each plane); d) Three different stacks of the spheroid shown in c. e) 3D reconstruction (top-view) of a spheroid with diameter ~ 0.4 µm. Scale bars correspond to 100 µm.
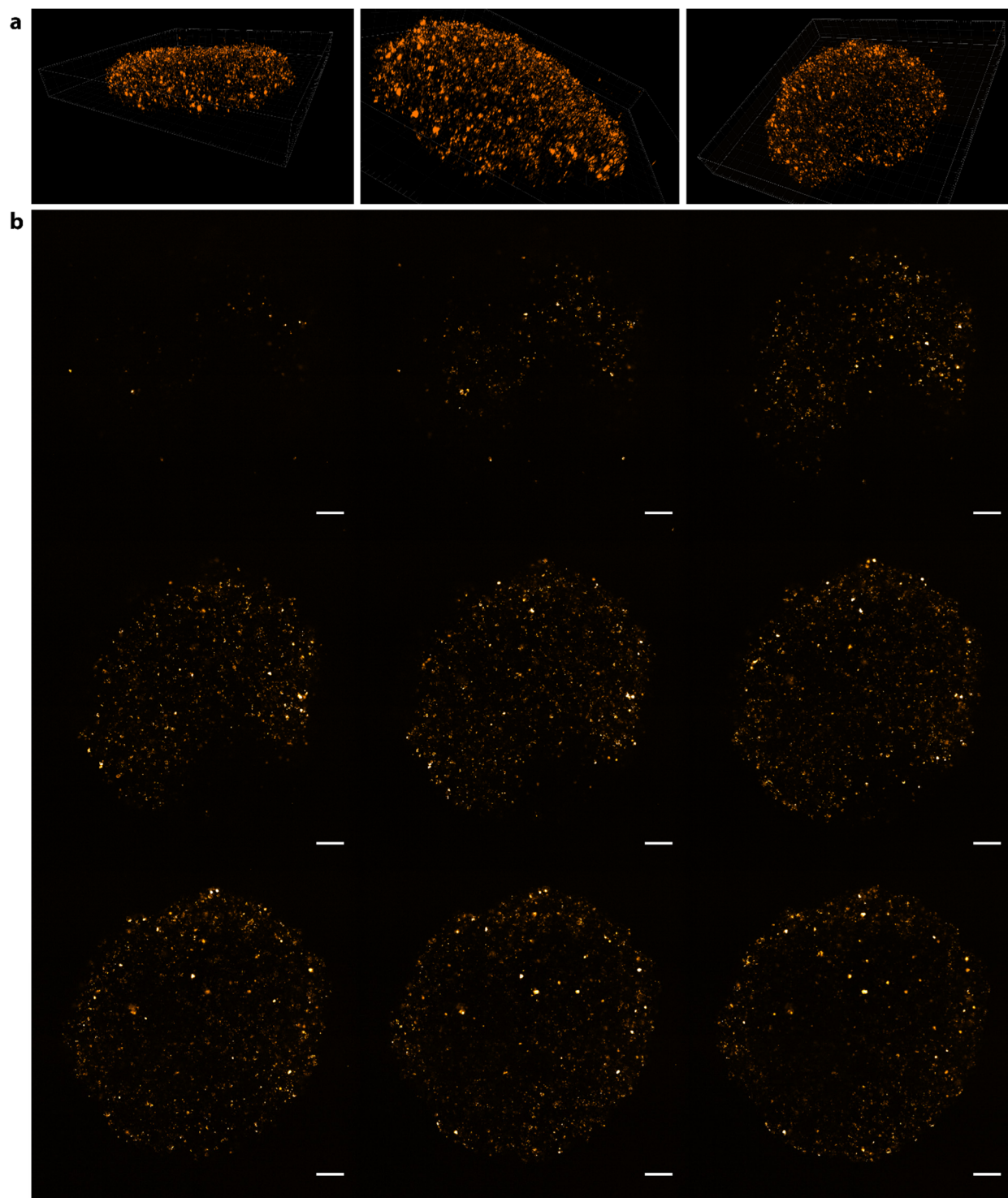
Figure S29. Collage of confocal images of 3D spheroids of HeLa cells loaded with TAMRA-labeled NRs. a) Three different views of a 3D reconstruction of a NR-loaded spheroid with diameter ~ 1 μm. b) Different stacks of the spheroid shown in a. Scale bars correspond to 100 μm
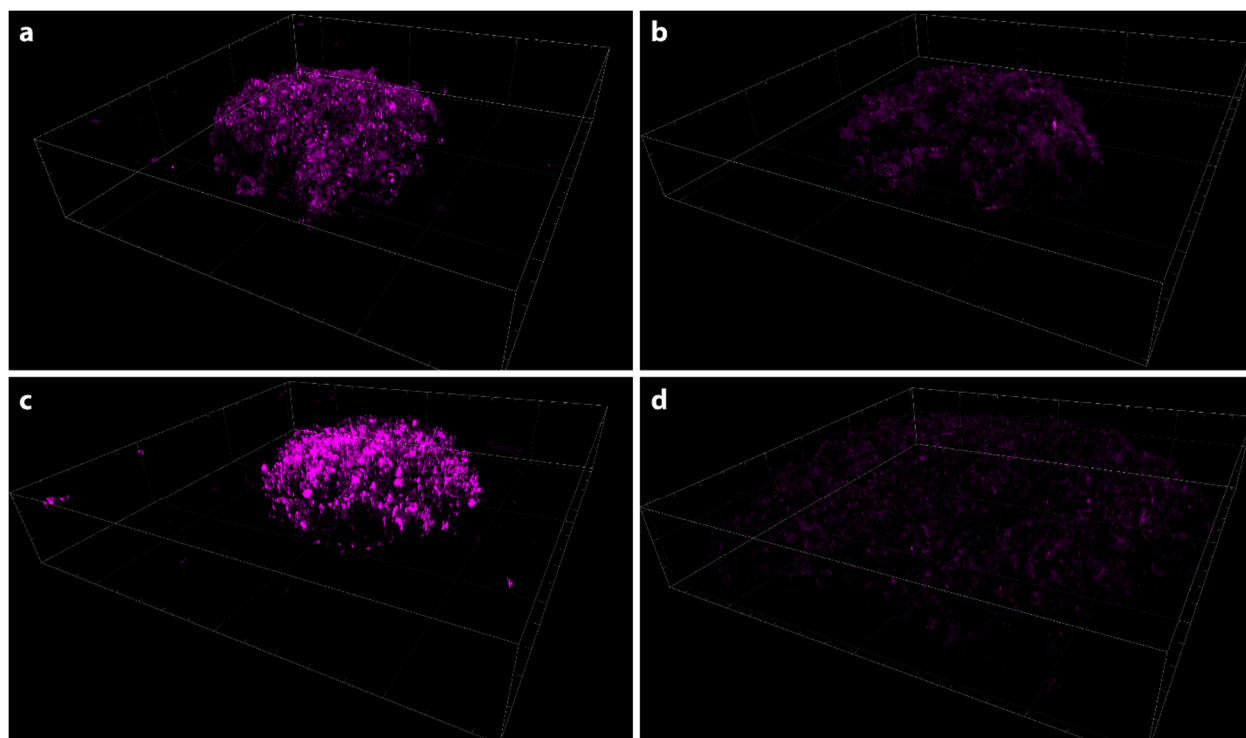
Figure S30. 3D reconstructions of spheroids of NR-preloaded HeLa cells treated with the substrate **5**. a) First generation of **6** after 24 h incubation of **5** (20 μM). b) 24 h cleansing. c) Second generation of **6** after 24 h incubation of **5** (20 μM). d) Control experiment of "empty" (Pd "free") spheroids incubated during 24 h with substrate **5** (20 μM). All these experiments were carried out using exactly the same experimental conditions and acquisition settings.

Supplemental References

1. Wang, J., Zheng, S., Liu, Y., Zhang, Z., Lin, Z., Li, J., Zhang, G., Wang, X., Li, J., Chen, P. R. (2016). Palladium-Triggered Chemical Rescue of Intracellular Proteins via Genetically Encoded Allene-Caged Tyrosine. J. Am. Chem. Soc. 138, 15118-15121.
2. Chen, T., Wei, T., Zhang, Z., Chen, Y., Qiang, J., Wang, F., Chen, X. (2017). Highly sensitive and selective ESIPT-based fluorescent probes for detection of Pd2+ with large Stocks shifts. Dyes Pigm. 140, 392-398.
3. Clavadetscher, J., Indrigo, E., Chankeshwara, S. V., Lilienkampf, A., Bradley, M. (2017). In-Cell Dual Drug Synthesis by Cancer-Targeting Palladium Catalysts. Angew. Chem. Int. Ed. 56, 6864-6868.
4. Li, J., Yu, J., Zhao, J., Wang, J., Zheng, S., Lin, S., Chen, L., Yang, M., Jia, S., Zhang, X. et al. (2014). Palladium-triggered deprotection chemistry for protein activation in living cells. Nat. Chem. 6, 352.
5. Martínez-Calvo, M., Couceiro, J. R., Destito, P., Rodríguez, J., Mosquera, J., Mascareñas, J. L. (2018). Intracellular Deprotection Reactions Mediated by Palladium Complexes Equipped with Designed Phosphine Ligands. ACS Catal. 8, 6055-6061.
6. Miller, M. A., Askevold, B., Mikula, H., Kohler, R. H., Pirovich, D., Weissleder, R. (2017). Nano-palladium is a cellular catalyst for in vivo chemistry. Nat. Commun. 8, 15906.
7. Hühn, J., Carrillo-Carrion, C., Soliman, M. G., Pfeiffer, C., Valdeperez, D., Masood, A., Chakraborty, I., Zhu, L., Gallego, M., Yue, Z. et al. (2017). Selected Standard Protocols for the Synthesis, Phase Transfer, and Characterization of Inorganic Colloidal Nanoparticles. Chem. Mater. 29, 399-461.
8. Xie, X., Gao, G., Pan, Z., Wang, T., Meng, X., Cai, L. (2015). Large-Scale Synthesis of Palladium Concave Nanocubes with High-Index Facets for Sustainable Enhanced Catalytic Performance. Sci. Rep. 5, 8515.
9. Carrillo-Carrion, C., Martinez, R., Navarro Poupard, M. F., Pelaz, B., Polo, E., Arenas-Vivo, A., Olgiati, A., Taboada, P., Soliman, M. G., Catalan, U. et al. (2019). Aqueous Stable Gold Nanostar/ZIF-8 Nanocomposites for Light-Triggered Release of Active Cargo Inside Living Cells. Angew. Chem. Int. Ed. Engl. 58, 7078-7082.
10. del Pino, P., Yang, F., Pelaz, B., Zhang, Q., Kantner, K., Hartmann, R., Martinez de Baroja, N., Gallego, M., Möller, M., Manshian, B. B. et al. (2016). Basic Physicochemical Properties of Polyethylene Glycol Coated Gold Nanoparticles that Determine Their Interaction with Cells. Angew. Chem. Int. Ed. 55, 5483-5487.
11. Weiswald, L.-B., Bellet, D., Dangles-Marie, V. (2015). Spherical Cancer Models in Tumor Biology. Neoplasia 17, 1-15.